

Christiaan Boersma



Kapteyn Institute *Rijksuniversiteit* Groningen
Landleven 12
9700 AV Groningen

Project supervisors: Prof. Dr. A.G.G.M. Tielens (SRON / RUG) and dr. S. Hony (ESTEC)

Abstract. Large Polycyclic Aromatic Hydrocarbon molecules (PAHS) are thought to be formed as the byproduct of the soot formation process in the outflows of carbon-rich Asymptotic Giant Branch (AGB) stars. Carbon-rich AGB stars feed the universe with these complex species. However, the observational evidence for these molecules in the outflows of AGB stars is scarce. Generally, these types of species are detected in interstellar and circumstellar environments through their IR fluorescence spectra, pumped by FUV photon absorption. However, AGB stars are exceedingly cool, and so without appreciable FUV photons. An exception is the carbon-rich AGB star TU Tau, where a companion star provides the FUV photons necessary to excite PAH molecules.

Fifty ISO SWS¹ spectra of warm carbon-rich AGB stars have been investigated for residual UIR band emission to constrain the PAH evolution scheme. A binary star, TU Tau, shows interesting spectral structure in the appropriate wavelength regions. The IR spectra of AGB stars show a multitude of molecular absorption bands and dust emission features. Hence, the choice of the continuum is crucial to the identification and characterization of 'excess' spectral structure. Stars similar to TU Tau have been selected for comparing UIR bands. Their continua and optical depths have been matched with TU Tau. Blackbody fits to the spectra showed that local continua should be used and that optical depth corrections are necessary. The residual UIR band emission was obtained by subtracting the corrected spectra from TU Tau.

The derived UIR band profiles have been compared to UIR band profiles from the ISM, PNE and carbon-rich post AGB stars. The profiles of TU Tau are shown to have the most resemblance with those from PNE. Uncertainties in the deduced residual UIR band profiles exist, however comparisons to several stars give similar results, which strengthens the confidence put in the derived profiles. Integrated band flux ratios have also been determined and compared to object type flux ratio correlations found in other studies. Here no definite match was found.

The influence of the nearby companion star on the PAH ionization state and PAH formation rate has also been established. The analysis indicates that the contribution of the companion star to these parameters can be significant, depending on position in the outflow. Future modeling on the stellar outflow, including FUV photon processing, should reveal if the UIR band profiles from TU Tau are characteristic for 'common' carbon-rich AGB stars.

The match of the band profiles from TU Tau with those from PNE indicates that PAHS are formed in the CSE of carbon-rich AGB stars and make it largely unmodified into the PN phase. The variations in the band strength ratios between the different objects has been linked to the ionization state of PAHS and reflects the different physical environments within these objects. This is an indication that the differences between PNE and ISM PAHS is largely due to modifications during the ISM phase.

¹Based on observations with ISO, an ESA project with instruments funded by ESA member states (especially the PI countries: France Germany, the Netherlands and the United Kingdom) and with the participation of ISAS and NASA.

Contents

Introduction	1
1 Carbon-rich stars and their spectra	3
1.1 Carbon-rich stars	3
1.1.1 The circumstellar envelope	3
1.2 ISO	5
1.2.1 SWS	6
1.3 Features in IR spectra of carbon-rich stars	7
1.4 UIR - bands and PAHS	9
1.4.1 PAH structure	10
1.4.2 PAH emission mechanism	12
1.4.3 The IR characteristics of PAHS	13
1.4.4 PAH formation and evolution	14
1.5 The sample	15
1.5.1 Data reduction	15
1.6 TU Tau	17
2 UIR features in carbon-rich AGB stars	21
2.1 Spectral classifications	22
2.2 A first selection	25
2.3 Blackbody fits	31
2.4 The second and final selection	31
2.4.1 4.0 - 7.0 μm	33
2.4.2 7.0 - 10.0 μm	35
2.4.3 10.0 - 13.0 μm	39
2.4.4 3.0 - 4.0 μm	41
2.5 The residual UIR bands of TU Tau	41
2.5.1 Single star	42
2.5.2 Continuum and optical depth corrections	45
2.6 The profiles	49
3 Comparing the UIR bands	53
3.1 Profiles	53
3.1.1 C-C modes	53
3.1.2 C-H modes	53
3.2 Flux ratios and ionization	55
3.3 Implications	57
4 Impacts	61
4.1 PAH evolution	61
4.2 Influence of companion star on the PAH composition in TU Tau	63
5 Summary and conclusions	67
5.1 Discussion and future work	68

Acknowledgments	69
References	71
List of Figures	75
List of Tables	77
A ISO - SWS spectra	79
B Equivalent Widths	93
C Classification Color Maps	99
D <i>Method 1</i> refined	105

Introduction

The gas and dust present in space have a profound influence on the Interstellar Medium (ISM). They form a critical part in the evolution of galaxies and stars, the formation of planetary systems and the synthesis of organic molecules. During the late stages of their life time stars eject much of their mass, in the form of gas and dust, back into the ISM through winds and supernova explosions. In the ISM the dust is vulnerable to shocks, UV photons and ions which may alter its composition. The ISM is slowly enriched with this dust and heavy elements, which form the building blocks for future generations of stars and planets. Understanding this life cycle of gas and dust is one of the key goals in astrophysics.

An important component of interstellar dust, genuine star dust, can be traced back to Asymptotic Giant Branch (AGB) stars through meteorites (Messenger 1997). The dust in AGB stars is the driver of their mass loss and also determines the end of the AGB phase. Thus, knowledge on the properties of dust is essential for a correct understanding of stellar evolution.

Another component of interstellar dust are Polycyclic Aromatic Hydrocarbons (PAHs), large molecules made up from many aromatic rings. PAHs are excited upon the absorption of a single FUV photon (Sellgren 1984). The absorbed energy is redistributed over the molecule into C-C and C-H vibrational modes. These modes re-stabilize by emitting photons at characteristic IR wavelengths, leaving fingerprints by which they can be identified in spectra.

The presence of these large molecules in space has a big influence on many aspects of the ISM (Omont 1986). These aspects include interstellar (surface) chemistry due to their large surface area, heating and cooling of the ambient ISM through photo-electric ejection, infrared emission and gas-grain collisions and the charge balance, which on its turn influences the equilibrium state for chemical reactions. The presence of PAHs in space is generally accepted. However, up to now the specific molecular identification of the carriers remains elusive. In order to identify the individual molecules of the interstellar PAH family an understanding of the evolution of PAHs is essential.

It is suggested that soot, carbonaceous dust, is formed via the carbon condensation route in the Circumstellar Envelopes (CSEs) of carbon-rich giants. PAHs are the primary building blocks in this route (see Allamandola et al. 1989, Frenklach & Feigelson 1989 and Cherchneff et al. 2000 for extensive overviews) and are also injected into the ISM by the stellar winds, when not incorporated into soot. At present the evidence for PAHs in the ejecta of carbon-rich giants is only indirect. This is for two reasons. First, spectra from carbon-rich protoplanetary nebulae and Planetary Nebulae (PNe) show strong IR emission features. These objects are the descendants of carbon-rich AGB stars and their circumstellar material originates from mass loss during the AGB phase (Salpeter 1971, Osterbrock 1974). Second, analysis of some graphite stardust grains isolated from meteorites - whose isotopic composition betrays an origin in carbon-rich AGB stars - have revealed the presence of (specific) small PAHs with an isotopic composition similar to that of the parent, genuine, grain (Messenger 1997). Likely, these PAHs are stowaways who survived the rigors of the ISM deeply embedded within these grains.

This thesis deals with the search for PAHs in the outflows of carbon-rich AGB stars. Emission features around 3.3, 6.2, 7.6, 7.9, 8.6, 11.2 and 12.7 μm , called the Unidentified IR (UIR) bands (Gillett et al. 1973, Geballe et al. 1985 and Cohen et al. 1986), are commonly ascribed to PAHs

(Leger & Puget 1984, Cohen et al. 1985, Puget & Leger 1989 and Allamandola et al. 1989). In astronomical spectra these features always seem to appear together, accompanied by broad emission plateaus. Laboratory spectra of PAHS reproduce the main characteristics of the UIR bands closely.

The UIR emission features are observed everywhere in space where matter is irradiated by FUV photons. The detection of PAHS in most AGB stars may well be hampered by the lack of FUV photons in their environment. An exception is a particular star system named TU Tau, a binary system. This system harbors an AGB stars with a carbon-rich outflow and a blue companion star that produces some FUV photons. These FUV photons may enable PAHS to be detected.

Prior research in this area, done by Speck & Barlow (1997) and Buss et al. (1991) using respectively IRAS and UKIRT spectra, showed minor evidence for the existence of residual UIR band emission in TU Tau. Here is hoped to improve on their work by using spectra obtained by the Short Wavelength Spectrometer (SWS) on board ESA's Infrared Space Observatory¹ (ISO) (de Graauw et al. 1996). These spectra have better signal to noise, higher spectral resolution and a wider wavelength coverage, which allows to search for all the IR emission features in TU Tau. Also, the C-H bands in the previously studied 8 - 13 μm region, are known to vary in strength and therefore may have presented only limited tracers of the presence of circumstellar PAHS.

The aim of this study is to establish the similarities and differences of the UIR bands from TU Tau compared to the UIR bands found in the ISM, carbon-rich post-AGB stars and PNE. It is known that the bands in the 5 - 9 μm range exhibit strong spectral variations reflecting their environment. Hence, the study of this region provides a tool for studying the evolution of PAHS.

The outline of this thesis is as follows: The first chapter treats carbon-rich stars and their spectra, including sections on the UIR bands and their carriers, the sample and Tu Tau. The second chapter deals with the determination of the UIR band profiles of Tu Tau. Chapter three deals with the comparison of these profiles with the UIR band profiles found in the ISM, carbon-rich post-AGB stars and PNE from Peeters et al. (2002) and Peeters et al. (2003). The integrated flux ratios in the UIR band are also determined. They are compared with object type flux ratio correlations found by Hony et al. (2000). The fourth chapter treats the astronomical impacts and the possible influences of the nearby companion star on the PAH in the CSE of TU Tau. In the last chapter a summary is presented and the conclusions are drawn, also a discussion is included and a section on future work.

¹Based on observations with ISO, an ESA project with instruments funded by ESA member states (especially the PI countries: France Germany, the Netherlands and the United Kingdom) and with the participation of ISAS and NASA.

Chapter 1

Carbon-rich stars and their spectra

1.1 Carbon-rich stars

Low through intermediate-massed stars ($M = 1 - 8M_{\odot}$), spend most of their life on the Main Sequence (MS), fusing hydrogen into helium in their core. After depletion of the hydrogen in the now mostly helium core, the star becomes a Red Giant and starts fusing hydrogen in a shell surrounding the core. Only the intermediate-massed stars reach the Horizontal Branch (HB). On the HB in the core of the star helium starts fusing into carbon (by the triple- α process) and oxygen. When the helium from the core has been depleted the star will ascend the Asymptotic Giant Branch (AGB). AGB stars are very cool ($T_{\text{effective}} \leq 3000 \text{ K}$), but bright ($L = 10^3 - 10^4 L_{\odot}$), implying a large stellar radius ($R = 200 - 400 R_{\odot}$). The core has a small radius ($\sim 3000 \text{ km}$), essentially a White Dwarf, and consist mainly of carbon and oxygen. The core is surrounded by a helium shell. The mass of the helium shell is increased by the helium coming from the fusion of hydrogen in a layer surrounding the helium. When the mass of the shell reaches a critical value the helium ignites fusion.

It is in this helium shell burning phase when heavy elements, mostly carbon, oxygen and nitrogen from the stellar interior are dredged up by convection into the extended hydrogen envelope surrounding the helium shell. This is called a Thermal Pulse (TP) and causes the long term variability of these stars, known to have a period of $\sim 10^4$ year, not to be confused with the short term pulsations of these objects having a period ~ 1 year.

In the atmosphere of the star the carbon reacts easily with the oxygen and forms the very stable molecule carbon-mono-oxide (CO). This effectively locks up the carbon or oxygen. Depending on the C/O ratio the star is classified oxygen-rich (class M: $C/O \leq 0.6$, class S: $C/O \approx 0.9$) or carbon-rich (class C: $C/O > 1.05$).

1.1.1 The circumstellar envelope

The density and temperature structure in the stellar atmosphere is highly dependent on dynamical phenomena, such as shock waves and stellar winds. Stellar pulsations create strong shock waves in the atmosphere causing levitation of the outer layers, hence cooling the outer layer of the atmosphere. When the atmosphere has been pushed far enough outward for the temperature to fall below 1500 K , solid particles, dust can form. It is on these particles radiation pressure from the star has a grip. The radiation pressure exerted on the particles is enough to accelerate them against the gravitational pull of the star. Through collisions the gas is coupled to the dust and the star has a strong mass-loss with a relatively low outflow velocity of less than $15 \text{ km}\cdot\text{s}^{-1}$.

When the outer envelope becomes gravitationally unbound its called the Circumstellar Envelope (CSE). The high mass-loss rate, up to $\sim 10^{-4} - 10^{-3} M_{\odot} \cdot \text{yr}^{-1}$ feeds the CSE, making the central star totally obscure in the optical. The absorbed light by the dust is re-emitted in the near-IR and IR.

When the central star has lost most of its envelope it enters the post-AGB phase. Typically the remainder of the star stays only $10^3 - 10^4$ year in the post-AGB phase. As a consequence, these

types of objects are very rare. Post-AGB stars can be recognized from two distinct contributions that appear in their spectral energy distribution (SED). First, the contribution from the expanding CSE that leaves its marks in the IR. Second, the contribution from the remaining central star that leaves marks at UV and optical wavelengths, as the optical depth decreases due to the expansion of the envelop UV and optical photons are able to penetrate the dust shell. The central star continues to fuse hydrogen in a very small hydrogen envelope ($\sim 10^{-3} M_{\odot}$) close to the surface of the star. When the central star reaches a temperature $T_{\text{effective}} \gtrsim 3 \cdot 10^4$ K it is capable of ionizing the CSE. This defines a new evolutionary stage: the Planetary Nebula (PN). The future of the central star is governed by the remaining mass of the hydrogen-rich envelope. When the mass of the envelope becomes too low fusion will stop and the star will slowly cool down and become a White Dwarf. Fig. 1.1 presents a sketch of the evolution of a low-mass star in the Hertzsprung-Russel diagram.

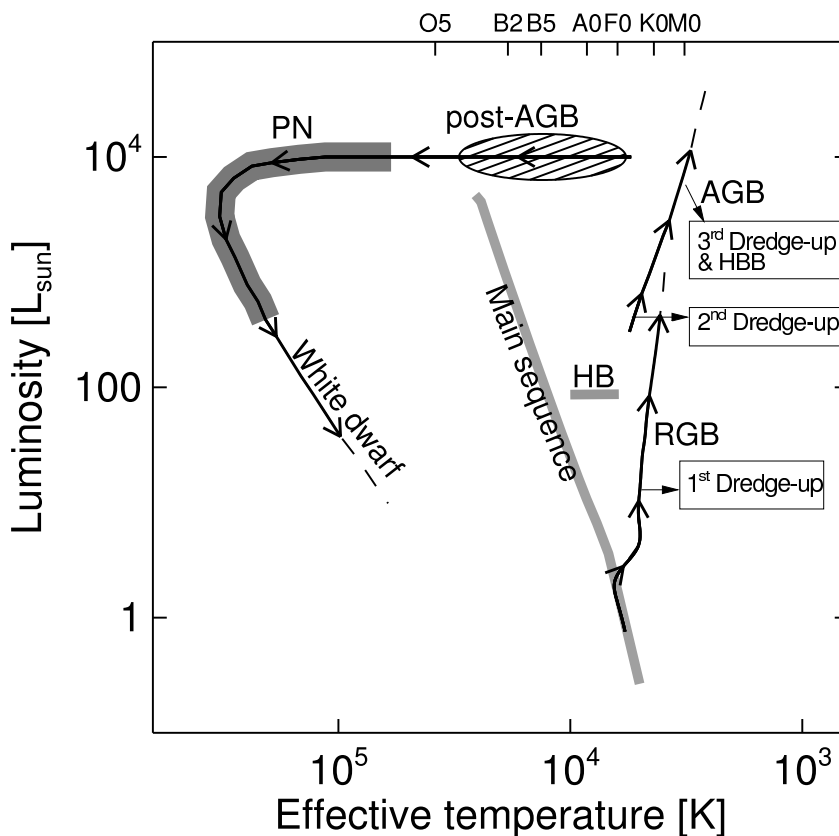


Figure 1.1— A sketch of the evolution of a low-mass star in the Hertzsprung-Russel diagram. Indicated are the evolutionary stages. Adapted from J. Bernard-Salas.

In the cool and expanding CSE further reactions including the C and O take place, which might give rise to the formation of more complex species than CO. In the CSE of carbon-rich stars, carbon-based molecules will form, which perhaps will be destroyed again in a later stage when the central star starts ionizing its surroundings. The formed molecules are the building blocks for the dust that is present during the PN phase and that eventually may appear in the ISM.

Carbon-based molecules show in general a wide range of rotational and vibrational transitions. These transitions lie mainly in the infrared. IR observations are therefore the tool to probe the rich collection of species in these stellar envelopes, which are the key to understanding dust evolution.

1.2 ISO

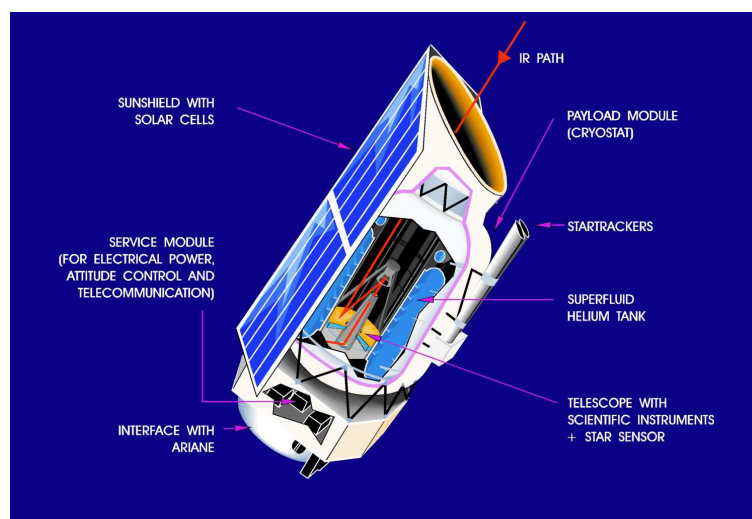


Figure 1.2— Schematic overview of the layout of ESA's Infrared Space Observatory (ISO). Source Leech et al. (2003)

The infrared universe has been clouded for a long time. Due to the high temperature of our own atmosphere and telluric lines ground based IR observations are only possible through a few, so called spectral windows. At these windows the earth's atmosphere is relatively transparent. In 1983 the launch of the IRAS satellite opened up more windows and on the 17th of November 1995 the total infrared spectrum (from 2 to 200 μm) became accessible with the launch of ESA's Infrared Space Observatory (ISO). The ISO satellite had a 28 month mission. By the 8th of April 1998 it had made more than 30,000 observations. A schematic overview of the satellite is given in Fig. 1.2.

The instrument package carried by ISO were the Long-Wave Spectrometer (LWS), ISOPHOT, a photo-polarimeter, ISOCAM, an infrared camera and the Short Wavelength Spectrometer (SWS), which gathered the data used in this work.

1.2.1 sws

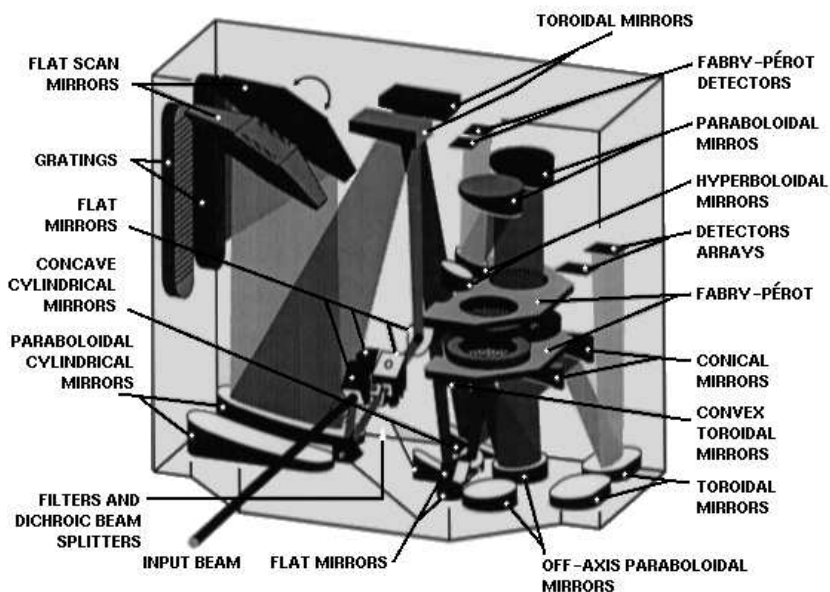


Figure 1.3— Schematic overview of the sws instrument carried by iso. Source de Graauw et al. (1996).

The sws instrument made 3763 scientific observations, which accounts for 13% of the total observations made by iso. In time, 2694 hours were used, accounting for 25% of the total amount of observation time. The size of the instrument was about that of a typical overhead projector. Together with the three other instruments the sws instrument was mounted into a cryostat, which was cooled with liquid helium to almost absolute zero. An overview of the instrument is given in Fig. 1.3. The instrument provided medium and high spectral resolution in the wavelength region from 2.38 up to 45.2 μm . The two spectrometers of the instrument had a spectral resolution R ($\equiv \frac{\lambda}{\Delta\lambda}$) of $\sim 1000 - 2000$, which corresponds to $\Delta v \sim 300 - 150 \text{ km}\cdot\text{s}^{-1}$. Two Fabry-Pérot (FP) filters could be inserted, increasing the resolution up to $R \sim 30,000$; $\Delta v \sim 10 \text{ km}\cdot\text{s}^{-1}$ for 25 - 35 μm , outside this range slightly less.

Light from the telescope reached the sws instrument through reflection by iso's pyramidal mirror. Each of the three entrance apertures of the sws instrument had its own dichroic beam splitter feeding the Short Wavelength (sw) and Long Wavelength (lw) section of the detector. The apertures were controlled by a shutter system, opening one of the apertures and closing the other two. Since the sw and lw section are independent, both wavelength ranges could be observed simultaneously. The sw section covered 2.38 - 12 μm and used a 100 lines/mm grating in the first four orders. The lw section covered 12 - 45.2 μm and used a 30 lines/mm grating in the first two orders.

The detectors were arranged into four arrays of twelve elements each for the sw and lw section and two double detectors for the Fabry-Pérots ($= 4 \times 12 + 2 \times 2 = 52$ detectors). The detection of a certain wavelength region was achieved by combining specific detectors, apertures and grating orders. Each combination was called a band. The bands had been chosen such that for each band

its array of detectors received the light of a unique order from the gratings. The sws band specifications are given in Table 1.1.

The light from each grating was redirected to the detectors by a mirror positioned close to the grating. Selecting a specific wavelength to fall on the detectors was achieved by rotating the mirror in discrete scan steps. Observations were made using an up-down scanning mechanism, meaning the grating initially made a scan of a wavelength range in one direction, then in the reverse direction. The availability of these two independent scans allows, to some extent to discriminate between 'real' spectral features and instrumental 'artifacts'.

The iso - sws instrument made several observations of carbon-rich AGB stars, making the wide variety of features accessible for investigation. The iso - sws spectra showed features from known and unknown species.

<u>Section</u>	<u>Band</u>	<u>Order</u>	<u>Area^a (″×″)</u>	<u>Detector Numbers</u>	<u>Wavelength^b (μm)</u>	<u>Resolution^c</u>
sw	1A	4	14-20	1 - 12	2.38 - 2.60	1870 - 2110
sw	1B	3	14-20	1 - 12	2.60 - 3.02	1470 - 1750
sw	1D	3	14-20	1 - 12	3.02 - 3.52	1750 - 2150
sw	1E	2	14-20	1 - 12	3.52 - 4.08	1290 - 1540
sw	2A	2	14-20	13 - 24	4.08 - 5.30	1540 - 2130
sw	2B	1	14-20	13 - 24	5.30 - 7.00	930 - 1250
sw	2C	1	14-20	13 - 24	7.00 - 12.0	1250 - 2450
lw	3A	2	14-27	25 - 36	12.0 - 16.5	1250 - 1760
lw	3C	2	14-27	25 - 36	16.5 - 19.5	1760 - 2380
lw	3D	1	14-27	25 - 36	19.5 - 27.5	980 - 1270
lw	3E	1	20-27	25 - 36	27.5 - 29.0	1300
lw	4	1	20-33	20 - 27	29.0 - 45.2	1020 - 1630

^a Aperture area' refers to the dimensions of the sws detectors projected through the entrance apertures projected onto the sky. The first number refers to the size in the dispersion direction and the second refers to the cross dispersion direction.

^bThese are the validated ranges of the bands. The actual wavelength ranges are slightly greater.

^cThe resolution given is that obtained when observing an extended source.

Table 1.1— sws band specifications. Source Leech et al. (2003).

1.3 Features in IR spectra of carbon-rich stars

In Fig. 1.4 the iso sws spectrum of RY Dra, a carbon-rich AGB star is shown. Indicated are the most common features together with the species from which they arise. The species contain the most common elements present in the cse, such as H, C, and N. Some species contain also some of the less abundant, heavier elements as Si, Ti and Zr. The species that can form are dependent on the local physical conditions in the envelope such as pressure, temperature and chemical abundances. Most of the molecular lines originate from close to the star, where the temperature is relatively high. Further away from the star, where it is cooler, the dust continuum forms together with the

dust features (e.g. SiC and MgS (Hony et al. 2003)). The spectra also exhibit this division: the strongest molecular resonances fall shortward of $\sim 15 \mu\text{m}$, while the dust continuum and the dust features are found at longer wavelengths. Reversing the logic, certain wavelength bands can be used to probe the different regions in the CSE, which can teach us something about the structure of the CSE. However, that is not the focus of this work.

The most common species found in carbon-rich AGB stars are C_2 , CN, CH, C_3 , HCN, C_2H_2 and SiC. In the 2.38 - 45.2 μm wavelength range these species have one, or several resonances, some partially overlapping. Table 1.2 gives an overview of the most important species and at what wavelength there signatures appear in the spectra.

The physical conditions in the CSE also allow for, besides the relatively simple species, rather large and complex molecules to form. The spectroscopic fingerprints of these molecules have been found in spectra from post-AGB stars, PNE and the ISM. The question is what evidence there is for the existence of these molecules in the CSEs of carbon-rich AGB stars. The spectroscopic fingerprints, the molecular structures, the emission mechanisms and the formation mechanism of those molecules are the subjects of the next section.

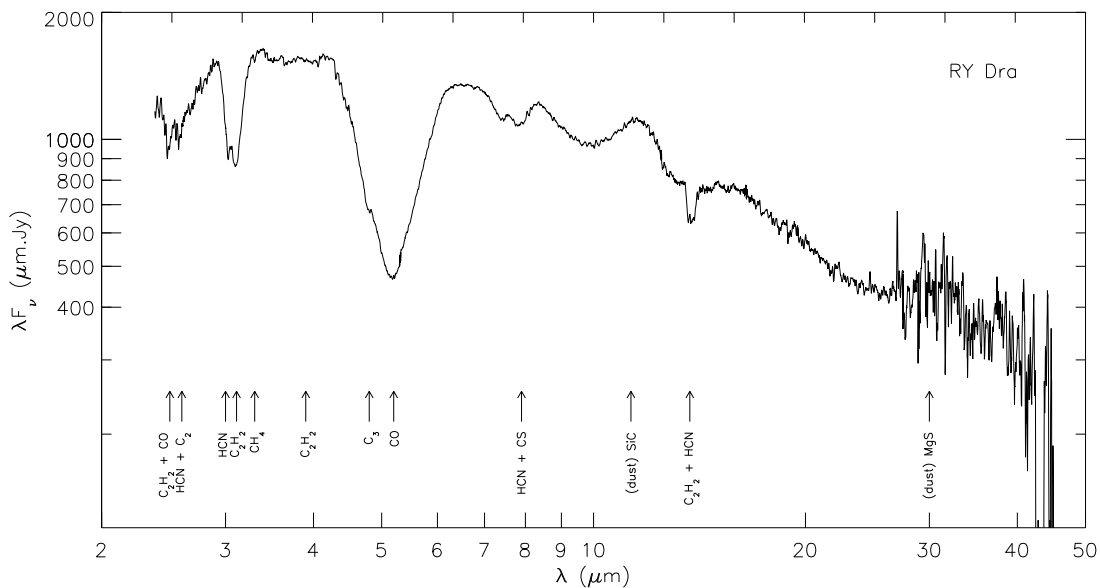


Figure 1.4— iso - sws spectra of RY Dra showing most of the typical features, including molecular and dust features, in carbon-rich AGB stars.

<u>Band</u>	<u>Species</u>
2.5 μm	$\text{C}_2\text{H}_2 + \text{CO}$
2.6 μm	$\text{HCN} + \text{C}_2$
3.0 μm	$\text{HCN} + \text{C}_2\text{H}_2$
3.3 μm	CH_4
3.9 μm	C_2H_2
5.0 μm	C_3
7.9 μm	$\text{HCN} + \text{CS}$
11.3 μm	SiC (dust)
13.7 μm	C_2H_2
30.0 μm	MgS (dust)

Table 1.2— Identified bands in carbon-rich AGB stars, including molecular and dust features.

1.4 UIR - bands and PAHS

In the early 1980, when mid-IR observations became for the first time widely available, investigations of HII regions, PNE, Young Stellar Objects (YSO), the diffuse ISM and galaxies revealed a diversity of spectral features. Most of them have been identified with molecular absorption and/or emission bands. However around 12 μm , the so called IR cirrus, there were also emission features, although temperatures expected in these regions are far too cool to emit at such short wavelengths. Furthermore these features, located around 3.3, 6.2, 7.6, 7.9, 8.6, 11.2 and 12.7 μm , always appeared together and accompanied by broad emission plateaus (see Fig. 1.5 for an example). These bands couldn't be identified with 'normal' molecular emission bands and therefore, at first, these bands were called the Unidentified Infrared Bands (UIR). After almost a decade it was realized that very small dust grains consisting of about 20 - 100 C-atoms, more typically large molecules, are the most likely candidates for the carriers of these bands. The observed UIR wavelengths coincide with the typical resonances found in aromatic hydrocarbon molecules. Moreover, connected aromatic molecules may easily attain the temperature required to emit at such short wavelengths upon the absorption of a single FUV photon (see Sect. 1.4.2). Therefore the carrier of the UIR bands is thought to be a family of connected aromatic species, so-called Polycyclic Aromatic Hydrocarbons (PAHS). These PAHS, dispersed throughout interstellar space are, to date the largest known molecules in space. A very extensive and complete overview on PAHS in interstellar space is given by Omont (1986).

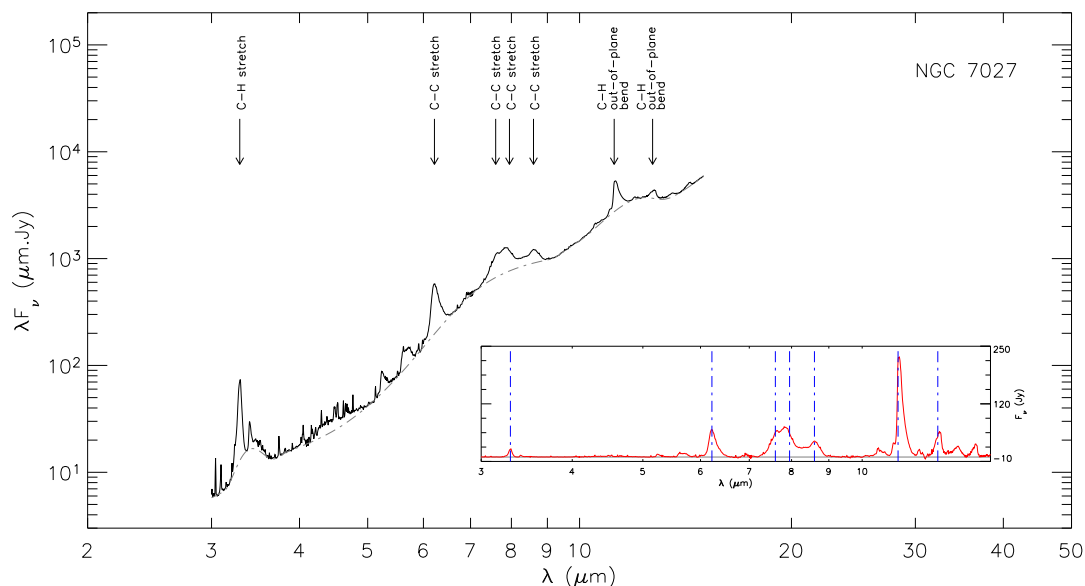


Figure 1.5— The IR emission features in the mid-IR spectra of the planetary nebula NGC 7027. Indicated are some of the ν_{IR} features together with their vibrational-mode identification.

1.4.1 PAH structure

Back on earth PAHs are known as a large family of tarry materials present in for example coal and crude oil. They are also formed during combustion of carbonaceous fuels and are therefore found in car exhaust, cigarette smoke, candle soot and burned food. In an astronomical context PAHs are a byproduct of dust formation.

Carbon atoms can have four bonds, this gives them the ability to form complex structures. A particular stable carbon complex is the benzene ring where the C-atoms are configured in a hexagonal ring with each atom bounded to three neighboring atoms by a σ , localized, bond. The fourth remaining electron of each C-atom forms a delocalized π bond with similar electrons of neighboring C-atoms, see Fig. 1.6.

The configuration is called aromatic and can be used as the basis of larger molecules consisting of several rings, such molecules are called polycyclic. When these molecules are only made up from hydrogen and carbon we speak of Polycyclic Aromatic Hydrocarbons (PAHs), e.g. Fig. 1.7. Non-aromatic hydrocarbons are called aliphatic. When a collection of PAHs are stacked parallel, like in graphite layers, one speaks of PAH platelets. PAH clusters are formed by PAHs stuck together in parallel and non-parallel orientations. PAH platelets and clusters form the basis of (hydrogenated) amorphous carbon.

In general it can be said for PAHs, that the more extensive the delocalized electron cloud, the more chemically stable the molecule. This is because for a PAH to react the σ -bond has to be broken and the aromatic π system has to be disrupted. Two typical classes of PAHs exist, the more centrally condensed, compact PAHs and the more open structured PAHs. The class of centrally condensed, compact PAHs are called pericondensed. The class of more open structured PAHs are called catacondensed, see Table 1.3 for some examples.

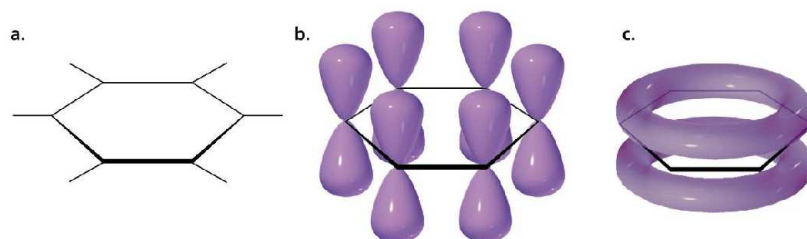


Figure 1.6— The structure of benzene. a: the σ -bonding framework of benzene. b: the p orbitals which form the delocalized π -bonding system in benzene. c: shape of the π electron clouds above and below the plane of the ring in benzene.

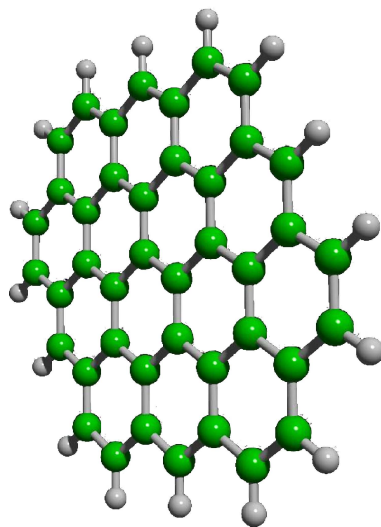


Figure 1.7— PAH example, circum-coronene ($C_{42}H_{16}$).

Pericondensed		Catacondensed	
Name	Structure formula	Name	Structure formula
Pyrene	$C_{16}H_{10}$	Naphthalene	$C_{10}H_8$
Perylene	$C_{20}H_{12}$	Tetraphene	$C_{18}H_{12}$
Antanthrene	$C_{22}H_{12}$	Pentaphenen	$C_{22}H_{14}$
Benzoperylene	$C_{22}H_{12}$	Phenanthrene	$C_{14}H_{10}$
Coronene	$C_{24}H_{12}$	Chrysene	$C_{18}H_{12}$
Ovalene	$C_{32}H_{14}$	Pentacene	$C_{22}H_{14}$

Table 1.3— The two main PAH classes with some examples.

Rings	$r - 1$
General structure formula	$C_{6r^2}H_{6r}$
Hexagonal cycles	$3r^2 - 3r + 1$
C-C bond length	$\approx 1.4 \text{ \AA}$
Area 1 aromatic cycle	$\approx 5 \text{ \AA}^2$
Total area (σ_{PAH})	$\approx 2.5 \times 10^{-16} \cdot N_C \text{ cm}^2$
Circular radius (a)	$0.9 \times 10^{-8} \cdot N_C^{\frac{1}{2}} \text{ cm}$

Table 1.4— Some properties for fully centrally condensed PAHS.

The structure is directly tied to the stability of the PAH molecule. The most stable PAHS are among the pericondensed, since this structure allows for complete electron de-localization throughout the entire molecule between all adjacent carbon atoms, In Table 1.4 some properties for fully centrally condensed PAHS are given.

The PAH's temperature is a very sensitive function of its heat capacity, which is determined by the size of the molecule. The PAH temperature translates itself into the observed band strength ratios: conversely, these ratios can be used to deduce the 'average' size of the emitting PAHS. The sharp UIR bands, in particular the $3.3 \mu\text{m}$ feature, is emitted by PAHS with between 50 to 100 carbon atoms. Generally the plateaus are formed by bigger, non-planer three dimensional PAHS, they are clearly discernible in Fig. 1.5. These PAHS are held together by weak Van der Waals bonds. At $25 \mu\text{m}$ some excess emission can also be ascribed to PAHS sized up to 10^5 C-atoms, which are more like small grains ($\approx 50 \text{ \AA}$).

1.4.2 PAH emission mechanism

In interstellar space PAH molecules are not in thermal equilibrium with the local radiation field. Instead, PAHS are electronically excited into an upper electronic state upon the absorption of a single FUV photon, raising the PAH's temperature as much as 1000 K. Rapidly the energy is internally

converted from the single excited vibrational state into several excited vibrational states, bringing the PAH back into a lower electronically state. The molecule cools down mainly by radiative cascade through IR emission in the C-C and C-H vibrational modes (see Table 1.5), decreasing its temperature to ~ 10 K on a timescale of seconds. The internal energy redistribution is a complex mechanism involving the coupling of different vibrational modes and can occur in several steps involving different timescales.

Laboratory studies show that PAH ionizations do not affect the frequency of vibrational resonances much. More striking is the effect on the relative intensity of the various modes. This effect is the clearest in the 5 - 10 μm region, where the resonances are very weak in neutral PAHS and much stronger in charged PAHS. PAHS can both be positively and negatively charged. The charge is set by the balance between photoelectrically ejected electrons and the PAH electron recombination rate, and is thus determined by the ratio of the UV field (G_0) and the electron density (n_e).

Bands (μm)	Mode(s)
3.3	aromatic C-H stretching
3.4	aliphatic C-H stretching in methyl groups C-H stretching in hydrogenated PAHS hot band of the aromatic C-H stretch
5.2	combination of C-H bend and C-C stretch
5.65	combination of C-H bend and C-C stretch
6.0	C-O stretch (?)
6.2	aromatic C-O stretching
6.9	aliphatic C-H bending
7.6	C-C stretching and C-H in-plane bending
7.8	C-C stretching and C-H in-plane bending
8.6	C-H in-plane bending
11.0	C-H out-of-plane bending, solo, cation
11.2	C-H out-of-plane bending, solo, natural
12.7	C-H out-of plane bending, trio, cation (?)
13.6	C-H out-of-plane bending, quartet
14.2	C-H out-of-plane bending, quartet
16.4	in-plane + out-of-plane C-C-C bending in pendant ring (?)
Plateaus (μm)	
3.2 - 3.6	C-C stretch overtone/combination
6 - 9	many C-C stretch blend and C-H in-plane bend ^a
11 - 14	blend out-of-plane C-H ^a
15 - 19	in-plane and out-of-plane C-C-C bending

^aIn clusters of PAHS.

Table 1.5— The IR emission features with wavelengths and mode identifications.

1.4.3 The IR characteristics of PAHS

The best known IR PAH emission features lie around 3.3, 6.2, 7.6, 7.9, 8.6, 11.2 and 12.7 μm . These coincide with the characteristic wavelengths for the stretching and bending vibrations of aromatic hydrocarbon materials. Table 1.5 summarizes the IR features with the specific modes

of PAH molecules. Besides the well know features there are a lot of more subtle and weaker ones. These weaker bands vary in relative importance from source to source and may even be completely absent in some, with otherwise clear UIR bands. The main UIR features also show strong variations in relative strength (Peeters et al. 2003). Moreover, detailed studies of the main UIR bands show that their profiles differ considerably between different regions in the sky (Hony et al. 2000). All these observed variations reflect the way in which the ensemble of PAH molecules reacts on the local physical conditions. Thus, the UIR bands originate in a family of related PAHS, but the exact composition of this ensemble traces the local conditions. The observed UIR variations are found to correlate to a large extent with the nature of the source. The UIR bands in massive star-forming regions all resemble each-other, as do the UIR spectra of galaxies. There is a larger spread in sources that are currently producing or processing dust; e.g. PNE and young stars with disks. Thus, the UIR bands can be used as a tracer of the molecular gas *and* the nature of the source where this gas is near.

The different modes reflect to a large extent the nearest neighbor interactions, which is why the resonances from a family of structurally related molecules (PAHS) tend to overlap. This explains also qualitatively why UIR spectra from widely different regions, with correspondingly different molecular families, are relatively similar. A similar clustering of resonances is observed in PAHS in the laboratory. The interstellar IR spectra often show narrower lines than those observed in laboratory spectra. This is due to fact that laboratory materials are more disordered. The precise position of a specific mode is dependent on the size, symmetry, structure, molecular heterogeneity of the PAH molecule and of the charge. Guided by laboratory experiments and quantum mechanical calculations the observed IR spectra can teach us about the interstellar PAH families.

1.4.4 PAH formation and evolution

PAHS represent the extension of the grain-size distribution into the molecular domain and are the building blocks of soot particles, dust. The main molecule from which PAHS are formed is acetylene (see Fig. 1.8) and its radical derivatives. The first step in PAH formation, which is the most difficult one, is the creation of the first aromatic ring. In additional reactions on the aromatic ring, such as abstraction of H-atoms and the addition of hydrocarbons, a PAH molecule is formed. For H-poor environments there is a three-way route. Upon the formation of small flexible linear C-chain radical monocyclic ring molecules are formed through the addition of C-atoms. The isomerization reactions on the C-chain lead to planar carbon hexagon structures. The absence of hydrogen leads to dangling bonds. Incorporation of pentagons and curling reduces the dangling bonds, possibly creating the specie fullerene, better known as 'The Bucky Ball' (Fig. 1.9).

Given the similarity between dust and PAHS, their evolution must be closely related. PAHS are mainly formed in the outflow of evolved stars and are introduced into the ISM by dust-driven winds. PAHS can be processed, destroyed or grow. PAH processing and destruction can be caused by high energetic radiation, high energetic particles or strong shocks. However, only the smaller PAHS are completely destroyed (up to 30 C-atoms). Near the stellar photosphere the high densities and temperatures allow for a PAH to grow chemically, further out in the flow PAH growth occurs by coagulation and accretion. Eventually a PAH might become part of a dust grain. Heavier elements produced by the star, as for example nitrogen, can be incorporated into PAHS as well.

In order to constrain the PAH evolution scheme by tying it to the dust evolution scheme, a sample of spectra of carbon-rich AGB stars observed by ISO has been investigated.

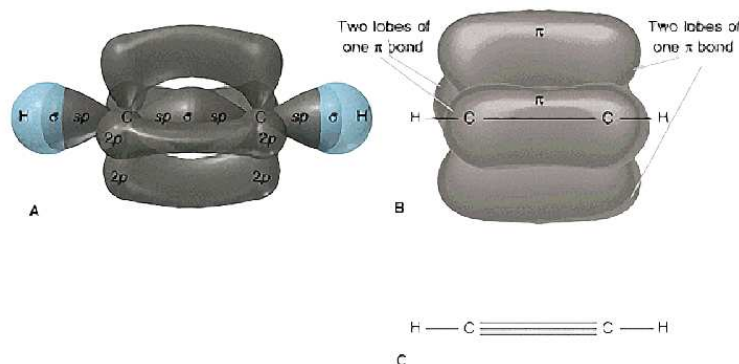


Figure 1.8— The structure of acetylene. A: σ bonds in acetylene and the electron orbitals. B: π bonds in acetylene. C: structural diagram for acetylene.

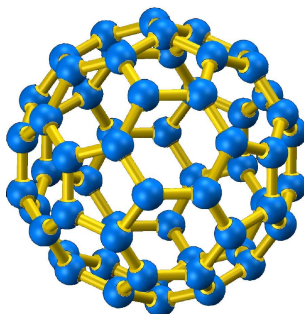


Figure 1.9— The structure of fullerene, better known as the “Bucky Ball”.

1.5 The sample

In this study the iso sws spectra of optically bright carbon-rich AGB stars have been used. The selected sources are those classified as either 1.NC or 2.CE and having a IRAS $12\ \mu\text{m}$ flux larger than 20 Jy. The classification scheme used is that from Kraemer et al. (2002), who classified the iso sws spectra on the spectral features and the slope of the continuum. The acquired sample consist of 50 spectra from 26 warm and bright carbon stars. The sample is presented in Table 1.8 at the end of this chapter. Also the optical classifications by Alksnis et al. (2001) have been added. The optical classifications do not span the full range of spectral classes, the stars are mainly N-type. The absence of the warm R-type stars indicates that stars rich in dust have been selected. The reduced iso sws spectra are shown in appendix A. The data reduction is discussed next.

1.5.1 Data reduction

Astronomical observations with the sws instrument were done using Astronomical Observing Templates (AOT). Available were four different science templates, each specialized for a different kind of observation. The four AOTs were sws01, for observing the entire $2.38 - 45.2\ \mu\text{m}$ range at low resolution, sws02, for observing specific spectral lines, sws06, for observing spectral ranges,

<u>speed</u>	<u>Duration (s)</u>	<u>Reset Interval (s)</u>	<u>Dwell Time (s)</u>	<u>Up-down Scans</u>
1	1172	1	1	1
2	1944	2	1	1
3	3846	2	1	1
4	6570	2	4	1

Table 1.6— sws01 speed specifications. Duration is the duration of the scan, Reset Interval is the time between detector resets, Dwell Time is the time in which the grating doesn't move and Up-down Scans is the number of up-down scans.

and sws07, for observing with the Fabry-Pérot filters. The 50 carbon star spectra in this work were observed using AOT sws01. sws01 had four user selectable scan speeds. Table 1.6 shows the sws01 speed specifications.

At the ground station the sws data beamed down by the satellite was collected and processed into several data files. These files contained the raw data, instrument status, pointing information, etc. The data file containing the detector read outs in time order is called the Edited Raw Data (ERD) file. In the next step a Standard Processed Data (SPD) file was created containing the uncalibrated signal and pertaining wavelengths, the data are still in time order. In the final step the file for scientific use is created, called the Auto Analysis Results (AAR) file. The last two steps were done by an automatic pipeline known as Off-Line Processing (OLP). The data in this work has been processed with (OLP) Version 10.1. Further reduction and analysis is possible using software packages like OSIA¹ and ISAP². In this work further reduction and analysis has been done using OSIA in combination with own software, written in C/C++.

Further data reduction consisted of extensive bad data removal. Glitches in the data were removed by inspecting the detector read outs in time and comparing the signal of each detector with the average signal from the other detectors in each sub-band in wavelength. Simultaneous jumps or glitches in all detectors of a sub-band have been isolated by comparing the independent up and down scan and removing the discrepant data. After cleaning the data have been re-binned to a regular wavelength grid with a resolution $R = 300$ (four times oversampled).

The re-binned spectra have been spliced with the sub-bands to form a continuous spectrum from 2.3 to 45.2 μm . At high flux levels the uncertainty in the absolute flux calibration is the dominant cause of discontinuities between neighboring sub-bands. While at low flux levels offsets due to dark-current corrections are thought to dominate. Scaling factors have been applied to those bands with a median flux level over 20 Jy and offset to bands with lower flux levels. In general the necessary corrections, in offset and scaling are small and in accordance with the quoted uncertainties for the sws instrument, except for three stars discussed below.

¹OSIA is a joint development of the sws consortium. Contributing institutes are SRON, MPE, KUL and the ESA Astrophysical Division.

²The Spectral Analysis Package (ISAP) is a joint development by the LWS and sws Instrument Teams and Data Centers. Contributing institutes are CESR, IAS, IPAC, MPE, RAL and SRON.

Y Cvn The observation is apparently affected by bad pointing and as a result the data in band 3 are systematically too low. A scaling factor of 1.8 is applied in order to match the flux levels with the data in band 2 and 4.

W Ori The data are of very high quality. However, the data in band 3A needs to be scaled by 1.25 to match sub-bands 2C and 3C. This correction falls outside the quoted flux calibration uncertainty of 12% for band 3A .

R Scl The data in band 4 is systematically too high and needs to be scaled by a factor 0.8 to match the data in band 3. This is probably due to the fact that the data in band 4 is obtained through a larger aperture and because this source is surrounded by a shell which is extended on the scale of the sws apertures (see Hony & Bouwman 2004).

In general the carbon stars in this study are relatively blue, this is the effect of choosing optically bright carbon stars. Notice that the combination of low flux levels at the longest sws wavelengths together with the increased noise levels of band 4 (29.0 - 45.5 μm) make this part of the spectrum to be often noise dominated and therefore unreliable.

As already has been discussed in section 1.4.2, PAH molecules need FUV photons to get electronically excited. Normally these are not present near carbon-rich AGB stars, however, one star in the sample, TU Tau, has a hot companion that may provide the necessary FUV photons.

1.6 TU Tau

TU Tau, a carbon-rich AGB star, classed C-N 4.5 C2, was shown to have a composite spectrum by Shane (1925), indicating a binary system. TU Tau's companion is a hot A star, classed A2 IV by Olson & Richer (1975). The angular separation between the two stars is 0.170 ± 0.025 arcsec (Perryman et al. 1997). The system is measured to have a radial velocity of $24 \text{ Km}\cdot\text{s}^{-1}$ (Wilson 1953). The mass-loss rate of TU Tau is estimated at $1.5 \cdot 10^{-7} \text{ M}_{\odot}\cdot\text{yr}^{-1}$ by Claussen et al. (1987), they put the star at the distance of 0.9 kpc, which is in good agreement with the parallax of 1.12 mas measured by Hipparcos (Perryman et al. 1997). Table 1.7 summarizes the properties of TU Tau with references to the data.

Iso observed TU Tau with the sws instrument on March the 17th 1998. The reduced spectrum is shown in Fig. 1.10, indicated are the locations of the molecular, dust and possible UIR features. A first glance at Fig. 1.10 near the locations of the UIR wavelengths shows sharpened peaks at some of these positions, which are not seen in the other spectra. This suggests, indeed, that emission unique to TU Tau may be present.

The next chapter deals with the determination of the residual UIR emission in the spectrum of TU Tau.

Name	TU Tau	<u>reference</u>
	Spectroscopic Binary	Shane (1925)
FK5 2000.0 RA	05 45 13.73	
FK5 2000.0 DEC	+24 25 12.5	
Star	HD 38218	
Parallax (mas)	1.12	Perryman et al. (1997)
Distance (pc)	893	<i>Inferred from parallax</i>
Proper motion (mas/yr)	3.46 -5.97	Perryman et al. (1997)
Radial velocity (Km · s ⁻¹)	-24	Wilson (1953)
mass-loss rate (M _⊙ ·yr ⁻¹)	1.5 · 10 ⁻⁷	Claussen et al. (1987)
Spectral type	C 5 II	Richer (1971)
V (mag)	8.46	Nicolet (1978)
B – V (mag)	2.87	Nicolet (1978)
U – B (mag)	1.36	Nicolet (1978)
K (2.2 μm) (mag)	1.76	Neugebauer & Leighton (1969)
I (mag)	5.84	Neugebauer & Leighton (1969)
F ₁₂ (Jy)	35.21	Beichman et al. (1988)
F ₂₅ (Jy)	9.17	Beichman et al. (1988)
F ₆₀ (Jy)	2.63	Beichman et al. (1988)
F ₁₀₀ (Jy)	2.24 (upper limit)	Beichman et al. (1988)
Interstellar extinction E(B – V) (mag)	0.44	Richer (1972)
Variability (days)	190	Perryman et al. (1997)
V _{min}	11.10	Kukarkin et al. (1971)
V _{max}	12.50	Kukarkin et al. (1971)
Spectral type companion	A2 IV	Olson & Richer (1975)
Angular separation (arcsec)	0.170 ± 0.025	Perryman et al. (1997)
Angular separation (AU)	>152 ± 22	<i>Inferred from separation (arcsec)</i>
Magnitude difference components (mag)	0.28 ± 0.35	Perryman et al. (1997)

Table 1.7— Properties of TU Tau, with references to the data.

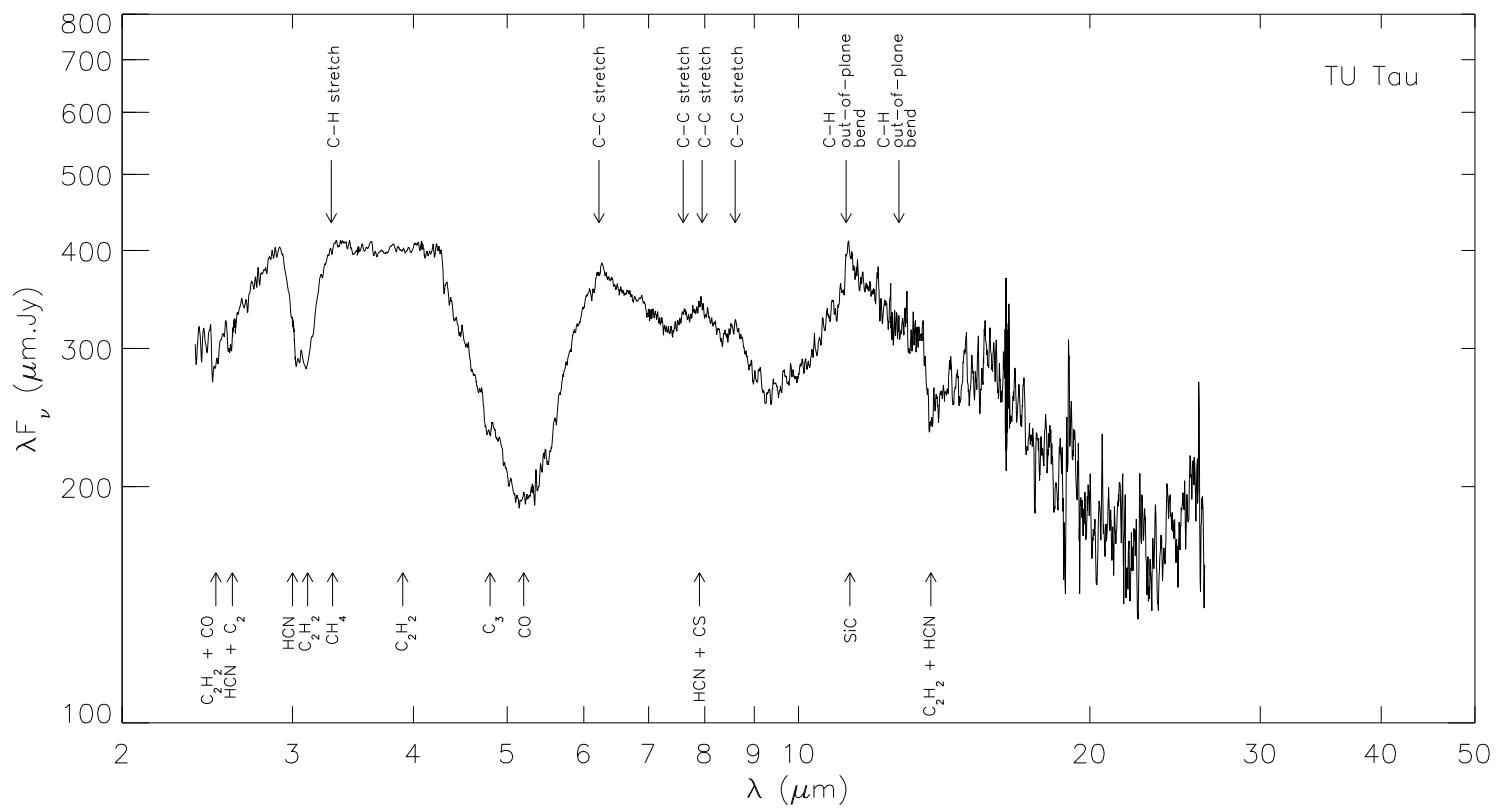


Figure 1.10— iso sws spectrum of TU Tau, indicated are the molecular line positions, dust features (below) and the UIR wavelengths (above). The data longward $25 \mu\text{m}$ have been omitted because of poor quality.

ID	SWS NAME	TDI	Mode(Speed)	RA (J2000)	DEC(J2000)	Obs.Date	Jul.Dat	Observer	IRAS	Preferred Name	Class (Kraemer)	Class (Alksnis)
0	HD19557	64601230	SWS01(1)	03h11m25.32s	+57d54m11.80s	1997-08-23	2450683.9	TTSUJI	03075+5742	HD19557	1.NC	n/a
1	TX PSC	55501379	SWS01(1)	23h46m23.50s	+03d29m12.59s	1997-05-24	2450593.0	SPRICE	23438+0312	TX Psc	1.NC	N0;C7.2
2	TX PSC	75700419	SWS01(2)	23h46m23.50s	+03d29m12.01s	1997-12-11	2450794.3	FKERSCHB	23438+0312	TX Psc	1.NC	N0;C7.2
3	V AQL	16402151	SWS01(2)	19h04m24.07s	-05d41m05.71s	1996-04-29	2450202.9	TDEJONG	19017-0545	V Aql	2.CE	N6
4	Y CVN	16000926	SWS01(2)	12h45m07.80s	+45d26m24.90s	1996-04-25	2450198.8	AHESKE	12427+4542	Y CVn	2.CE	N3
5	TU TAU	85403210	SWS01(2)	05h45m13.70s	+24d25m12.21s	1998-03-18	2450891.4	MBARLOW	05421+2424	TU Tau	2.CE	N2 + A
6	S SCT	16401849	SWS01(2)	18h50m19.93s	-07d54m26.39s	1996-04-29	2450202.8	TDEJONG	18476-0758	S Sct	2.CE	N3
7	V460 CYG	42201734	SWS01(1)	21h42m01.06s	+35d30m36.50s	1997-01-11	2450460.1	TTSUJI	21399+3516	V460 Cyg	2.CE	N1;C6.3
8	V460 CYG	74500512	SWS01(1)	21h42m01.10s	+35d30m35.99s	1997-11-29	2450782.3	FKERSCHB	21399+3516	V460 cyg	2.CE	N1;C6.3
9	T IND	71800602	SWS01(2)	21h20m09.50s	-45d01m18.98s	1997-11-02	2450755.3	AHESKE	21168-4514	T Ind	1.NC	N
10	T IND	37300427	SWS01(2)	21h20m09.50s	-45d01m18.98s	1996-11-23	2450411.0	AHESKE	21168-4514	T IND	1.NC	N
11	W ORI	85801604	SWS01(3)	05h05m23.70s	+01d10m39.22s	1998-03-22	2450895.4	ABLANCO	05028+0106	W ORI	2.CE	N5;C5.4
12	RY DRA	54300203	SWS01(3)	12h56m25.70s	+65d59m39.02s	1997-05-12	2450580.7	IYAMAMUR	12544+6615	RY Dra	2.CE	N4
13	SS 485	43600471	SWS01(1)	14h41m02.50s	-62d45m54.00s	1997-01-25	2450473.9	SPRICE	14371-6233	C* 2178	2.CE	R:
14	VX AND	42801502	SWS01(2)	00h19m54.10s	+44d42m34.99s	1997-01-17	2450466.3	TTANABE	00172+4425	VX And	2.CE	N7;C4.5
15	R FOR	82001817	SWS01(1)	02h29m15.30s	-26d05m56.18s	1998-02-13	2450857.6	KERIKSSO	02270-2619	R For	2.CE	Ne
16	RU VIR	24601053	SWS01(2)	12h47m18.43s	+04d08m41.89s	1996-07-20	2450284.6	TDEJONG	12447+0425	RU Vir	2.CE	R3e
17	CS 3070	42602373	SWS01(1)	21h44m28.80s	+73d38m03.01s	1997-01-15	2450464.2	SPRICE	21440+7324	C* 3070	2.CE	N
18	V CRB	11105149	SWS01(2)	15h49m31.42s	+39d34m18.01s	1996-03-07	2450150.2	JHRON	15477+3943	V Crb	2.CE	Ne
19	V CRB	42200213	SWS01(2)	15h49m31.39s	+39d34m18.01s	1997-01-11	2450459.9	JHRON	15477+3943	V Crb	2.CE	Ne
20	V CRB	42300201	SWS01(2)	15h49m31.39s	+39d34m18.01s	1997-01-12	2450460.9	JHRON	15477+3943	V Crb	2.CE	Ne
21	V CRB	47600302	SWS01(2)	15h49m31.39s	+39d34m18.01s	1997-03-06	2450513.8	JHRON	15477+3943	V Crb	2.CE	Ne
22	V CRB	57401003	SWS01(2)	15h49m31.39s	+39d34m18.01s	1997-06-12	2450611.9	JHRON	15477+3943	V Crb	2.CE	Ne
23	V CRB	67600104	SWS01(2)	15h49m31.40s	+39d34m18.01s	1997-09-21	2450713.3	JHRON	15477+3943	V Crb	2.CE	Ne
24	SS VIR	21100138	SWS01(1)	12h25m14.40s	+00d46m10.20s	1996-06-14	2450249.4	TTSUJI	12226+0102	SS Vir	2.CE	Ne
25	AFGL 933	86706617	SWS01(1)	06h25m01.60s	-09d07m16.00s	1998-03-31	2450904.5	SPRICE	06226-0905	V636 Mon	2.CE	c
26	CS 2429	46200776	SWS01(1)	17h20m46.20s	-40d23m18.09s	1997-02-20	2450500.1	SPRICE	17172-4020	C* 2429	2.CE	N
27	T DRA	11101727	SWS01(2)	17h56m23.29s	+58d13m06.39s	1996-03-07	2450149.8	JHRON	17556+5813	T Dra	2.CE	Ne
28	T DRA	24800101	SWS01(2)	17h56m23.30s	+58d13m06.39s	1996-07-21	2450286.3	JHRON	17556+5813	T Dra	2.CE	Ne
29	T DRA	34601702	SWS01(2)	17h56m23.30s	+58d13m06.39s	1996-10-28	2450384.5	JHRON	17556+5813	T Dra	2.CE	Ne
30	T DRA	42902712	SWS01(2)	17h56m23.30s	+58d13m06.39s	1997-01-18	2450467.5	JHRON	17556+5813	T Dra	2.CE	Ne
31	T DRA	43700103	SWS01(2)	17h56m23.30s	+58d13m06.39s	1997-01-26	2450474.8	JHRON	17556+5813	T Dra	2.CE	Ne
32	T DRA	54600104	SWS01(2)	17h56m23.30s	+58d13m06.39s	1997-05-15	2450583.6	JHRON	17556+5813	T Dra	2.CE	Ne
33	T DRA	64500205	SWS01(2)	17h56m23.30s	+58d13m06.39s	1997-08-21	2450682.4	JHRON	17556+5813	T Dra	2.CE	Ne
34	T DRA	38303014	SWS01(3)	17h56m23.30s	+58d13m05.59s	1996-12-04	2450421.5	ABLANCO	17556+5813	T Dra	2.CE	Ne
35	U CAM	64001445	SWS01(2)	03h41m48.16s	+62d38m55.21s	1997-08-17	2450677.9	TDEJONG	03374+6229	U Cam	2.CE	N5;C5.4
36	S CEP	56200926	SWS01(1)	21h35m12.80s	+78d37m28.19s	1997-05-31	2450599.8	KERIKSSO	21358+7823	S Cep	2.CE	N
37	S CEP	75100424	SWS01(1)	21h35m12.80s	+78d37m27.99s	1997-12-05	2450788.2	FKERSCHB	21358+7823	S Cep	2.CE	N
38	V CYG	08001855	SWS01(1)	20h41m18.28s	+48d08m28.90s	1996-02-05	2450119.3	TDEJONG	20396+4757	V Cyg	2.CE	Ne
39	V CYG	42100111	SWS01(2)	20h41m18.20s	+48d08m29.01s	1997-01-10	2450458.9	JHRON	20396+4757	V Cyg	2.CE	Ne
40	V CYG	42300307	SWS01(2)	20h41m18.20s	+48d08m29.01s	1997-01-12	2450460.9	JHRON	20396+4757	V Cyg	2.CE	Ne
41	V CYG	51401308	SWS01(2)	20h41m18.20s	+48d08m29.01s	1997-04-13	2450552.2	JHRON	20396+4757	V Cyg	2.CE	Ne
42	V CYG	59501909	SWS01(2)	20h41m18.20s	+48d08m29.01s	1997-07-03	2450633.0	JHRON	20396+4757	V Cyg	2.CE	Ne
43	V CYG	69500110	SWS01(2)	20h41m18.20s	+48d08m29.01s	1997-10-10	2450732.2	JHRON	20396+4757	V Cyg	2.CE	Ne
44	R SCL	24701012	SWS01(2)	01h26m58.10s	-32d32m34.91s	1996-07-21	2450285.7	JHRON	01246-3248	R Scl	2.CE	N;C6.5
45	R SCL	37801443	SWS01(2)	01h26m58.05s	-32d32m34.19s	1996-11-28	2450416.4	TDEJONG	01246-3248	R Scl	2.CE	N;C6.5
46	R SCL	37801213	SWS01(2)	01h26m58.10s	-32d32m34.91s	1996-11-28	2450416.4	JHRON	01246-3248	R Scl	2.CE	N;C6.5
47	R SCL	39901911	SWS01(2)	01h26m58.10s	-32d32m34.91s	1996-12-19	2450437.3	JHRON	01246-3248	R Scl	2.CE	N;C6.5
48	R SCL	41401514	SWS01(2)	01h26m58.10s	-32d32m34.91s	1997-01-03	2450452.3	JHRON	01246-3248	R Scl	2.CE	N;C6.5
49	R SCL	56900115	SWS01(2)	01h26m58.10s	-32d32m34.91s	1997-06-07	2450606.5	JHRON	01246-3248	R Scl	2.CE	N;C6.5

Table 1.8— The sample.

Chapter 2

UIR features in carbon-rich AGB stars

This chapter is concerned with the determination of the residual UIR band profiles of TU Tau from its iso sws spectrum (Fig. 1.10). The determination is based on the comparison of the spectrum of TU Tau with spectra from other, suitable, carbon-rich AGB stars.

Two things have to be taken into account when comparing two stars. First the complexity of the spectra. The figures in appendix A clearly show that many emission and absorption components are present in the spectra from carbon-rich AGB stars. Second, comparing one star to another is very sensitive to stellar characteristics, which are not very well known ($T_{\text{effective}}$, $\log g$, C/O, ...).

The spectra of carbon-rich AGB stars have various components. The principle component being the stellar continuum. Besides the continuum radiation carbon-rich AGB stars exhibit emission and absorption bands due to the molecules and dust in the CSE. Concentrating on the molecular absorption bands, the resultant spectrum can be approximated as:

$$F_{\nu(\star)}(\lambda) = F_{\nu(\text{C-star})}(\lambda)e^{-\tau_{\star}(\lambda)}, \quad (2.1)$$

with $F_{\nu(\text{C-star})}$ being the continuum and $\tau_{\star}(\lambda)$ the optical depth in the molecular bands, which is dependent on the physical conditions in the CSE and most importantly, on the abundances of the different species present. In addition, for TU Tau an extra component, due to the UIR bands, is suspected. Therefore, the spectrum of TU Tau is written as the sum of two parts, where the extra term is from the UIR bands ($F_{\nu(\text{UIR})}(\lambda)$).

$$F_{\nu(\text{TU Tau})}(\lambda) = F_{\nu(\text{UIR})}(\lambda) + F_{\nu(\text{C-star})}(\lambda)e^{-\tau_{\text{TU Tau}}(\lambda)} \quad (2.2)$$

Line formation is a complex interplay of the diffusion of energy outwards mediated by the absorption, scattering, and re-emission due to photospheric gasses. Clearly, the spectrum of TU Tau, or any other carbon-rich AGB star, is not that of a simple continuum with superimposed circumstellar absorption bands. Indeed, many of the molecular absorption bands that are seen mainly form in the photosphere.

However, it is beyond the scope of this project to develop a stellar atmosphere model for carbon-rich AGB stars to derive an appropriate model continuum. Rather this problem is approached phenomenologically by assuming an appropriate standard star with added circumstellar absorption and emission components.

For the determination of the residual UIR band profiles an expression for $F_{\nu(\text{C-star})}(\lambda)e^{-\tau_{\text{TU Tau}}(\lambda)}$ has to be found. This is achieved by rewriting eq. (2.2) into eq. (2.3), where $\mathcal{H}(F_{\nu(\star)}(\lambda))$, in the boxed part of the equation, is a function of $F_{\nu(\star)}(\lambda)$, which is the spectrum of an appropriate carbon-rich AGB star. Appropriate carbon-rich AGB stars do not show any residual UIR band emission and are selected from the sample of stars that has been discussed in section 1.5.

$$R_{\nu(\text{TU Tau})}(\lambda) = F_{\nu(\text{UIR})}(\lambda) = F_{\nu(\text{TU Tau})}(\lambda) - \boxed{\mathcal{H}(F_{\nu(\star)}(\lambda))} \quad (2.3)$$

First, the sample of carbon-rich AGB stars will be classified based upon several parameters. This is done to be able to determine the ‘appropriate’ stars for comparison. After selecting the appropriate stars the continuum component of the spectra is approximated as a blackbody, this will result for the need to use local continua near the UIR bands. Finally a summary and a discussion on the determined residual UIR band profiles will be given. Also the question “How real are the profiles that have been determined?” will be addressed.

2.1 Spectral classifications

The sample of stars consist of 26 optically bright carbon-stars classified 1.NC or 2.CE and having an IRAS 12 μm flux over 20 Jy. Several stars have been observed more than once. In total there are 50 spectra. To reduce the number of carbon stars under investigation and determine appropriate comparison stars, several characteristic features of the spectra have been quantified and compared from one spectrum to the other. First is the temperature of the blackbody fitted to the spectra considered. Due to the extent of the sample, the blackbodies have been auto-fitted to the spectra. The OSIA package contains a blackbody fitting routine that can be used to do this (see Section 1.5.1). The temperatures of the auto-fitted blackbodies are presented in Table 2.1. Note that the auto-fitting systematically underestimates the blackbody temperature for two main reasons:

1. The turn-over point of the blackbodies fitted to the warm carbon-rich AGB stars lie near the edge of the spectrum, between 2 - 4 μm . This region is dominated by the strong absorption features from C_2H_2 and CO. This results in a peak-shift for the auto-fitted Blackbodies to longer wavelengths, implying cooler temperatures.
2. Strong absorption features in the spectra, especially between 2 - 15 μm tend to lower the fitted blackbody flux in this region, causing a shift of the peak to longer wavelengths, implying, again, a cooler temperature.

Next the absorption bands together with the 11.3 μm SiC emission feature are considered. To do this, the Equivalent Widths have been measured. The EWs provide a good tool for comparing the strength of the absorption bands (and SiC emission feature) from one star to another. First for each band a straight local continuum has been drawn. Next the EW was determined, in accordance with eq. (2.4).

$$\text{EW} = - \int_a^b \frac{F_\nu(\lambda) - F_{\text{continuum}}(\lambda)}{F_{\text{continuum}}(\lambda)} d\lambda \quad (2.4)$$

Table 2.2 lists the features, the carriers and the adopted integration ranges, Table 2.1 presents the determined EWs.

Fig. 2.1 displays three spectra around 3.0 μm , showing the range in profile strength present in the sample. Take special notice of the CH_4 absorption feature, which is clearly visible here.

For the features that originate from the same species plots have been made showing the EW of the second specie (λ_y) plotted against that of the first specie (λ_x). Also the fractional EWs ($\frac{\lambda_x}{\lambda_y}$) have been determined and plotted, against the 13.7 μm EW ($\lambda_{13.7}$). Table 2.3 gives an overview of the common species and for which features the EW has been plotted. The plots are presented in appendix B. In each plot TU Tau has been colored purple.

The top figures in appendix B do not show a simple relation for most of the plotted EW, except perhaps for the 3.0 - 3.9 and 3.0 - 7.9 plots. The bottom figures show in some cases a small scatter

ID	Name	T _{BB} (K)	EW (Å)						
			2.5 + 2.6	3.0	3.9	5.0	7.9	11.3	13.7
0	HD19557	2679	292.194	12.0996	17.0181	3270.81	78.5659	-397.551	34.5692
1	TX PSC	2980	88.6688	1095.61	266.699	3951.22	3658.65	105.487	632.445
2	TX PSC	2880	178.828	1356.71	465.19	3873.62	4388.06	-357.344	506.277
3	V AQL	2449	337.526	1146.63	31.6168	7756.03	2191.61	-3695.15	1023.78
4	Y CVN	2674	562.939	1166.76	38.3889	7914.89	2305.12	-4535.56	1206.67
5	TU TAU	2222	321.262	599.484	70.1344	5991.89	407.509	-3888.9	966.211
6	S SCT	2350	350.815	1249.79	467.304	6726.77	3470.58	-2525.61	1119.95
7	V460 CYG	2808	177.607	472.321	138.56	4882.51	2254.14	-2907.09	982.77
8	V460 CYG	2839	200.168	713.19	138.261	5392.05	2430.5	-2947.33	836.678
9	T IND	2988	163.622	560.364	71.9523	3793.03	1719.14	-1376.71	668.305
10	T IND	2812	153.082	748.924	157.978	3895.63	2381.16	-2731.6	717.26
11	W ORI	2355	335.353	562.963	-42.7447	6737.35	796.159	-5863.2	933.817
12	RY DRA	2293	693.225	920.092	98.9295	7617.32	1373.76	-3187.51	760.278
13	SS 485	1070	249.216	1087.33	493.17	2192.55	2136.58	-3724.02	486.109
14	VX AND	2462	568.68	1363.03	-34.2912	8495.33	2544.24	-4264.93	1223.9
15	R FOR SCAN	1202	210.933	1106.98	299.247	1778.54	2037.83	-6359.38	531.747
16	RU VIR	997	252.722	1018.77	319.471	643.418	816.158	-6668.6	388.003
17	CS 3070	1522	407.956	1827.16	693.733	4376.86	2930.27	-6542.71	566.562
18	CRB V	1244	235.657	1571.69	475.94	1020.51	2714.41	-9592.25	555.34
19	CRB V	1363	178.926	1261.43	335.257	1558.69	1652.23	-9370.27	608.008
20	CRB V	1323	187.254	1369.5	455.884	853.893	2025.65	-11919.2	681.369
21	CRB V	1272	336.803	1609.34	717.61	1352.63	2533.79	-10715.3	1012.55
22	CRB V	1287	346.398	1579.73	706.016	1128.32	2638.81	-10653.2	689.431
23	CRB V	1481	-24.7111	816.686	55.4971	837.063	944.589	-9736.87	565.368
24	SS VIR	1785	514.816	2097.23	673.356	4988.44	4065.53	-7913.9	860.453
25	AFGL 933	1201	119.567	942.831	207.254	1575.75	1360.41	-6409.44	479.926
26	CS 2429	1815	260.17	903.54	51.8123	5241.05	2075.68	-13343.9	839.47
27	DRA T	1106	354.418	1441.89	613.998	1981.09	2453.2	-8892.45	348.445
28	DRA T	1159	238.046	1089.04	315.404	882.909	1208.19	-10005.1	430.505
29	DRA T	1160	235.712	1091.86	454.147	901.746	1265.15	-7930.36	306.405
30	DRA T	1026	427.791	1482.7	722.444	1632.9	1889.12	-6955.52	471.877
31	DRA T	976	736.644	1575.83	1031.71	1955.34	1445.06	-7162.46	384.783
32	DRA T	1039	508.171	1219.94	593.404	981.348	1354.77	-8126.52	424.873
33	DRA T	1106	361.556	1395.88	539.854	1779.28	1629.27	-6586.79	363.774
34	T DRA	1133	294.187	1201.29	483.893	1025.65	1506.65	-8218.39	377.294
35	U CAM	2044	339.219	482.174	-35.5187	6126.84	754.74	-8363.37	936.009
36	S CEP SCAN	1411	182.711	1065.72	282.268	2093.43	2277.05	-7539.14	591.574
37	S CEP	1337	370.545	1616.49	615.361	3061.19	2669.02	-4499.94	636.571
38	V CYG	1004	356.958	1543.18	705.394	1637.99	2136.77	-7646.34	514.153
39	CYG V	1084	298.909	1320.14	414.633	1421.65	1912.64	-9585.8	586.166
40	CYG V	1081	290.297	1333.13	367.809	1555.32	1676.4	-8812.31	549.525
41	CYG V	990	449.868	1616.18	899.356	2170.31	1951.66	-6856.48	628.643
42	CYG V	1007	438.012	1504.45	696.702	1880.83	2135.23	-7370.89	597.307
43	CYG V	1148	185.183	1112.55	304.011	1050.35	2407.78	-9742.82	564.394
44	SCL R	2168	346.218	1908.54	525.475	6518.11	4076.6	-4098.27	965.855
45	R SCL	2233	344.239	1869.32	581.27	6842.3	3929.31	-3813.35	1021.18
46	SCL R	2180	357.52	2105.18	680	7023.98	4892.48	-2807.84	899.524
47	SCL R	2216	395.999	2192.88	709.433	7363.7	5141.98	-3354.3	702.165
48	SCL R	1961	377.85	2038.12	682.663	6365.61	4788.46	-7867.59	878.907
49	SCL R	2272	240.691	1749.46	344.701	5913.26	4575.6	-7091.03	928.474

Table 2.1— Overview of the 50 stars from the sample and their deduced properties. Shown are the auto-fitted blackbody temperatures and the EW for the selected features.

Feature (μm)	Carrier(s)	\underline{a} (μm)	\underline{b} (μm)
2.5 + 2.6	C ₂ H ₂ , CO, HCN and C ₂	2.4	2.9
3.0	C ₂ H ₂ and HCN	2.8	3.4
3.9	C ₂ H ₂	3.5	4.3
5.0	CO and C ₃	3.9	6.1
7.9	HCN and CS	6.5	9.0
11.3	SiC	10.0	13.0
13.7	C ₂ H ₂ and HCN	13.4	14.3

Table 2.2— Features under investigation shown together with their carrier(s) and the adopted integration ranges.

and in some cases a large scatter around the mean fractional EWs. It is interesting to see that at the bottom plots involving the 7.9 μm feature, TU Tau lies clearly outside the region occupied by the other stars. This is already an indication that, indeed, around 6.5 - 9.0 μm TU Tau is different.

To seek out classification schemes and to see whether similar classifications are made based on different schemes, each spectrum is represented by a color. The spectra have been sorted, in ascending order, on blackbody temperature and EW for the features mentioned in Table 2.1. An image is constructed showing in each column a classification scheme. The constructed images are presented in Appendix C. In each image a different column has been linear color coded to make it easier to spot correlations.

Thus far, based upon the color classification maps, no obvious correlations are present. One could argue that there is a slight correlation between the blackbody temperature and the 5.0 μm EW together with an anti-correlation of the 3.9 μm EW. Looking at the figure in which the column for blackbody temperature has been linear color coded, the darker colors and lighter colors more or less stay together in the 5.0 μm EW column, the 3.9 μm column displays mirrored behavior. This could indicate that the CO and C₃ abundances are sensitive to the temperature in the CSE.

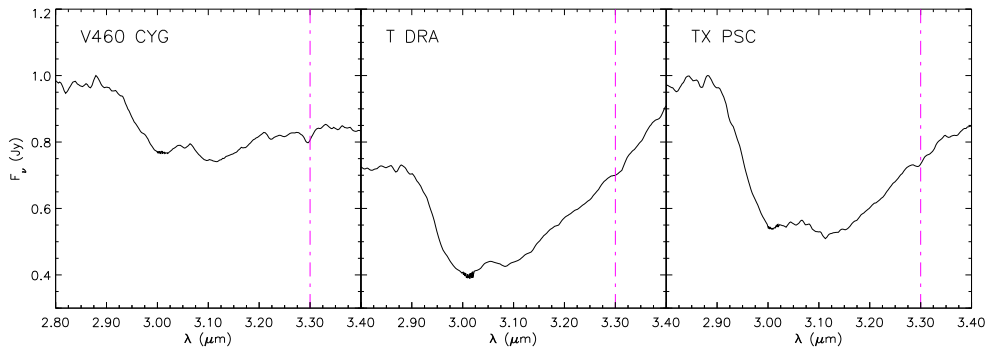


Figure 2.1— Three spectra shown from 2.8 μm to 3.4 μm . Each spectrum has been normalized to the maximum flux level of their entire spectrum. Indicated is the CH₄ absorption feature.

<u>Specie</u>	<u>Feature λ_x (μm)</u>		<u>Feature λ_y (μm)</u>
C ₂ H ₂	2.5 + 2.6	→	3.0
			3.9
			13.7
	3.0	→	3.9
			13.7
			13.7
HCN	2.5 + 2.6	→	3.0
			7.9
			13.7
	3.0	→	7.9
			13.7
			13.7
CO	2.5 + 2.6	→	5.0

Table 2.3— Overview of the features carried by common species and for which plots have been made.

Although no obvious subset around TU Tau is found from these spectral classifications, this doesn't mean that it is impossible to create a subset of appropriate stars. In the next section a more qualitative scheme will be used to select those stars. The results from this section can be used to explain, in some extend, occurring mismatches between TU Tau and the comparison stars.

2.2 A first selection

Before selecting a subset and discarding most of the stars and spectra from further analysis, it is necessary to check for other stars for which residual uIR band emission could be suspected. For this each spectrum has been checked around 3.3, 6.2, 7.6, 7.9, 8.60, 11.2 and 12.7 μm for excess emission when drawing a local continuum and estimating the molecular absorption and at 11.3 μm the SiC emission. A list of possible candidates was created and the list was rechecked for possible candidates. This resulted in no other stars, besides TU Tau, for which residual emission around the uIR bands is suspected.

Reassured by the result that TU Tau is rather unique, we continue with the determination of the subset. The criteria on which the selection is based are set by the spectral characteristics of TU Tau. These include:

- Reasonable flat λF_ν versus λ graph
- Clear 2.9 - 3.4 μm absorption feature
- Clear 4.3 - 6.1 μm absorption feature
- Clear bump around 10.0 - 12.5 μm

- Clear bump around 13.5 - 14.0 μm

This exercise resulted in a subsample consisting of the spectra from 9 different carbon-rich AGB stars. The 9 stars, together with TU Tau, are presented in Table 2.4. The stars in the subsample for which several spectra are available the spectra showing the most resemblance with that of TU Tau have been selected. This effected only two stars, V460 Cyg and R Scl for which, respectively, spectrum 7 and 44 are used in further analyzes. In Fig. 2.5 are the spectra from the subset, plus TU Tau, in the connected region around the UIR bands (4.0 - 15 μm), plotted. This plot shows the large variations present around the 7.6 and 7.9 μm UIR bands, already suggesting that matching TU Tau, in this region with the other stars will be difficult and that the deduced 7.6 and 7.9 μm profiles can depend a lot on the selected comparison star.

#	Name	T_{BB} (K)	d
3	V AQL	2912	0.73
5	TU TAU	1912	0.38
4	Y CVN	2682	1.2
6	S SCT	2395	0.39
7, 8 ^a	V460 CYG	2759	1.2
11	W ORI	2092	1.8
12	RY DRA	2325	0.82
14	VX AND	2379	0.43
35	U CAM	1964	1.0
44 - 49 ^b	R SCL	2427	1.1

^aSpectrum # 7 selected.

^bSpectrum # 44 selected.

Table 2.4— The subsample: selected carbon-rich AGB stars with fitted blackbody temperatures and distance factor.

The color classification map in Fig. 2.2 shows the locations of TU Tau and the subset. The map indicates that, at least for the blackbody temperature, the 5.0 μm and 13.7 μm , and more or less for the 2.5 + 2.6 μm , 7.9 μm and 11.3 μm , stars similar to TU Tau have been selected, which strengthens confidence in the subsample.

W Ori, ID 11, displays the most similarities with TU Tau. Already the IRAS and UKIRT spectra of W Ori and TU Tau have been used by Buss et al. (1991) and Speck & Barlow (1997) to find evidence for PAH features in TU Tau. When making the assumption that W Ori and TU Tau are the same, except for their distance and UIR bands, thus using eq. (2.2) and assuming for $F_{\nu(\text{C-star})}(\lambda)$ eq. (2.5), further taking for the optical depth $\tau_{\text{TU Tau}}(\lambda) = \tau_{\star}(\lambda)$, it is possible to determine the residual spectrum. Take $d = 0.17$, which puts W Ori roughly at the same distance as TU Tau, and for the distance downscaled spectrum the dark curve in Fig. 2.3 is found.

$$F_{\nu(\text{C-star})}(\lambda) = d \cdot F_{\nu(\star)}(\lambda)e^{\tau_{\star}(\lambda)} \quad (2.5)$$

In the inset of Fig. 2.3 the residual spectrum is plotted. Indicated with the blue dash-dotted lines are the centers of the UIR bands. Around most of these locations residual emission is found.

However, while the agreement is reasonable for such a direct comparison, spectral structure particularly near strong absorption bands remain. A statistical approach with the entire sample might improve the fit of the absorption bands. For this the nine spectra have been normalized, using eq. (2.6), and the usual statistical formulas, eq. (2.7) have been applied to get the mean, $\pm 1 \sigma$, minimal and maximum spectrum.

$$F_{\nu(\star)}^{\text{normalized}}(\lambda) = \frac{F_{\nu(\star)}(\lambda)}{\max(F_{\nu(\star)})} \tag{2.6}$$

$$\begin{aligned} \bar{F}_\nu(\lambda) &= \frac{1}{9} \sum_{i=1}^9 F_\nu^{(i)}(\lambda) & \sigma^2(\lambda) &= \frac{1}{8} \sum_{i=1}^9 (\bar{F}_\nu^{(i)}(\lambda) - F_\nu^{(i)}(\lambda))^2 \\ F_\nu^{\max}(\lambda) &= \max_{i=[1,9]} F_\nu^{(i)}(\lambda) & F_\nu^{\min}(\lambda) &= \min_{i=[1,9]} F_\nu^{(i)}(\lambda) \end{aligned} \tag{2.7}$$

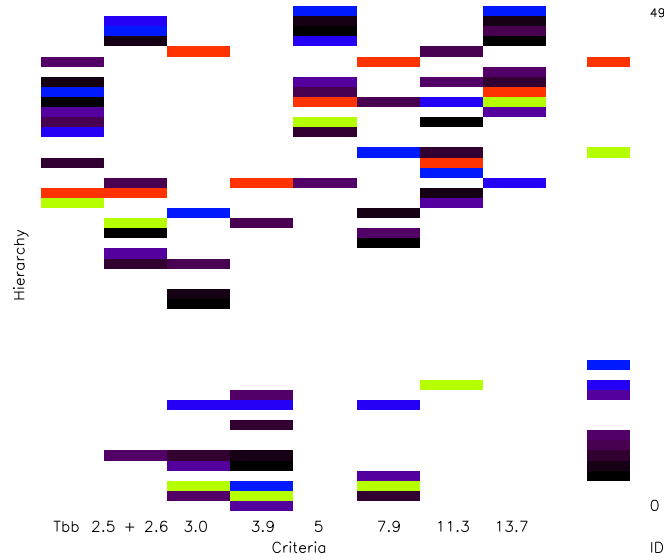


Figure 2.2— Classification color map showing the locations of the stars from the subset. The spectrum ID has been linear color coded.

The resulting spectra are presented in the top panel of Fig. 2.4. In the bottom panel the comparison with TU Tau is made. The same approach as with W Ori is used, with $d = 147$ (eq. (2.5)). The inset in the bottom panel shows, again, the residual spectrum. At some places the fit of the MEAN spectrum with TU Tau seems to be better than with that of W Ori. However the match of the stronger absorption bands is still very poor. It is evident that corrections for the absorption bands should be made. But before turning to this, the continua are investigated using blackbody curves.

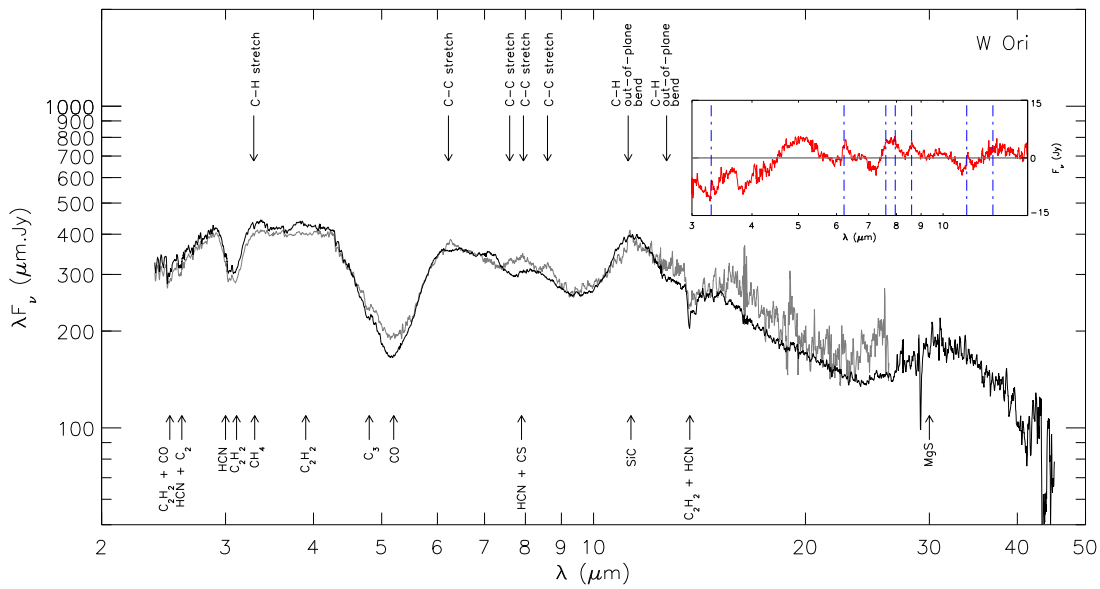


Figure 2.3— Distance downscaled spectrum of W Ori, dark line, and the spectrum of TU Tau, gray line. In the box the residual spectrum is shown. Indicated with the blue dash-dotted lines are the centers of the UIR bands.

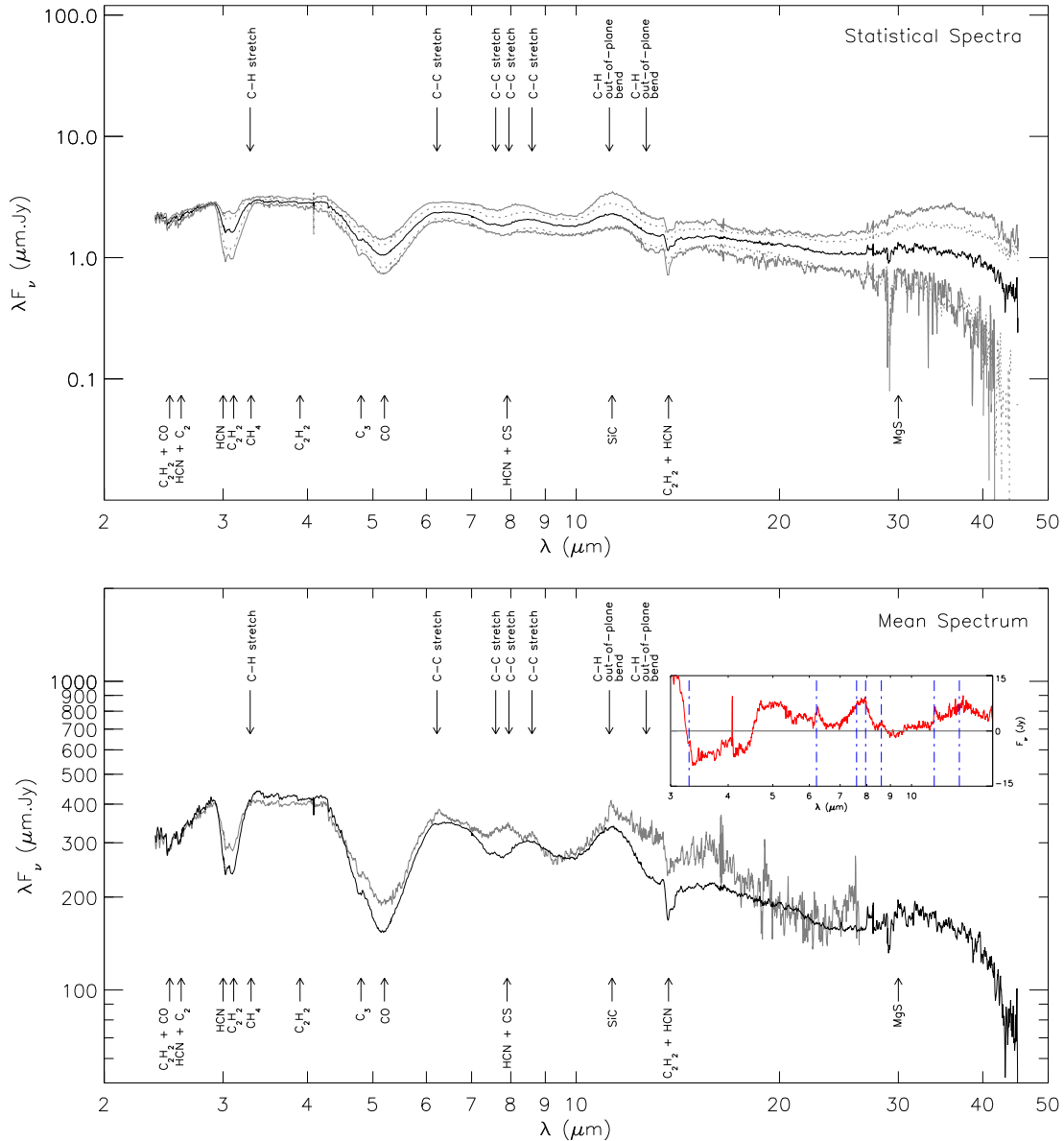


Figure 2.4— Top: The mean normalized spectrum from the subsample of nine carbon-rich AGB stars. The dark solid curve is the mean, the dotted curves are the $\pm 1\sigma$ curves and the gray solid curves represent the maximum and the minimum spectrum. Bottom: distance scaled mean spectrum, dark line, with the spectrum of TU Tau, gray line. In the insert the residual is plotted. Indicated with the blue dash-dotted lines are the centers of the UIR bands.

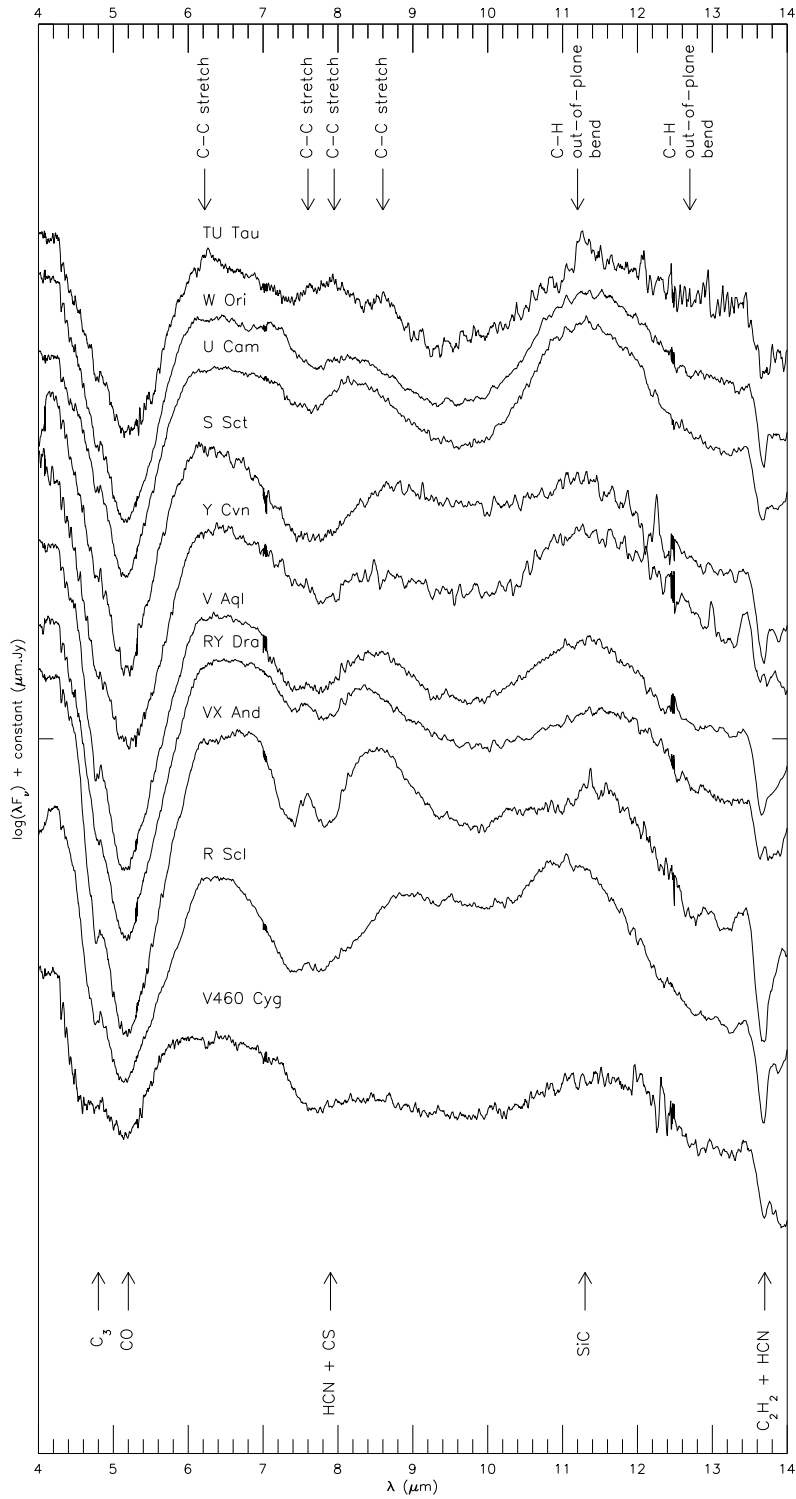


Figure 2.5— Overview of the spectra in the subsample. Indicated above the spectra are the locations of the possible PAH features with their modes. Indicated below the spectra are some of the molecular bands and SiC.

2.3 Blackbody fits

Blackbody physics is relatively easy since it is clear what is happening. And very important, the physics is described by a single parameter, the temperature (T_{BB}). When introducing a parameter d correcting for distance effects, the blackbody equation becomes (2.8).

$$F_{\nu(\text{BB})}(\lambda) = d \cdot \frac{4\pi hc}{\lambda^3} \left(e^{\frac{hc}{\lambda k T_{\text{BB}}}} - 1 \right)^{-1} \quad (2.8)$$

The reason for fitting blackbodies to the spectra is to correct for, to some extent the global spectral differences between the stars of the subsample and TU Tau. These global differences are put in terms of different stellar temperatures and effect the underlying continua of the spectra.

An interactive blackbody fit routine, part of the `osia` (see section 1.5.1), has been used to fit the blackbodies to the spectra. The routine uses an arbitrary number of points ($n > 2$), chosen by the user, to fit on. Here, three regions are assumed to contain continuum points. In each of these regions one point has been selected. The three regions are:

1. Maximum around 2 - 3 μm . This to avoid the strong absorption features around 2.5 and 2.6 μm due to C_2H_2 , CO , HCN and C_2 .
2. The 17 μm point. Assumed to be an isolated continuum point.
3. Fixed between 4 - 5 μm to get the start of the 13.7 μm feature, due to C_2H_2 , at zero.

Table 2.4 presents the fitted blackbody temperatures and the distance factors. The autofitting procedure, used in section 2.1, agrees to within 15 K with the temperatures found here. As expected, the autofitting routine underestimated the blackbody temperatures, but the small difference of only 15 K is remarkable.

The panels to the left in Fig. 2.6 present the nine spectra from the subsample and TU Tau with the fitted blackbodies. The residuals are plotted in the panels to the right. The fit to TU Tau is very poor. This could be due to extra emission from PAH plateaus, but is uncertain. Overall, the blackbody fits are poor. The residual spectra do flatten out with the subtraction of the blackbodies, but they more or less overshoot. The residual spectra show a concave profile, whereas the original spectra are more convex.

The blackbody fits to the spectra are very poor and show that it is difficult to use a global description for the continua. Focusing on the molecular bands (see section 2.2) and using local descriptions for the continua could prove to be a more fruitful strategy.

2.4 The second and final selection

From W Ori and the MEAN spectrum it became obvious that $\tau_{\text{TU Tau}}(\lambda) \neq \tau_{\star}(\lambda)$ (section 2.2). From the previous section it became clear that using global continua, such as blackbodies, is not the way to go. The new strategy is to apply first order corrections to the optical depth and use power-laws to describe, locally, the continuum.

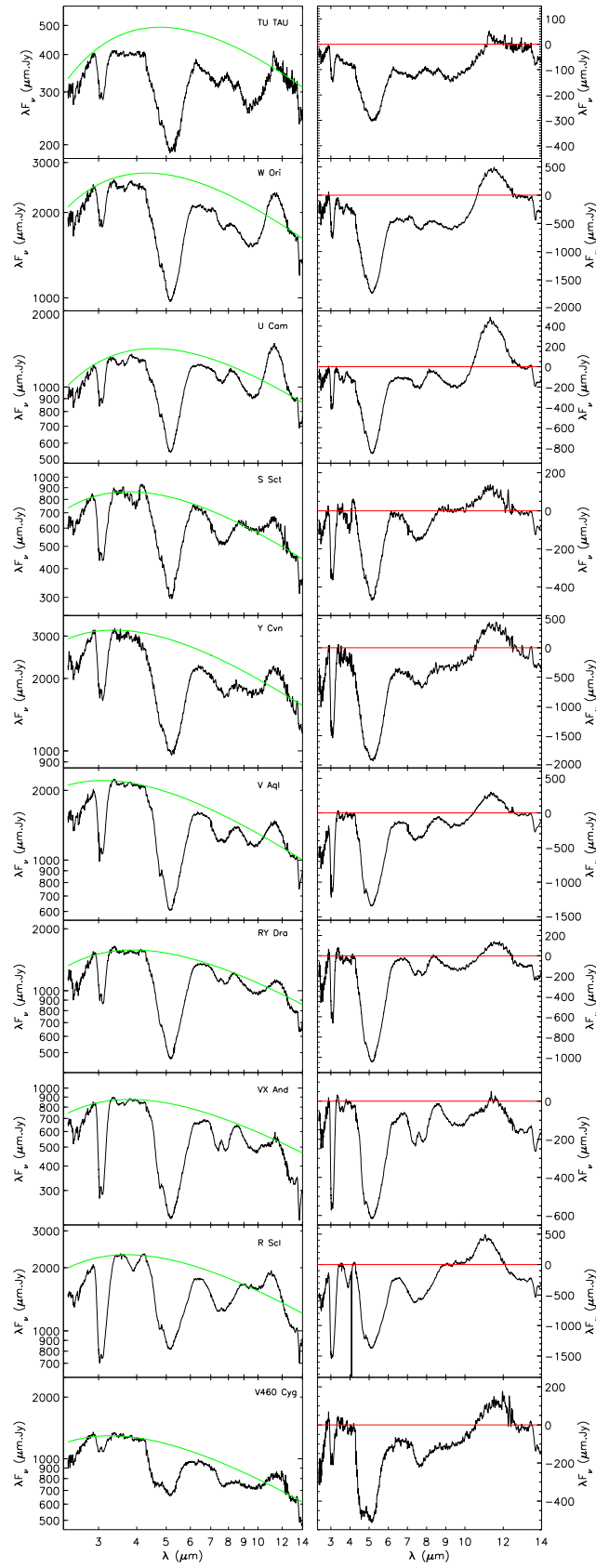


Figure 2.6— Left panels: the spectra from the subsample with fitted blackbody curves. Right panels: residual spectra.

The first order correction to the optical depth is given by eq. (2.9), where t is the correction term.

$$t \cdot \tau_{\star}(\lambda) = \tau_{\text{TU Tau}}(\lambda) \quad (2.9)$$

The description for the power-law is given in eq. (2.10), where γ is the power-law index and c is the power-law constant.

$$F_{\nu(\text{C-star})}(\lambda) = c \cdot \lambda^{-\gamma} \quad (2.10)$$

Combining this with eq. (2.5) results in eq. (2.11). The “’” is put above the d for naming conveniences later.

$$F_{\nu(\star)}(\lambda) = d' \cdot c \cdot \lambda^{-\gamma} \cdot e^{-\frac{\tau_{\text{TU Tau}}(\lambda)}{t}} \quad (2.11)$$

Lets assume, for simplicity, that all stars in the subsample, including TU Tau, have the same local continuum around 3.0 - 10.0 μm and such, that $\gamma = 1$. Putting this into the boxed part of eq. (2.2) and multiplying with λ results in eq. (2.12), where $d \equiv c \cdot d'^{-t}$

$$\lambda \cdot F_{\nu(\text{TU Tau})}(\lambda) = \lambda \cdot F_{\nu(\text{UIR})}(\lambda) + d \cdot [\lambda \cdot F_{\nu(\star)}(\lambda)]^t \quad (2.12)$$

The UIR bands of interest are located in four regions, 3.0 - 4.0 μm , 4.0 - 7.0 μm , 7.0 - 10.0 μm and 10.0 - 13.0 μm . Three spectra, for each region, have been selected from the subsample for comparison with TU Tau. The spectra have been selected based on similarities in the four regions, one having the most similarities, one having the second most similarities and one having the least similarities. This is to constrain the variations in the resulting residual UIR band profiles.

For each region W Ori has been selected as the star with the most similarities, S Sct as the star with the second most similarities and VX And as the star with the least similarities with TU Tau. That the selection of stars for each region resulted in the same three stars, puts confidence in the general characteristics for the deduced profiles.

As a check, Fig. 2.7 shows that the power-law approximation for the continuum, with $\gamma = 1$, isn't such a bad first choice for these three spectra. The derived formula will now be applied to the three spectra from the selection and values will be fitted to d and t .

2.4.1 4.0 - 7.0 μm

One of the dominating features in spectra from carbon-rich AGB stars is the absorption band due to C_2H_2 around 5.0 μm . The spectra for W Ori, S Sct and VX And have been scaled, using eq. (2.11), to fit this band in TU Tau. The residual spectrum has been determined using eq. (2.12). The fitted values for d and t are presented in Table 2.5. The left panel in Fig. 2.8 presents the scaled spectra (left boxes) and the residual spectra (right boxes). The UIR band around 6.2 μm , indicated with the blue dash-dotted line, show residual emission in all three residual spectra. The results with W Ori give the best fit in the 6.2 μm band.

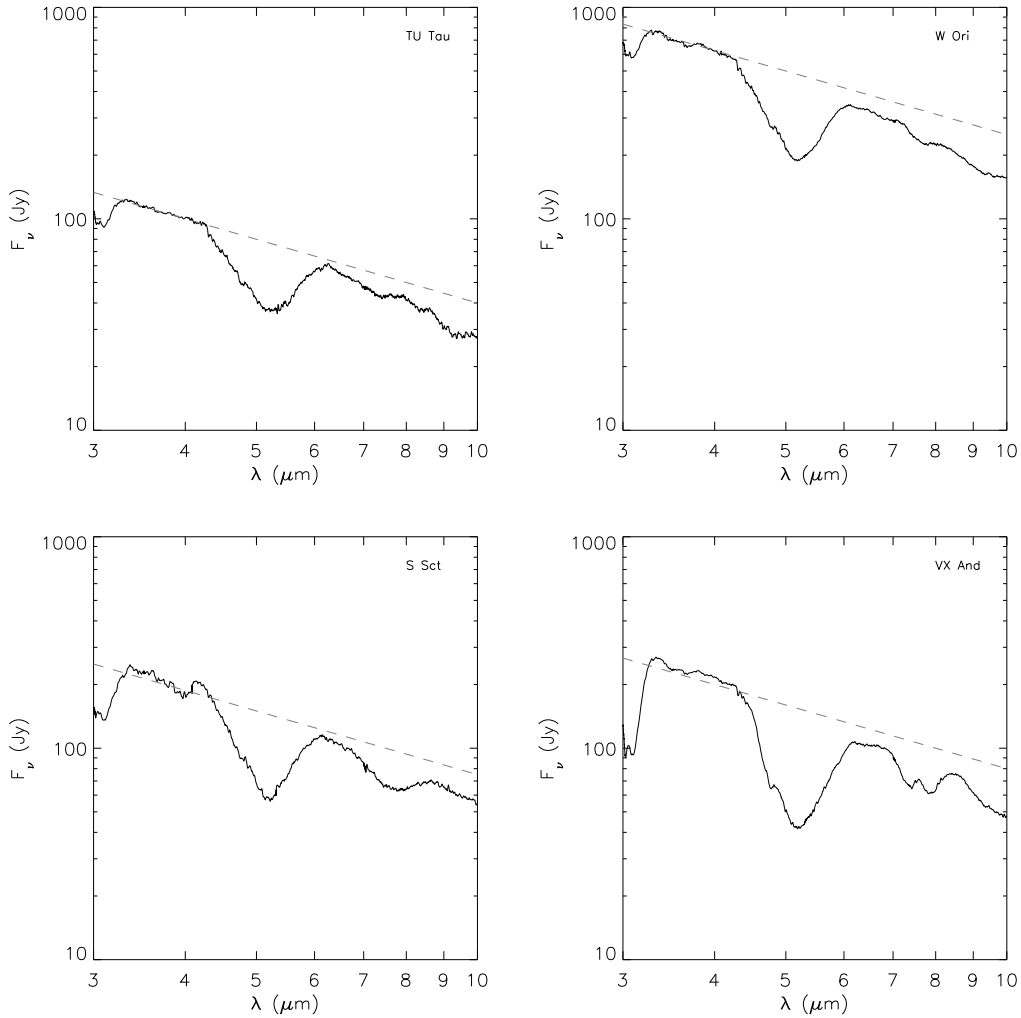


Figure 2.7— Power-law fits, with power-law index $\gamma = 1$, to the local continuum (dashed lines) for the selected three stars (see text).

	4.0 - 7.0 μm			7.0 - 10.0 μm		
	<u>W Ori</u>	<u>S Sct</u>	<u>VX And</u>	<u>W Ori</u>	<u>S Sct</u>	<u>VX And</u>
d	0.66	3.7	7.5	0.66	3.7	7.5
t	0.82	0.69	0.60	0.82	0.69	0.60

Table 2.5— Scaling parameters (*method 1*).

2.4.2 7.0 - 10.0 μm

From 7.0 - 10.0 μm the absorption bands due to HCN and CS are dominant. The two bands tend to overlap in most carbon-rich AGB stars. Due to the large variation in the way the two bands overlap, it is very difficult to match these bands in W Ori, S Sct and VX And with those in TU Tau (see also section 2.2). To overcome this problem the fitted values for d and t for 7.0 - 10.0 μm have been adopted (Table 2.5). This is somewhat justified since for each band the same three stars were selected. The right panel in Fig. 2.8 presents the scaled spectra (left boxes) and the residual spectra (right boxes). The UIR bands around 7.6, 7.9 and 8.6 μm are indicated with the blue dash-dotted lines.

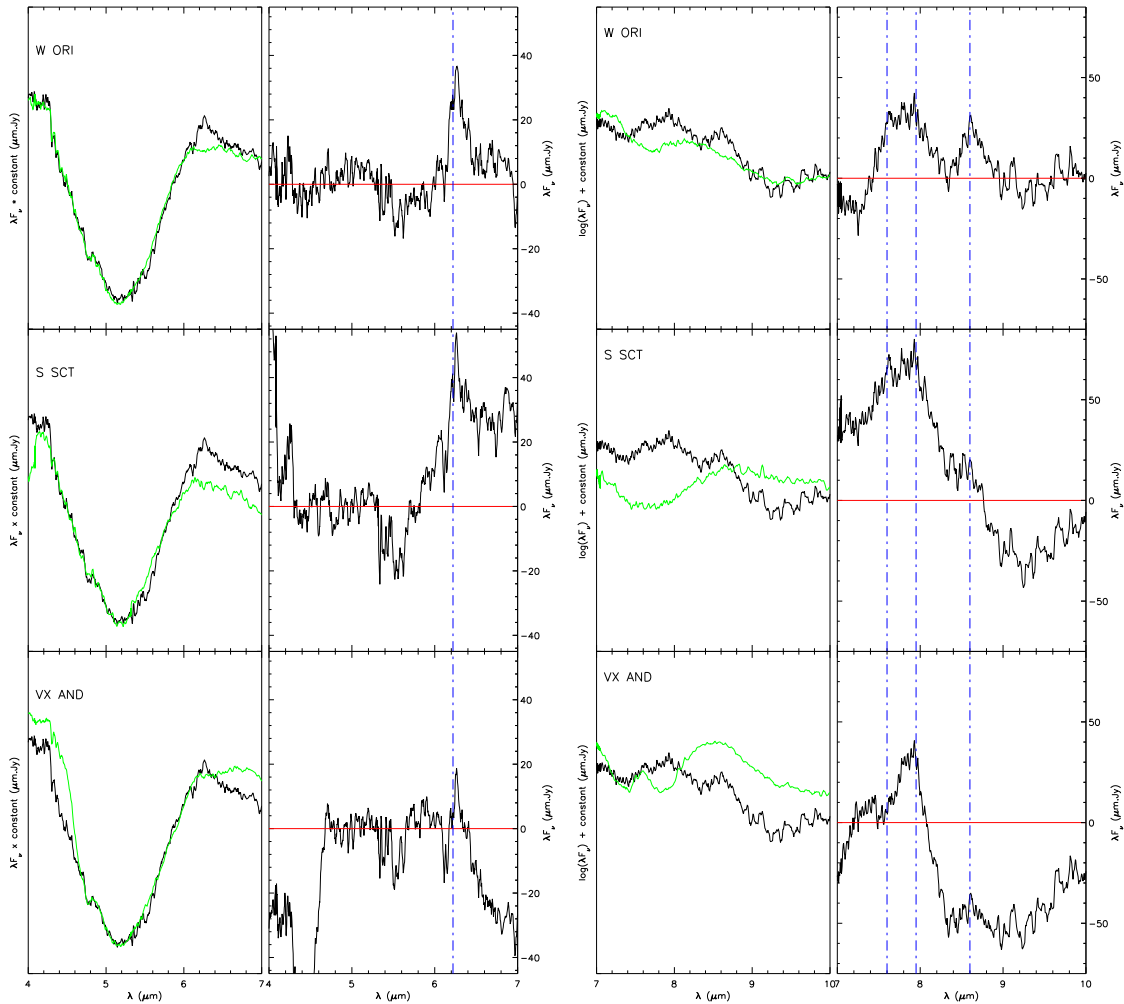


Figure 2.8— Left: Scaled spectra of the three selected stars from 4.0 - 7.0 μm . Right: Scaled spectra of three selected stars from 7.0 up to 10.0 μm . In both panels the boxes on the left present the scaled profiles (green) and TU Tau. The boxes on the right present the residual spectra.

	TU Tau	R^2	W Ori	R^2	S Sct	R^2	VX And	R^2
d	-	-	0.1640	0.997	0.5340	0.991	0.5233	0.973
c	622.0	0.849	716.7	0.845	419.24	0.584	558.57	0.759
γ	1.3485		1.4461		1.0256		1.1900	
t	-	-	0.8228	0.996	0.6923	0.993	0.4721	0.989

Table 2.6— Scaling parameters using *method 2*, with linear correlation coefficients R^2 .

The result with W Ori shows again the best fit in the UIR bands. With S Sct and VX And there seems to be a continuum mismatch. This is not unexpected, since Fig. 2.7 clearly shows the mismatch of the power-law continuum around 7.0 - 10.0 μm . This is fixed by reintroducing the power-law index γ as a variable.

Using $c_{\text{TU Tau}}$ and $\gamma_{\text{TU Tau}}$ to indicate the power-law constant and power-law index for TU Tau and c_{\star} and γ_{\star} to indicate the power-law constants and power-law indexes for the selected stars, eq. 2.13 is written.

$$F_{\nu(\text{TU Tau})}(\lambda) = F_{\nu(\text{UIR})}(\lambda) + d^t \cdot \frac{c_{\text{TU Tau}}}{c_{\star}^t} \cdot \lambda^{-(\gamma_{\text{TU Tau}} - \gamma_{\star} \cdot t)} \cdot [F_{\nu(\star)}(\lambda)]^t \quad (2.13)$$

To illustrate the process, take a look at Fig. 2.9. The top-left box displays the flux from W Ori plotted against the flux from TU Tau. Note that the spectra have been rebinned to the same wavelength grid (see section 1.5), so this is justified. The plot suggest a linear relationship. The least square fit, with no constant term, to the data results in a slope of 0.164. This is d'^{-1} from eq. (2.11) and should be interpreted as the combined correction factor for the difference in distance and stellar radii of the two stars.

In the top-right panel the spectra for TU Tau, W Ori and the distance scaled spectrum for W Ori (dashed line) are drawn. Also the fitted power-laws are shown in this panel (dotted lines). The power-law has been fitted between 3.2 and 4.5 μm , outside the major absorption features. A least square fit to the data in this region results in $c_{\text{TU Tau}} = 622.0$, $\gamma_{\text{TU Tau}} = 1.349$, $c_{\text{W Ori}} = 717$ and $\gamma_{\text{W Ori}} = 1.45$.

Next, in the middle-left panel, the optical depth of distance scaled W Ori is plotted against the optical depth of TU Tau. Again a straight line has been fitted between 3.2 and 4.5 μm . This resulted in $t = 0.800$. In the middle-right panel the optical depth profile of TU Tau, distance scaled W Ori and the corrected optical depth of distance scaled W Ori are drawn (dashed line).

$F_{\nu(\text{C-star})} e^{-\tau_{\text{TU Tau}}(\lambda)}$ is plotted as the dashed line in the bottom-left box. Also the spectrum from TU Tau is drawn again. In the final panel the residual is plotted.

Table 2.6 presents the fitted values for TU Tau, W Ori, S Sct and VX And. Fig. 2.10 and Fig. 2.11 illustrate, respectively, the process for S Sct and VX And.

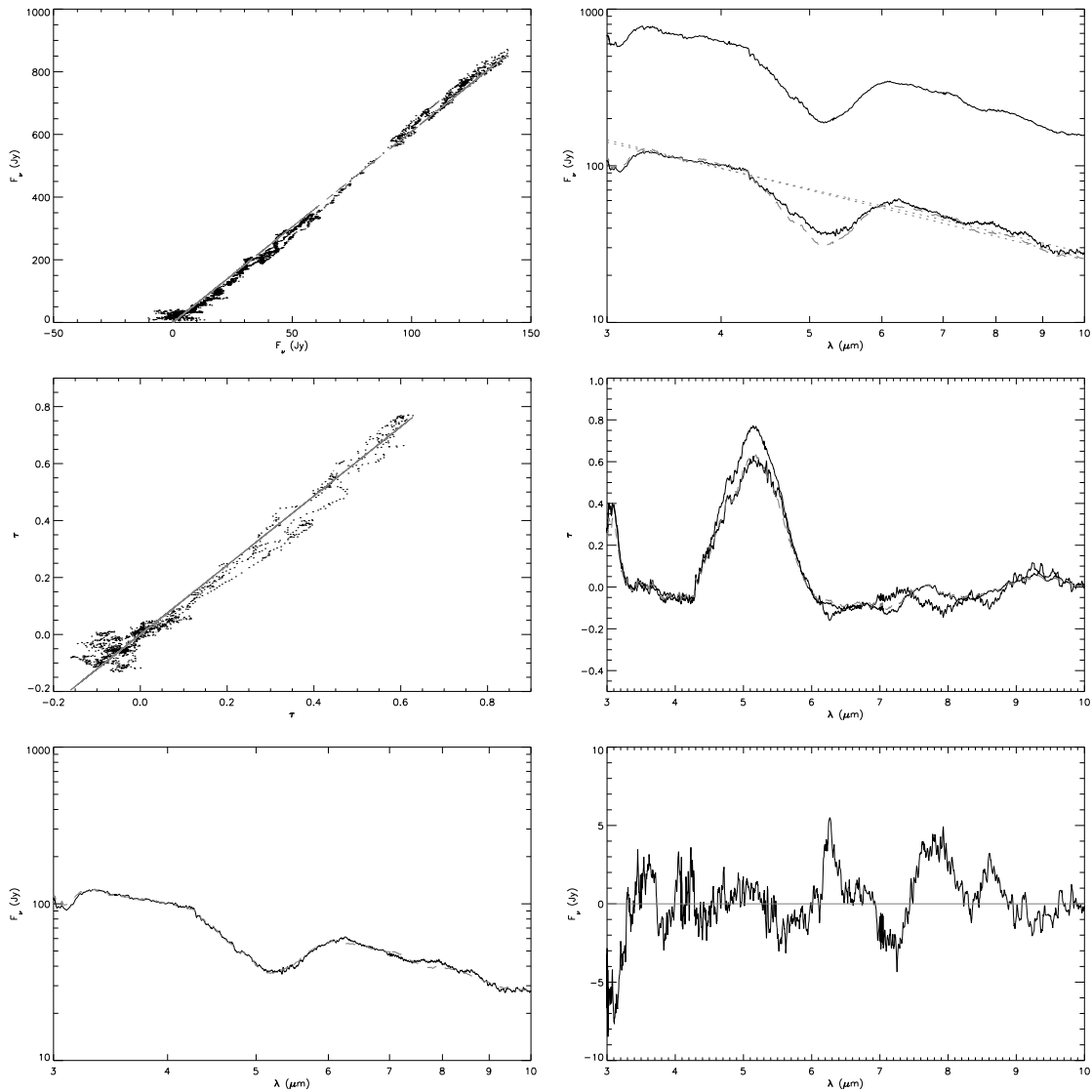


Figure 2.9— *method 2* fitting routine with W Ori as selected comparison star. See text for details.

$$d_{method\ 1} = d^t \cdot \frac{C_{TU\ Tau}}{c_{\star}^t} \quad (2.14)$$

The determination of d and t for eq. (2.12) were done manually (*method 1*). Now however, with the fit routine from *method 2* available it is possible to determine these parameters more systematically. This is done by demanding that $\gamma = 1$. But since these results are similar to the previous ones, they are presented in the appendices (appendix D). To state the similarities, take a look at W Ori. Table 2.5 gives $d = 0.66$ and $t = 0.82$. Table D.1 gives, for W Ori, $t = 0.82$. $d_{method\ 1}$ is here found through eq. (2.14) and gives as result $d = 0.68$, thus showing that the results are indeed similar.

Comparing the values from Table 2.5 (*method 1*) with those from Table 2.6 (*method 2*) shows

that t doesn't differ much and that it is mostly the continuum is responsible for the differences. Except for VX And, which also has a large correction on t . But this is not totally unexpected, since VX And shows the least similarities with TU Tau and is therefore suspected to be more sensitive to variations on the fitted parameters.

Table 2.6 also presents the linear correlation coefficients, which are very good. The value for the continuum fit for S Sct is somewhat low. This is due to exceptionally strong absorption in some overtones of C_2H_2 between 3.2 and $4.0 \mu m$, which gives an extra dip in the region where the power-law is fitted.

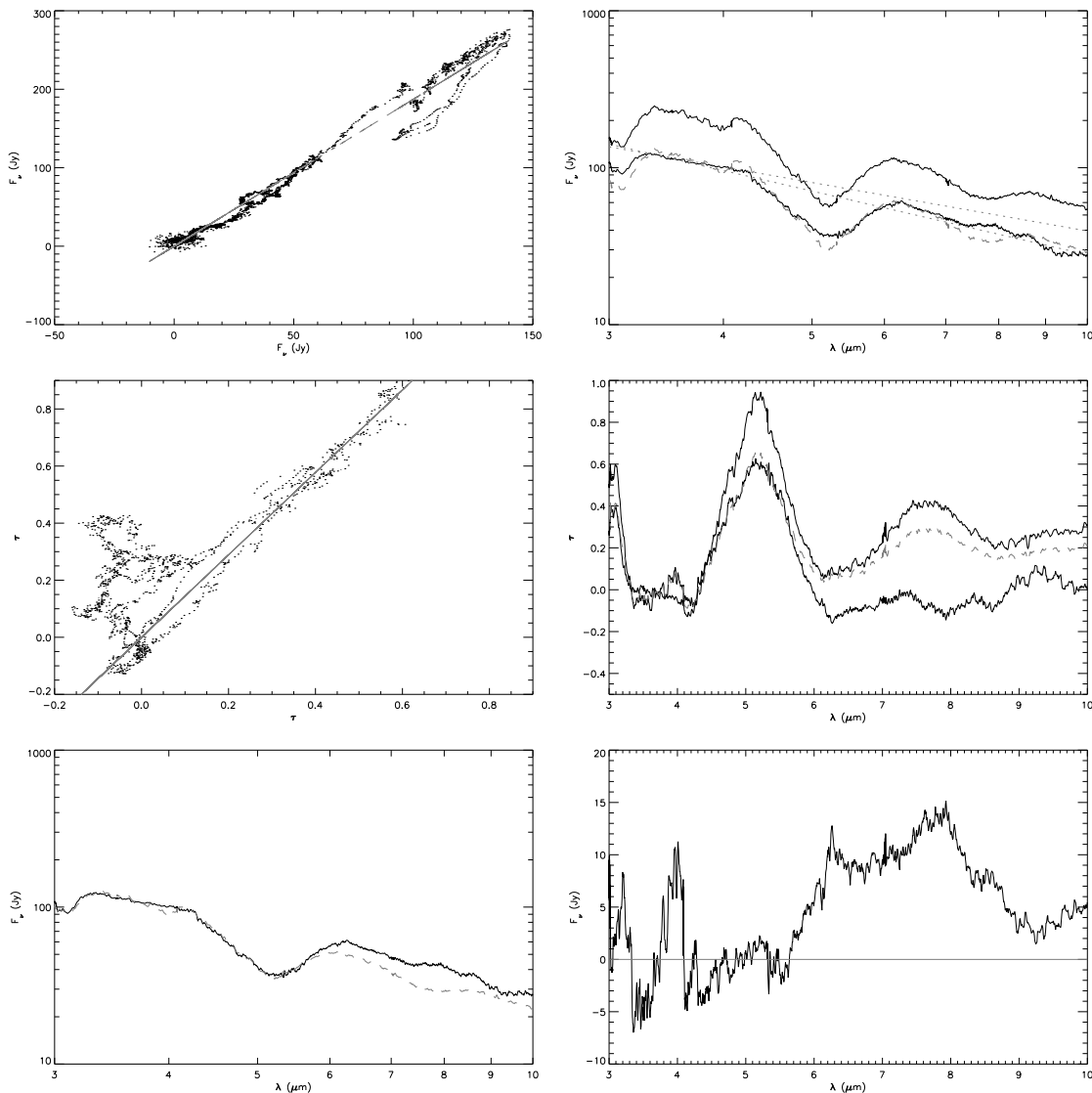


Figure 2.10— *method 2* fitting routine with S Sct as selected comparison star. See text for details.

2.4.3 10.0 - 13.0 μm

Around 11.2 μm the dominant feature due to SiC is located. The SiC is in emission, so a different strategy has to be adopted to match the feature from W Ori, S Sct and VX And with that from TU Tau. For the spectrum of the comparison star eq. (2.15) is written, where $f_{\text{SiC}}(\lambda)$ is the SiC feature, which is assumed to be generic for all carbon-rich AGB stars.

$$d \cdot F_{\nu(\star)}(\lambda) = c_{0(\star)} + c_{1(\star)} \cdot \lambda + f_{\text{SiC}}(\lambda) \quad (2.15)$$

Then similar for TU Tau eq. (2.16) can be written.

$$F_{\nu(\text{TU Tau})}(\lambda) = F_{\nu(\text{UIR})}(\lambda) + c_{0(\text{TU Tau})} + c_{1(\text{TU Tau})} \cdot \lambda + f_{\text{SiC}}(\lambda) \quad (2.16)$$

Combing both gives eq. (2.17).

$$F_{\nu(\text{TU Tau})}(\lambda) = F_{\nu(\text{UIR})} + d \cdot F_{\nu(\star)}(\lambda) + (c_{0(\text{TU Tau})} - c_{0(\star)}) + (c_{1(\text{TU Tau})} - c_{1(\star)}) \cdot \lambda \quad (2.17)$$

The manually fitted values to c_0 , c_1 and d are presented in Table 2.7. The left panel in Fig. 2.12 displays the spectra for TU Tau and the three selected stars between 10.0 - 13.0 μm , together with the matched continuum (in green). The panel in the middle displays the spectra after subtracting the continuum, together with TU Tau (in gray). The right panel displays the residual spectra. Indicated with the blue dash-dotted lines are the centers of the UIR bands.

The result with W Ori show again the best fit in the UIR band. Indications for the presence of the UIR band around 12.7 μm are only seen for VX And as selected companion star.

	c_0	c_1	d
TU Tau	40	-1.2	-
W Ori	26	-0.10	0.10
S Sct	89.3	-0.5	0.71
VX And	7.14	-84.3	0.71

Table 2.7— Continuum and scaling parameters between 10.0 - 13.0 μm .

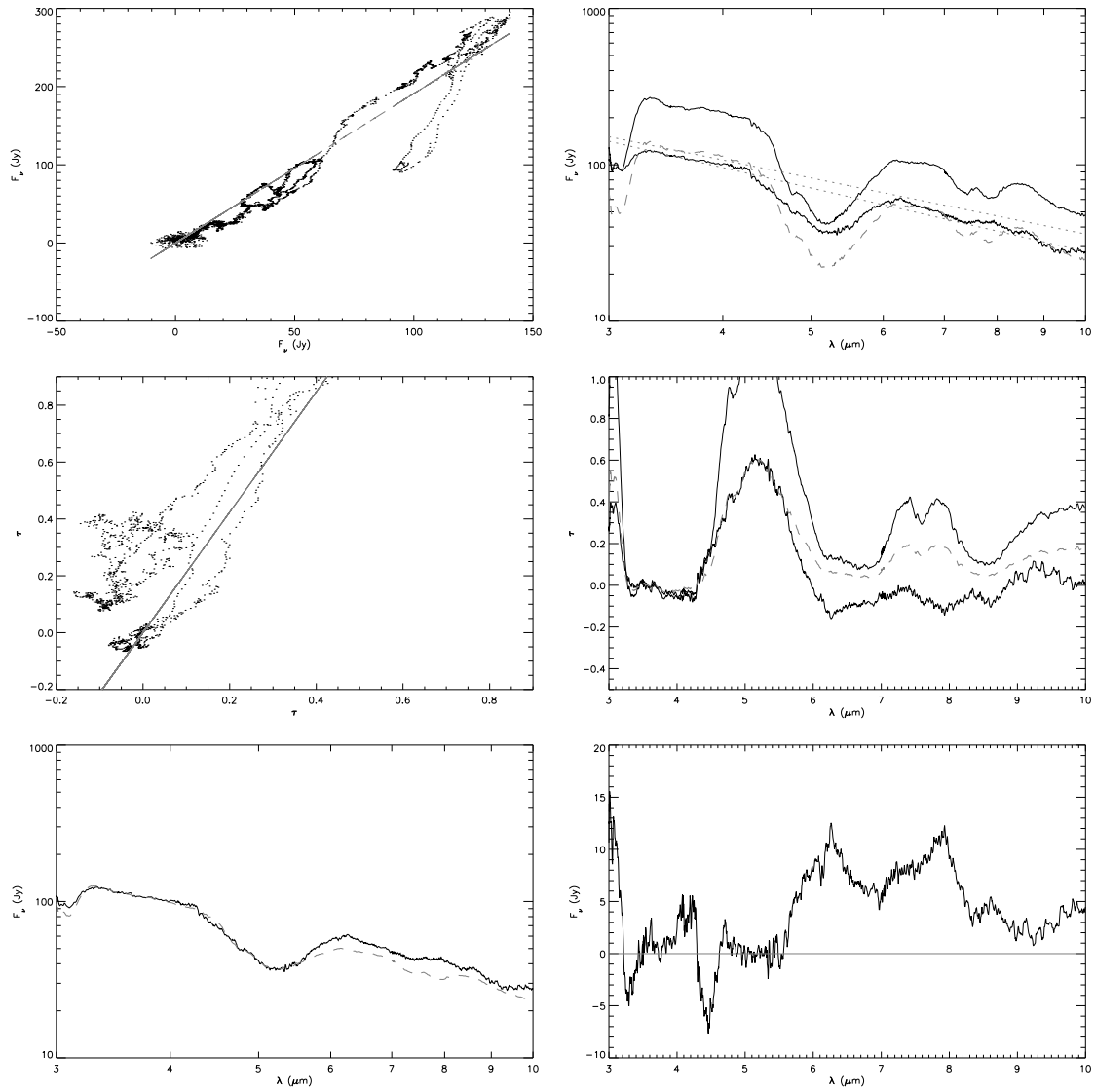


Figure 2.11— *method 2* fitting routine with VX And as selected comparison star. See text for details.

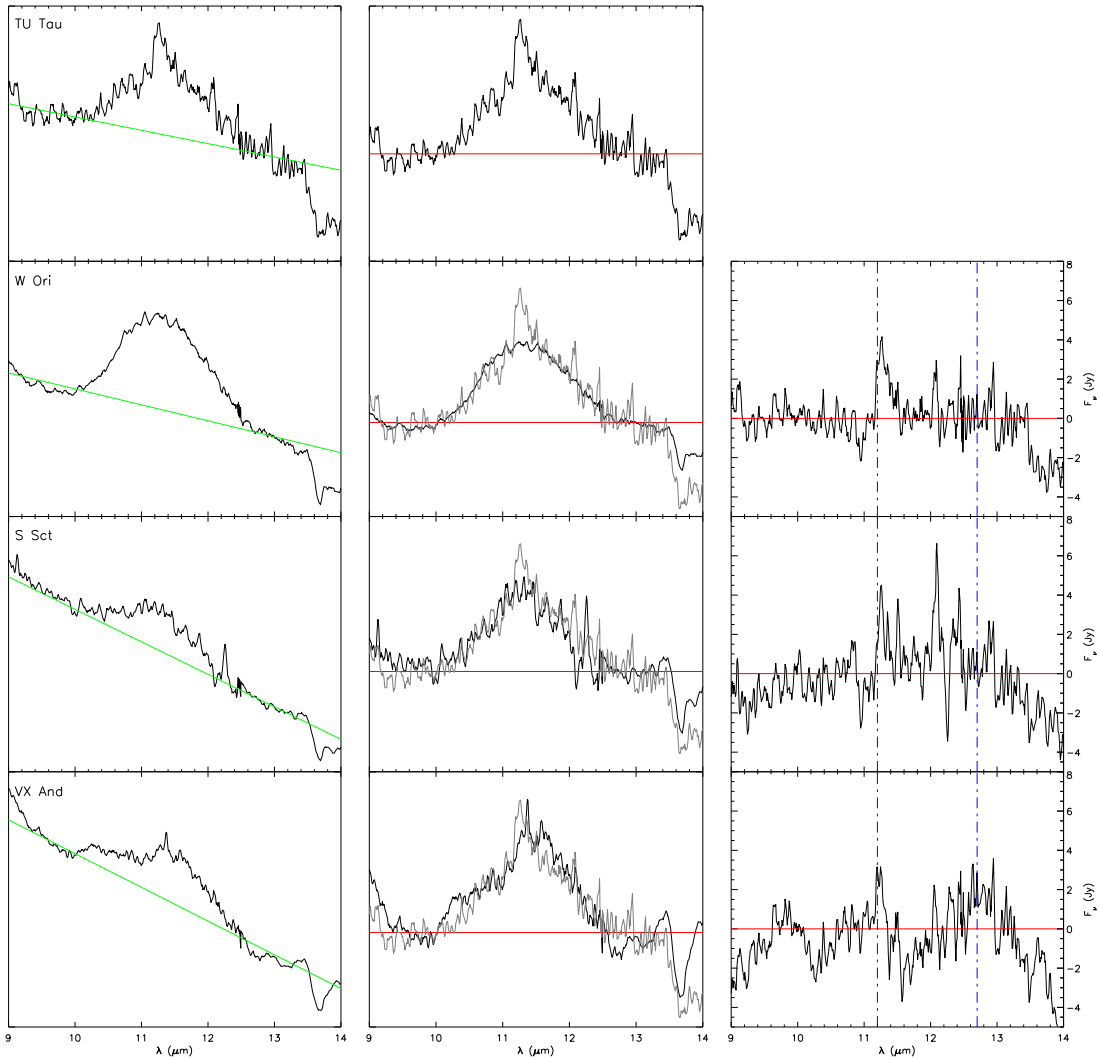


Figure 2.12— Matching the SiC emission of TU Tau.

2.4.4 3.0 - 4.0 μm

Around 3.3 μm is also an UIR band located. However, the direct surrounding region is dominated by the strong blended absorption bands from C_2H_2 and HCN. Even more, as Fig. 2.1 clearly displays, at 3.28 μm is the absorption feature due to CH_4 . Both the overlap of the C_2H_2 with the HCN absorption band and the presence of the CH_4 features just on top 3.3 μm , make the fitting of the bands to complex. This has therefore not been attempted.

2.5 The residual UIR bands of TU Tau

Essentially two methods have been used to find residual UIR emission in the spectrum of TU Tau. The first method was the comparison to spectra from two single stars, W Ori and MEAN (section

2.2). The second method was the comparison to three selected spectra with corrections for the continuum and optical depth. Because of the mismatch of the molecular absorption bands and the SiC feature in the first method the corrections for the continuum and optical depth were applied. For both methods eq. (2.3) was used to obtain the residual spectra. For the single star comparisons the boxed part in the equation was represented by eq. (2.18).

$$\mathcal{H}(F_{\nu(\star)}(\lambda)) = \begin{cases} d \cdot F_{\nu(\text{W Ori})}(\lambda) \\ d \cdot F_{\nu(\text{Mean})}(\lambda) \end{cases} \quad (2.18)$$

For the method that used corrections for the continuum and optical depth the boxed part in the equation was represented by eq. (2.19).

$$\mathcal{H}(F_{\nu(\star)}(\lambda)) = \begin{cases} d \cdot \lambda^{-1} \cdot [\lambda \cdot F_{\nu(x)}(\lambda)]^t \\ d^t \cdot \frac{c_{\text{TU Tau}}}{c_x^t} \cdot \lambda^{-(\gamma_{\text{TU Tau}} - \gamma_x \cdot t)} \cdot [F_{\nu(\star)}(\lambda)]^t \\ d \cdot F_{\nu(x)}(\lambda) + (c_{0(\text{TU Tau})} - c_{0(x)}) + (c_{1(\text{TU Tau})} - c_{1(x)}) \cdot \lambda \end{cases} \quad (2.19)$$

$x \in \{ \text{W Ori, S Sct, VX And} \}$.

With the residual UIR profiles determined, it is now time to characterize them. The following set of parameters is used to do this:

- λ_0 , line position
- R_a, R_b , line range
- $F_{\nu}(\lambda_0)$, flux at line position
- F , total flux = $\int_R F_{\nu}(\lambda) - F_{\nu(\text{continuum})}(\lambda) d\lambda$
- $\Delta\lambda_1$, equivalent width = $\int_R (F_{\nu}(\lambda) - F_{\nu(\text{continuum})}(\lambda)) d\lambda = (F_{\nu}(\lambda_0) - F_{\nu(\text{continuum})}(\lambda_0)) \cdot \Delta\lambda_2$
- $\Delta\lambda_2$, Full Width at Half Max.
- σ_{λ_0} , noise at the line position = $\sqrt{\sum_x \sigma_x^2}$, where σ_x^2 is the average noise in a $\sim 2 \mu\text{m}$ wide region around the line position.

Also will be investigated:

- Wings and/or flanks.
- Uncertainties introduced by the method.

2.5.1 Single star

The residual spectra for TU Tau have been plotted in Fig. 2.13. The top panel displays the results from comparing TU Tau with W Ori and the bottom panel from comparing TU Tau with the MEAN. Table 2.8, at the end of this section, presents the line positions, line ranges, fluxes at the line positions, total fluxes, equivalent widths, FWHM and the noise at the line positions for the residual UIR band profiles in both spectra. Next are the wings, flanks and the uncertainties introduced by the method for each of the residual UIR band profiles characterized.

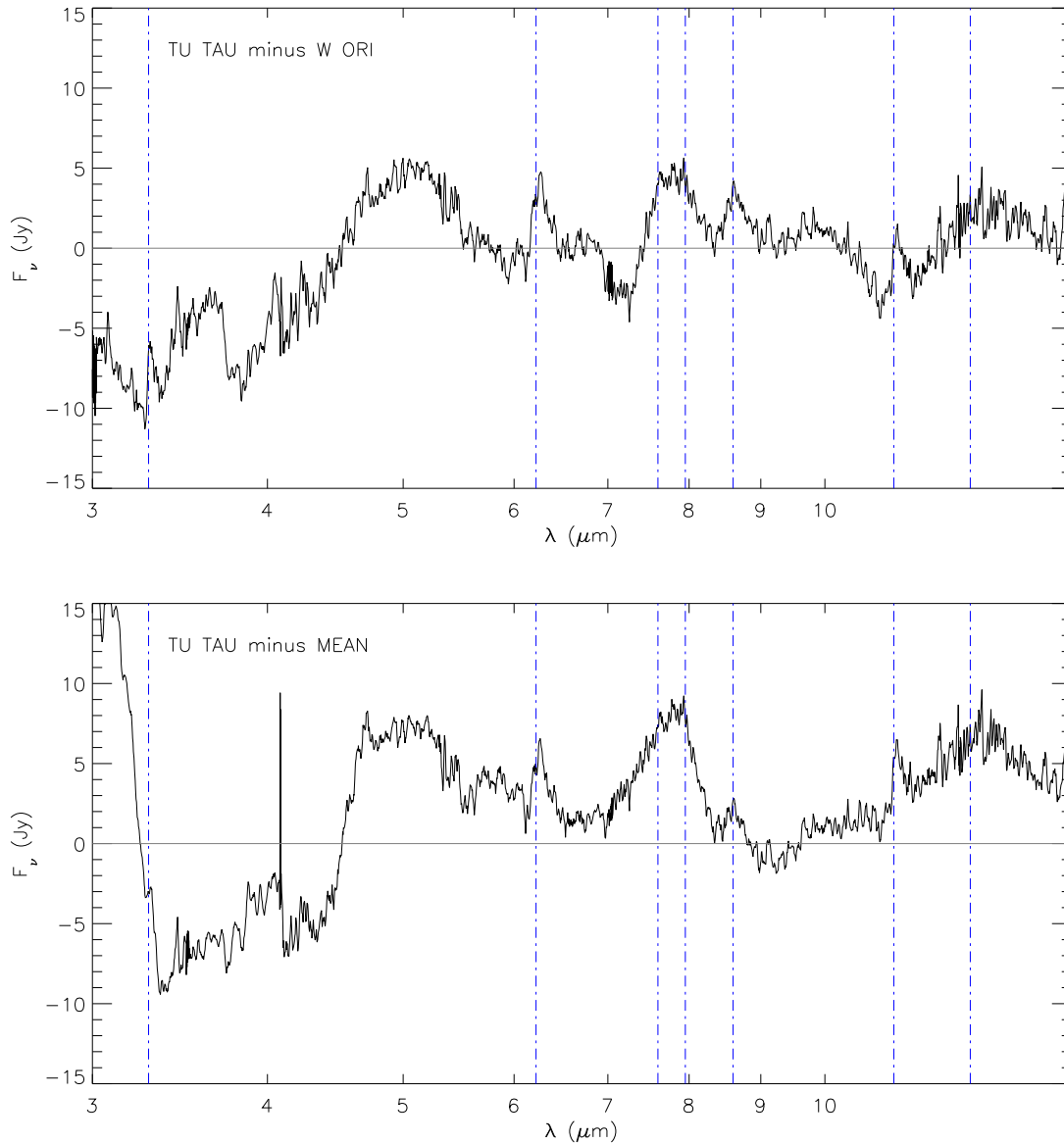


Figure 2.13— Top: residual spectrum from comparing TU Tau with W Ori. Bottom: residual from comparing TU Tau with the MEAN.

The residual UIR band profiles of TU Tau, determined with W Ori, show the following characteristics:

6.22 Sharp and narrow peak, with no wings. The profile reaches zero flux in both tails.

7.60 + 7.95 Double profile, with two clear peak positions. The wings are not extended. The profile for the combined bands reaches zero flux in both tails.

8.60 Sharp profile. the profile reaches zero flux in both tails.

- 11.25** Sharp and narrow peak, however, an offset is present, likely from a discrepancy between the SiC emission band of TU Tau and W Ori. A shift of ~ 5 Jy seems probable.
- 12.7** No clear profile. One might suggest that the broad bump is the $12.7 \mu\text{m}$ UIR band, however this leads to a profile that is too broad. The bump is caused by a continuum mismatch between TU Tau and W Ori in this region.

The distance scaling parameter d is the governing parameter in the method used to derive these profiles. For small variations in d ($d < 0.17$) the match of the molecular absorption bands around $3.0 - 4.0 \mu\text{m}$ is improved. This would lead to a narrower profile around $6.22 \mu\text{m}$, but it would also broaden its wings. The $7.60 + 7.95$ and 8.60 profiles would keep their shape, but a blend between the right wing of the $7.60 + 7.95 \mu\text{m}$ and the left wing of the $8.60 \mu\text{m}$ profile would be introduced. For the $11.25 \mu\text{m}$ profile a decrease in d would lead to an increased offset.

When two spectra are subtracted the noise in the residual spectra will have increased in accordance with eq. (2.20). For two spectra, having approximately the same noise, the noise in the residual spectra will have become $\sqrt{2}$ times the noise in one spectrum. This is a 40% increase. It is a lot harder to give a single quantitative measure of the ‘true’ total statistical error, because it contains the contribution from the uncertainties introduced by the method used to derive the profiles, which are not very clear.

$$\sigma_{\text{residual}} = \sqrt{\sigma_{\text{TU Tau}}^2 + \sigma_x^2}, \quad x \in \{\text{W Ori, S Sct, VX And}\} \quad (2.20)$$

The residual UIR band profiles of TU Tau, determined with the MEAN, show the following characteristics:

- 6.22** Sharp and narrow profile, with no wings. The profile doesn’t reach zero flux in both tails, suggesting a continuum mismatch.
- 7.60 + 7.95** Double profile, with two clear peak positions. The wings are not very extended. The profile for the combined bands reaches only zero in the right tail, suggesting a continuum mismatch.
- 8.60** Sharp profile. The profile reaches almost zero flux in both tails, however, the overshoot in the right tail suggest an offset of ~ 1 Jy.
- 11.25** Sharp and narrow profile, however, an offset is present, which could be as interpreted plateau emission.
- 12.7** No clear profile.

The spectrum of the MEAN has been determined statistically from nine spectra. The nine spectra show a wide spread in their fitted blackbody temperatures, which is a measure for the continuum match between the stars. Also is there a wide variety in the molecular bands for these spectra. This is clearly seen in Fig. 2.5. When adding all these spectra, normalized, and the average spectrum is obtained, then the question still remains how well the continuum and molecular bands of this average spectrum will agree with those from TU Tau. There is no particular physical reason to expect there to be a good match between them. Since TU Tau certainly is not average, it is the coolest star in the subsample (see section 2.2), it is clear that the average spectrum will be hotter, thus not averaging out any effects of continuum mismatches here. As for the molecular bands, averaging out their strength is not the proper way to deal with effects caused by mismatches

in optical depth. The bottom panel in Fig. 2.4 clearly displays the continuum and optical depth mismatches.

Examining the influence of the distance scaling parameter d leads, more or less to the same conclusions as with comparing TU Tau to W Ori. Decreasing d gives a better match for the molecular absorption bands around 3.0 - 4.0 μm . For the 11.25 μm profile a decrease in d would lead to an increased offset.

Giving a quantitative measure for the ‘true’ statistical error here is very difficult, because by adding 9 spectra the statistical will go down, but the systematic errors due to differences in T_{BB} or such will propagate.

2.5.2 Continuum and optical depth corrections

The residual spectra for TU Tau have been plotted in Fig. 2.14 and Fig. 2.15. Each color indicates a region, blue 4.0 - 7.0 μm , pail green 7.0 - 10.0 μm and green 10.0 - 13.0 μm . The separate panels present the residual spectrum from comparing TU Tau with, respectively, W Ori, S Sct and VX And. The residual spectra in Fig. 2.14 have been determined using *method 1* and those in Fig. 2.15 using *method 2*. Table 2.8, at the end of this section, presents the line positions, line ranges, fluxes at the line positions, total fluxes, equivalent widths, FWHM and the noise at the line positions for the residual UIR band profiles from these spectra. Next are the wings, flanks and the uncertainties introduced by the method for each of the residual UIR band profiles and used methods characterized.

The residual UIR band profiles of TU Tau, determined with W Ori using *method 1*, show the following characteristics:

- 6.22** Sharp and narrow profile. The profile reaches zero flux in the left tail, the right tail has an offset.
- 7.60 + 7.95** Double profile, with two clear peak positions. The wings are not extended. The profile for the combined bands reach zero flux in both tails, but the right tail overshoots.
- 8.60** Sharp, but broad profile. The profile reaches zero flux in both left tails.
- 11.25** Sharp and narrow profile. The profile reaches zero flux in both left tails. Connection with the previous band is good.
- 12.7** No clear profile.

The residual UIR band profiles of TU Tau, determined with S Sct using *method 1*, show the following characteristics:

- 6.22** Sharp, but broad profile. The profile reaches zero flux in the left tail, but overshoots. An offset is present, which could be interpreted as plateau emission.
- 7.60 + 7.95** Double profile, with two clear peak positions. The wings are not extended. The profile for the combined bands doesn’t reach zero flux. An offset is present, which could be interpreted as plateau emission. The right wing has an extra offset, a shift of ~ 2 Jy is probable.
- 8.60** No clear profile.

11.25 Sharp and narrow profile. The profile reaches zero flux in both left tails, but right tail overshoots. Connection with the previous band is good.

12.7 No clear profile.

The residual uir band profiles of TU Tau, determined with VX And using *method 1*, show the following characteristics:

6.22 Sharp and narrow profile. The profile overshoots zero flux in both tails. An offset is present, a shift of ~ 3 Jy is probable.

7.60 + 7.95 Only the $7.95 \mu\text{m}$ part is present. It has a broad peak. The profile reaches zero flux in both tails, but the right tail overshoots.

8.60 Broad profile. An offset is present, a shift of ~ 7 Jy is probable.

11.25 Sharp and narrow profile. The profile reaches zero flux in both left tails, but right tail overshoots. Connection with the previous band is poor.

12.7 No clear profile.

The distance scaling parameter d and the optical depth correction factor t are the governing parameters in *method 1*. The peak positions for the uir band profiles do not change much upon variations in d and t . For as the $6.22 \mu\text{m}$ feature is concerned, residual emission is found when comparing the spectrum from TU Tau with each of the other three stars spectrum. Although, there is for the comparisons with S Sct and VX And a continuum mismatch. This continuum mismatch is also seen for the $7.60 + 7.95$ and $8.60 \mu\text{m}$ profiles. The $11.25 \mu\text{m}$ profile is the best defined from the comparison with W Ori, for the other two comparisons the resulting profiles are embedded in noise. A $12.7 \mu\text{m}$ uir band profile hasn't been found for all three residual spectra. Again, it is due to the additive nature of errors, that it is very difficult here to give a quantitative measure for the 'true' statistical errors in the profiles.

The residual uir band profiles of TU Tau, determined with W Ori using *method 2*, show the following characteristics:

6.22 Sharp and narrow profile. The profile falls back to zero flux in both tails. An offset is present in the right tail. A shift of ~ 1 Jy is probable.

7.60 + 7.95 Double profile, with two clear peak positions. The wings are not extended. The profile for the combined bands reaches zero in both tails, but the left tail overshoots.

8.60 Sharp, but broad profile. The profile reaches zero in both tails. Connection with the next band is reasonable.

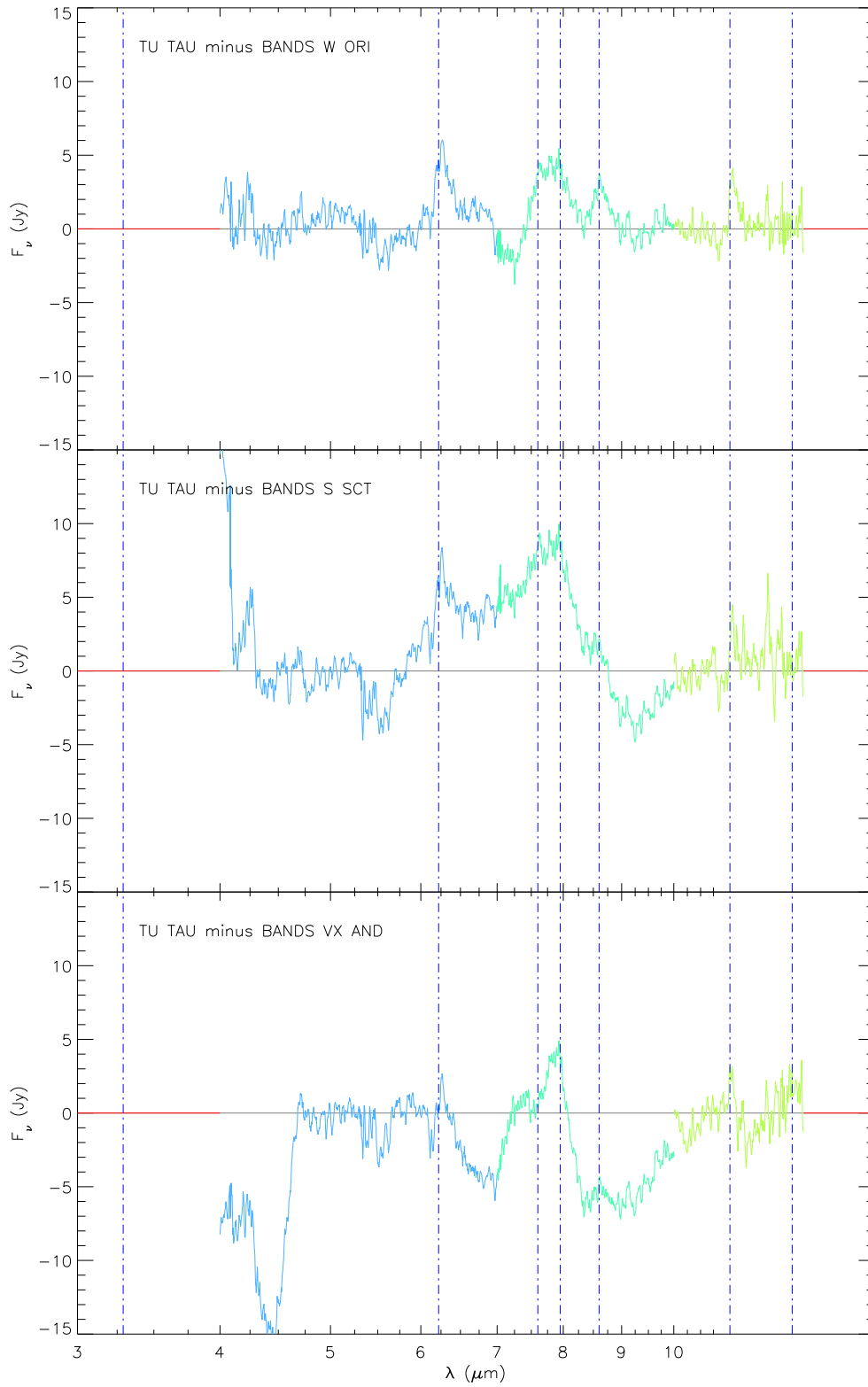


Figure 2.14— Residual spectra for comparing TU Tau with W Ori (top), S Sct (middle) and VX And (bottom), using *method 1*.

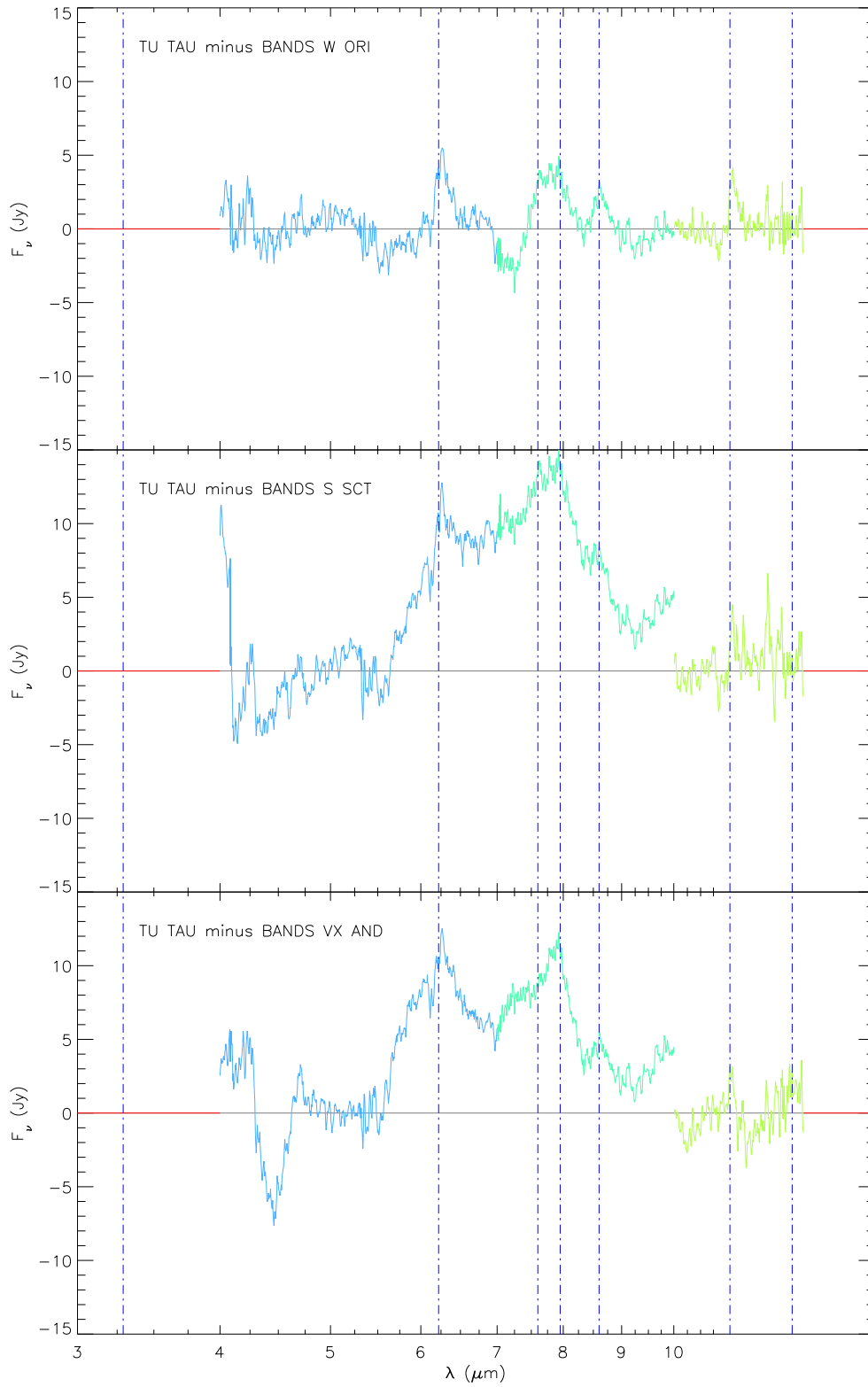


Figure 2.15— Residual spectra for comparing TU Tau with W Ori (top), S Sct (middle) and VX And (bottom), using *method 2*.

The residual uIR band profiles of TU Tau, determined with S Sct using *method 2*, show the following characteristics:

- 6.22** Sharp, but broad profile. The profile falls back to zero flux in the left tail. An offset is present, which could be interpreted as plateau emission.
- 7.60 + 7.95** Double profile, with two clear peak positions. The profile for the combined bands doesn't reach zero flux. An offset is present which could be interpret as plateau emission.
- 8.60** No clear profile. The connection with the next band is very poor.

The residual uIR band profiles of TU Tau, determined with VX And using *method 2*, show the following characteristics:

- 6.22** Sharp, but broad profile. The profile reaches zero flux in the left tail. An offset is present, which could be interpreted as plateau emission.
- 7.60 + 7.95** Double profile, the peaks for the two profiles are not distinguishable. The profile for the combined bands doesn't reach zero flux. An offset is present which could be interpret as plateau emission.
- 8.60** Sharp, but broad profile. The profile doesn't reach zero flux. An offset is present, which could be interpreted as plateau emission. The connection with the next band is very poor.

Besides the optical depth parameter t are here the continuum parameters c_\star and γ_\star , respectively the power-law constant and power-law index of importance to. Any variation in these parameters would worsen the fit of the continuum. It is actually the fit to the $5.0 \mu\text{m}$ absorption feature that worsens the overall match between TU Tau and the comparison star. When the continuum corrections give a relatively good overall match, the optical depth corrections worsens it again. This is however easily understood. As the color classification maps from section 2.1 already showed, no clear relation exists between the molecular bands in carbon-rich AGB stars. This means, when matching only the $5.0 \mu\text{m}$ band the other molecular bands will undergo an independent change. Near $6.2 \mu\text{m}$ we might hope that the effects are negligible, but between $7.0 - 10.0 \mu\text{m}$ it will certainly be not.

Comparing TU Tau with W Ori using *method 1* or *method 2* give remarkably similar profiles. This is a clear indication that TU Tau and W Ori are very alike, as also can be seen from Table 2.6 where only small relative corrections are presented for W Ori and the linear correlation coefficients are very high.

2.6 The profiles

Three techniques have been used to determine the residual spectra of TU Tau. A total of eight residual spectra from $4 - 13 \mu\text{m}$ were obtained this way. Most of these spectra showed excess emission in the uIR bands. This is a very strong indication for the reality of uIR band emission in TU Tau. However, the shape of the profiles vary and are, therefor, less certain.

The three techniques used to determine the residual uIR band profiles, differ in their complexity. The most complex was the third technique, where the distance, continuum and optical depth were matched. (section 2.4, *method 2*). One star, W Ori, showed the most resemblance with TU Tau. The linear correlation coefficients for d , t , c and γ , being nearly one, as the similarity between the values for t , c and γ reflect this. It is, therefor, the profiles deduced from comparing TU Tau with W Ori that has been elected as the main result from this chapter. The profiles found from

the comparison with S Sct and VX And are used to estimate the uncertainties in the main profiles. Fig. 2.16 presents the normalized 6.22, 7.6 + 7.95, 8.6 and 11.2 μm profiles. The uncertainties are indicated with the dashed and dotted lines.

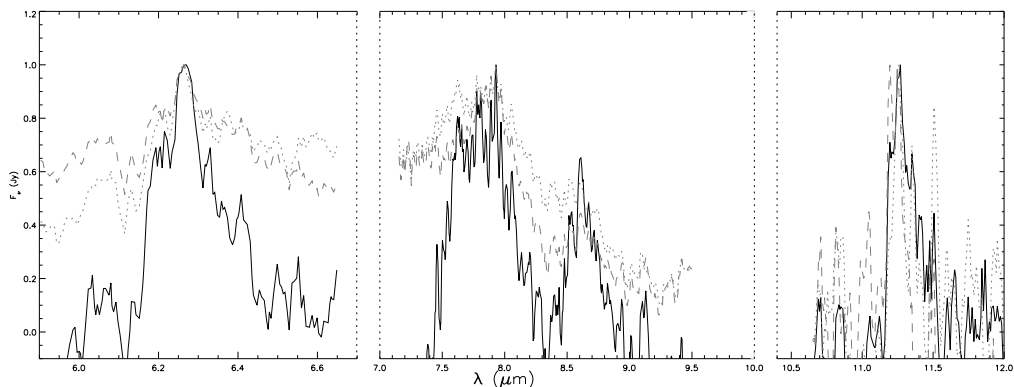


Figure 2.16— Main result: 6.22, 7.6 + 7.95, 8.6 and 11.2 μm profiles. The maxima have been normalized to one.

The profiles representing the estimated errors show, what seems, an underlying plateau of emission. At the end of section 2.5.2, it has been argued that this is actually not plateau emission, but emission which came forth from the counteracting effects of matching both continuum and optical depth. Only very locally corrections can be applied. The result is presented in Fig. 2.17. The profiles are remarkably similar. However, using this ‘extra’ correction is somewhat arbitrary and less systematic than the techniques used to derive the original profiles. Effectively one could just draw ‘super’ local continua in the spectrum of TU Tau and obtain, more or less the same profiles.

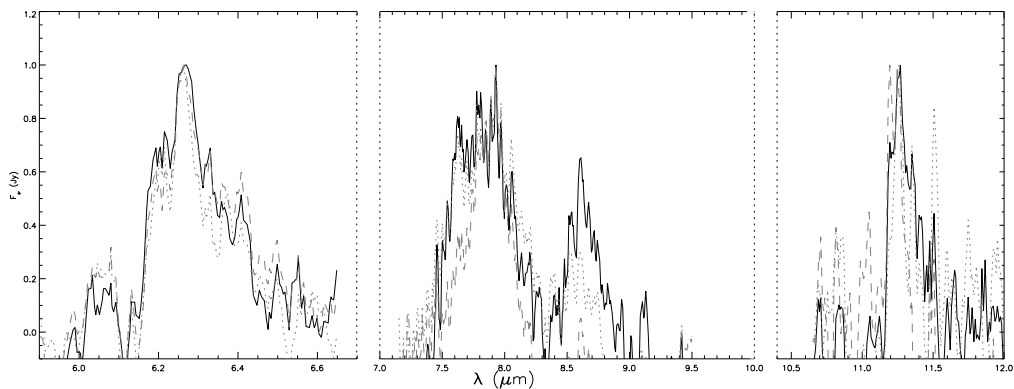


Figure 2.17— Main result with an ‘extra’ continuum component subtracted: 6.22, 7.7 + 8.6 and 11.2 μm profiles. The maxima have been normalized to one.

One could state that it was already clear from Fig. 2.10 and Fig. 2.11 that a mismatch, because

of the poor relation between the optical depths of TU Tau and S Sct/VX And, was imminent. Compare this with the relation for the optical depths between TU Tau and W Ori, here there is much less scatter around the fitted line and therefore the deduced profiles leave much less room for justified corrections. Thus, using the applied 'extra' corrections can be argued for, but keep in mind that the method used to derive them allows for some ambiguity.

The next chapter deals with the comparison of the residual UIR band profiles from TU Tau with those from other types of objects e.g. post AGB stars and PNe. Also the possible relation with PAH molecules is investigated.

	W Ori						MEAN											
Feature (μm)	<u>6.22</u>	<u>7.60</u>	<u>7.95</u>	<u>8.60</u>	<u>11.25</u>	<u>12.7</u>	<u>6.22</u>	<u>7.60</u>	<u>7.95</u>	<u>8.60</u>	<u>11.25</u>	<u>12.7</u>						
λ_0 (μm)	6.270	7.623	7.930	8.610	11.27	-	6.263	7.636	7.930	8.610	11.25	-						
R_a (μm)	6.155	7.421		8.353	11.22	-	6.103	6.956		8.454	10.95	-						
R_b (μm)	6.439		8.353	8.972	11.31	-	6.548		8.349	8.798	11.49	-						
$F_\nu(\lambda_0)$ (Jy)	4.758	4.785	5.651	4.190	1.520	-	6.566	8.224	6.929	2.833	6.485	-						
F (Jy- μm)	0.701			1.264	0.064	-	1.423			0.526	1.947	-						
$\Delta\lambda_1$ (μm)	0.147			0.302	0.042	-	0.217			0.186	0.300	-						
$\Delta\lambda_2$ (μm)	0.150			0.310	0.050	-	0.200			0.180	0.170	-						
σ_{λ_0}	1.08	1.06	1.03	0.81	0.98	1.23	3.33	2.89	2.88	2.58	3.04	3.17						
<i>method 1</i>	BAND (W Ori)						BAND (S Sct)				BAND (VX And)							
Feature (μm)	<u>6.22</u>	<u>7.60</u>	<u>7.95</u>	<u>8.60</u>	<u>11.25</u>	<u>12.7</u>	<u>6.22</u>	<u>7.60</u>	<u>7.95</u>	<u>8.60</u>	<u>11.25</u>	<u>12.7</u>	<u>6.22</u>	<u>7.60</u>	<u>7.95</u>	<u>8.60</u>	<u>11.25</u>	<u>12.7</u>
λ_0 (μm)	6.270	7.623	7.930	8.610	11.27	-	6.263	-	7.930	-	11.25	12.64	6.263	7.623	7.930	-	11.26	-
R_a (μm)	6.103	7.421		8.353	11.16	-	6.201	-	7.554	-	11.11	12.56	6.103	7.000		-	11.16	-
R_b (μm)	6.448		8.319	8.897	11.55	-	6.312	-	8.068	-	11.35	12.91	6.349		8.444	-	11.45	-
$F_\nu(\lambda_0)$ (Jy)	6.012	4.493	5.459	3.725	4.167	-	2.684	-	4.931	-	3.165	3.311	8.322	9.325	9.926	-	4.516	-
F (Jy- μm)	1.107			0.933	0.774	-	0.126	-	1.180	-	0.377	0.589	1.176			-	0.532	-
$\Delta\lambda_1$ (μm)	0.184			0.251	0.186	-	0.470	-	0.239	-	0.119	0.178	0.141			-	0.118	-
$\Delta\lambda_2$ (μm)	0.190			0.270	0.200	-	0.040	-	0.250	-	0.110	0.050	0.190			-	0.180	-
σ_{λ_0}	1.08	1.06	1.03	0.81	0.98	1.23	0.85	0.71	0.67	0.60	0.83	1.01	0.68	0.60	0.60	0.51	0.72	0.94
<i>method 2</i>	BAND (W Ori)				BAND (S Sct)				BAND (VX And)									
Feature (μm)	<u>6.22</u>	<u>7.60</u>	<u>7.95</u>	<u>8.60</u>			<u>6.22</u>	<u>7.60</u>	<u>7.95</u>	<u>8.60</u>			<u>6.22</u>	<u>7.60</u>	<u>7.95</u>	<u>8.60</u>		
λ_0 (μm)	6.270	7.775	7.930	8.610			6.263	7.623	7.930	8.514			6.263	7.622	7.935	8.514		
R_a (μm)	6.143	7.435		8.353														
R_b (μm)	6.479		8.234	8.873														
$F_\nu(\lambda_0)$ (Jy)	5.485	4.455	4.937	3.215			12.78	14.295	15.158	8.669			12.78	14.29	15.16	8.67		
F (Jy- μm)	0.948	→	2.053	0.663														
$\Delta\lambda_1$ (μm)	0.173			0.206														
$\Delta\lambda_2$ (μm)	0.160			0.200														
σ_{λ_0}	1.08	1.06	1.03	0.81			0.85	0.71	0.67	0.60			0.68	0.60	0.60	0.51		

Table 2.8— Residual UIR band profile characterizations for TU Tau. The star names indicate the spectrum used to match TU Tau. *method 1* and *method 2* refer to the two approaches used for determining the residual emission between 4.0 - 10.0 μm . See section 2.5 for details.

Chapter 3

Comparing the UIR bands

In this chapter the UIR band profiles from TU Tau, derived in chapter 2, are compared to those from HII regions, YSO's, RNE, evolved stars and PNE. First the shape and peak positions are investigated to see if there are similarities. Second are the UIR band strength ratios determined and compared to known flux ratio object type correlations. The possible relation with PAH molecules will be addressed at the end of this chapter.

3.1 Profiles

The comparison of shape and peak positions of the profiles is separated into two parts. Part one deals with the features that can be assigned to aromatic C-C bending and stretching modes. These modes leave their fingerprints between 6 - 9 μm . Part two deals with the features that can be assigned to aromatic C-H bending and stretching modes (see section 1.4.2). These modes leave their fingerprints around 3.3 and 11.2 μm .

Fig. 3.1 presents the profiles. The top panel displays the compiled work from Peeters et al. (2002) and Peeters et al. (2003). Each color represents a different class of objects. The bottom panel displays the profiles from TU Tau obtained with the three comparison stars (chapter 2).

3.1.1 C-C modes

Peeters et al. (2002) present, and classify, 6 - 9 μm spectra from RNE, HII regions, YSO's, evolved stars and galaxies that show strong UIR bands. They find that the variations in the UIR bands correlate with object type and each other. Table 3.1 presents their classification scheme. The profiles from TU Tau match the profiles of class \mathcal{B} (compare Table 2.8). In Fig. 3.2 the UIR band profiles from TU Tau have been overlain with the profiles of class \mathcal{B} , their similarities are very clear.

3.1.2 C-H modes

Peeters et al. (2003) present, and classify, spectra around 3.3 and 11.2 μm for a variety of objects. They find correlations between profile peak position, FWHM, object type and the 6 - 9 μm profiles. Table 3.2 presents their classification scheme. The 11.2 μm profile from TU Tau matches class $B_{11.2}$ (compare Table 2.8). Unfortunately only classes $A_{3.3}$, $A_{11.2}$ and \mathcal{A} correlate, it is not possible to use this correlation to constrain a 3.3 μm band. In Fig. 3.2 the 11.2 μm UIR band profile from TU Tau has been overlain with the profile of class $B_{11.2}$, the match is consistent in peak position.

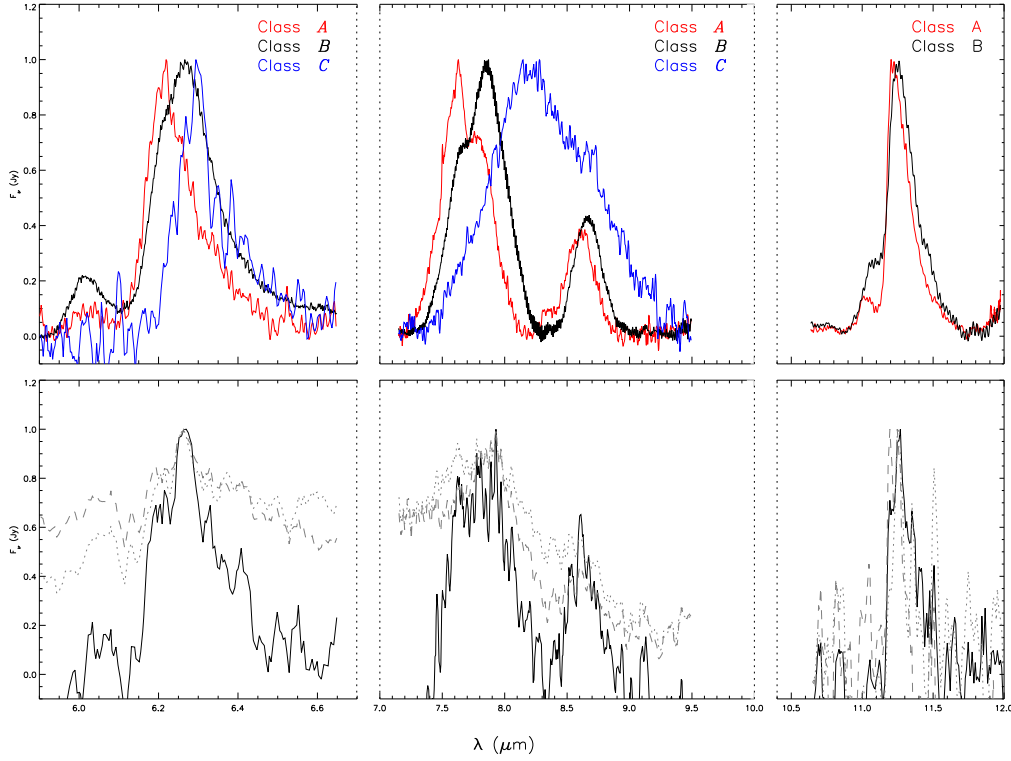


Figure 3.1— Top: the profiles from Peeters et al. (2002) and Peeters et al. (2003). The colors represent for the C-C modes: red = \mathcal{A} , black = \mathcal{B} and blue = \mathcal{C} and for the C-H modes: red = A , black = B . Bottom: the UIR band profiles for TU Tau and their uncertainties.

<u>Class</u>	<u>λ_0 (μm)</u>			<u>Object(s)</u>
	6.2	7.7	8.6	
\mathcal{A}	~ 6.22	~ 7.6 / equal	~ 8.6	HII, RNE
\mathcal{B}	6.24 - 6.28	“7.8”	> 8.62	PNE
\mathcal{C}	~ 6.3	8.22	none	post AGB stars
	6.27	7.6 / 7.8	8.61	TU Tau

Table 3.1— Classification scheme for the 6.22, 7.7 complex and 8.6 μm profiles, λ_0 indicates the peak position. The 7.7 μm complex is classified by its dominant component. Adapted from Peeters et al. (2002).

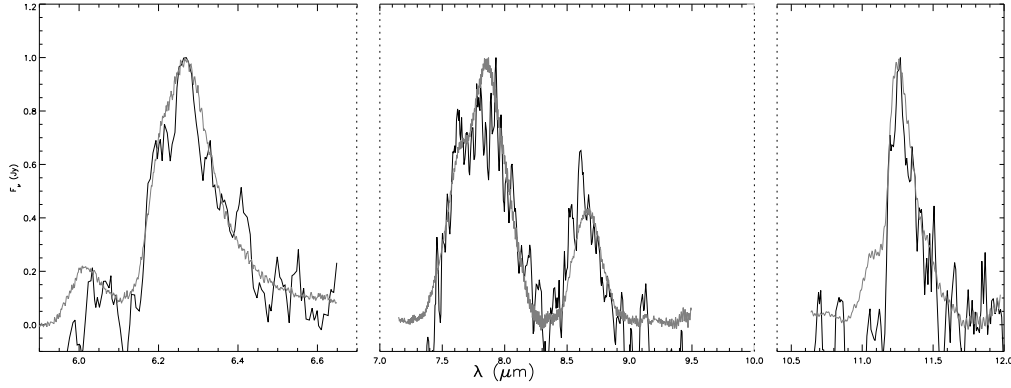


Figure 3.2— The matching UIR band profiles (class \mathcal{B} and $B_{11.2}$) have been overlaid on the UIR band profiles from TU Tau.

<u>Class</u>	<u>λ_0 (μm)</u>	<u>$\Delta\lambda_2$ (μm)</u>	<u>Object(s)</u>
A _{3.3}	~ 3.290	~ 0.040	HII, Herbig, YSO's, Galaxies, PNE
B _{13.3}	~ 3.293	~ 0.037	post AGB
B _{23.3}	~ 3.297	~ 0.037	post AGB
A _{11.2}	$\sim 11.20 - 11.24$	~ 0.17	HII, Herbig, YSOs
A(B) _{11.2}	$\sim 11.20 - 11.24$	~ 0.21	Galaxies, PNE
B _{11.2}	~ 11.25	~ 0.20	Galaxies, PNE, post AGB
	11.25 - 11.27	0.05 - 0.2	TU Tau

Table 3.2— Classification scheme for the 3.3 μm and 11.2 μm profiles. Adopted from Peeters et al. (2003).

The profile object type correlation with the C-H mode profiles is not as tight as with the C-C mode profiles. Also, the determined FWHM for the profiles from TU Tau have a large intrinsic uncertainty due to the method applied for deriving them. However, combining the object identifications from both modes and putting little weight on the FWHM, indicates that the UIR bands from TU Tau show a lot of similarities with those from PNE.

3.2 Flux ratios and ionization

Hony et al. (2000) present spectra from HII, YSO's, PNE and PNE. They find that object type correlates with certain UIR band flux ratios. These correlations are found for $\frac{I_{3.3}}{I_{6.2}}$ with $\frac{I_{11.2}}{I_{6.2}}$, $\frac{I_{6.2}}{I_{11.2}}$ with $\frac{I_{12.7}}{I_{11.2}}$ and $\frac{I_{\text{PAH}}}{I_{\text{IR}}}$ with $\frac{I_{12.7}}{I_{11.2}}$. For TU Tau only $F_{6.2}$ and $F_{11.2}$ are reliable, so the full potential of the

correlations can not be used. However, they might give insightful constraints on $F_{3.3}$ and $F_{12.7}$.

<u>profile</u>	6.2	11.2
6.2	1	0.59
11.2	1.68	1

Table 3.3— Flux ratios for the uir bands of TU Tau.

<u>profile</u>	<u>a</u> (μm)	<u>b</u> (μm)
6.2	6.1	6.6
11.2	10.8	11.9

Table 3.4— Integration ranges used for the determination for the flux ratios in the uir bands of TU Tau.

Table 3.3 presents the determined flux ratios for TU Tau. The ratios have been calculated using the integration ranges given in Table 3.4 ($F_x = \int_a^b F_v(\lambda)d\lambda$).

The left panel of Fig. 3.3 displays the established correlation for $\frac{F_{3.3}}{F_{6.2}}$ with $\frac{F_{11.2}}{F_{6.2}}$. The gray line indicates the derived range for TU Tau, when assuming the established correlation and a range in $\frac{F_{11.2}}{F_{6.2}}$ similar to the spread in the correlation. The match of the TU Tau with a single object is very ambiguous. The possible positions imply that the band strengths of TU Tau show characteristics common to several objects.

The right panel of Fig. 3.3 displays the established correlation for $\frac{F_{6.2}}{F_{11.2}}$ with $\frac{F_{12.7}}{F_{11.2}}$. The gray line indicates the possible positions for TU Tau, when assuming the range in $\frac{F_{12.7}}{F_{11.2}}$ to be similar to the spread in the correlation. Here the match of the TU Tau with a single object is also very ambiguous. Again, the possible positions imply that the band strengths of TU Tau show characteristics common to several objects.

However, keep in mind that the objects on which the correlation is based are bright objects that show strong uir bands. In contrast to TU Tau, which is not a bright object and has weak uir bands. This leaves some room for debate on the exact location of TU Tau on these correlation diagrams.

When adopting the established relationship between the $\frac{F_{11.2}}{F_{6.2}}$, $\frac{F_{3.3}}{F_{6.2}}$ and the $\frac{F_{12.7}}{F_{11.2}}$ ratios it is possible to predict $F_{3.3}$ and $F_{12.7}$.

$F_{3.3}$ can be found from the correlation of $\frac{F_{3.3}}{F_{6.2}}$ with $\frac{F_{11.2}}{F_{6.2}}$. $F_{3.3}$ is then estimated as $F_{3.3} = F_{6.2} \cdot 10^\chi = 1.02 \cdot 10^\chi$ (Jy $\cdot\mu\text{m}$), with $-0.85 \lesssim \chi \lesssim -0.65$. Putting in the values for χ gives

$0.14 \lesssim F_{3.3} \lesssim 0.23$ ($\text{Jy}\cdot\mu\text{m}$).

$F_{12.7}$ can be found from the correlation of $\frac{F_{6.2}}{F_{11.2}}$ with $\frac{F_{12.7}}{F_{11.2}}$. $F_{12.7}$ is then estimated as $F_{12.7} = F_{11.2} \cdot 10^\chi = 0.61 \cdot 10^\chi$ ($\text{Jy}\cdot\mu\text{m}$), with $-0.25 \lesssim \chi \lesssim 0.0$. Putting in the values for χ gives $0.34 \lesssim F_{12.7} \lesssim 0.61$ ($\text{Jy}\cdot\mu\text{m}$).

This shows, when assuming a Gaussian profile with a width of $\sim 0.1 \mu\text{m}$ for $F_{3.3}$ and $\sim 0.4 \mu\text{m}$ for $F_{12.7}$, that it would have been difficult to detect these features in the spectrum of TU Tau, if they are present. When looking back at Fig. 2.14 and Fig. 2.15 it is clear that such features at these wavelengths could be missed.

No definite match with one type of object can be made for TU Tau, based upon the correlations between the UIR band strength ratios. Also, the band strength ratios in TU Tau do not at all seem to correspond to those in PNE. But, nevertheless, some insightful constraints for $F_{3.3}$ and $F_{12.7}$ were obtained.

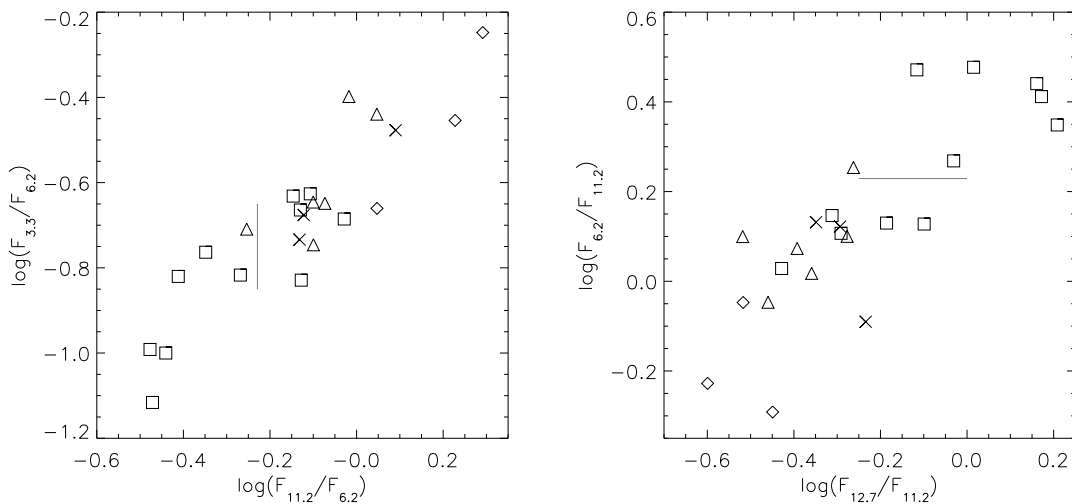


Figure 3.3— Band strength ratios. Squares indicate HII regions, triangles indicate intermediate mass star forming regions, crosses indicate RNE and diamonds indicate PNE. The gray lines indicate the possible location of TU Tau. Adapted from Hony et al. (2000).

3.3 Implications

As already has been seen in section 1.4, Polycyclic Aromatic Hydrocarbons (PAHS) are good candidates for the carriers of the UIR bands. Laboratory studies and quantum mechanical calculations have revealed the characteristics of PAHS. But their seems to be a discrepancy between astronomical PAH spectra and those obtained in laboratory. The gap is however closing. Including effects as PAH ionization, structure, symmetry, heterogeneity and dehydrogenation, which induce small shifts in peak positions and intensities, help remove them. Most striking is the influence of PAH ionization, especially between 5 - 10 μm . The peak positions of the profiles is hardly effected, but the intensity changes remarkably. The emission in this region is coming from aromatic C-C stretching modes. A strong oscillating dipole in the C-skeleton is created when the PAH molecule

is ionized, while the oscillating dipole moments for the C-H bonds are reduced. This behavior is seen in all PAHS known to date.

The peak position for the 6.2 μm profile of TU Tau, due to ionized PAHS, is roughly located at $\sim 6.27 \mu\text{m}$. Whereas laboratory studies show that the peak positions for ionized PAHS fall just longward 6.3 μm . Since TU Tau has an insignificant radial velocity ($v = -24 \text{ Km} \cdot \text{s}^{-1}$), thus a negligible Doppler shift. For PAHS consisting up to 30 carbon-atoms, it has been shown that the peak position shifts to shorter wavelengths with increasing molecular size. For PAH molecules with more than 30 carbon-atoms the trend, however, levels off (Hudgins & Allamandola 1999). Unfortunately the relation between PAH size and peak position isn't able to bridge this $\sim 0.05 \mu\text{m}$.

Another property that can shift the peak position is the symmetry of a PAH molecule (Bauschlicher 2002). When the symmetry is broken cancellation of opposite oriented dipoles doesn't occur anymore. However the shift in peak position is very small and the peaks generally still fall beyond 6.3 μm .

Maybe molecular heterogeneity might also solve the problem. Disturbing the heterogeneity alters the symmetry and the charge distribution of the PAH molecule. Effects on the IR spectra are dependent on the substituted atom and the location of the substitution (Bauschlicher 2002). The best candidate for substitution is nitrogen, basically for two reasons; one: incorporation of nitrogen into the PAH doesn't compromise the aromatic stability of the π bond, two: nitrogen is relatively abundant with respect to oxygen (locked in CO) and silicate (locked in SiC). However, alterations to the heterogeneity of a PAH molecule generally shift the peak position back to 6.2 μm .

Concluding, the most likely carrier of the 6.27 μm band in TU Tau is thus, a family of small, 'pure' carbon, ionized PAHS.

The 7.7 μm complex is produced by aromatic C-C stretching and C-H in-plane bending modes. Laboratory studies show that single ionized PAHS give at least one strong feature between 7.2 and 8.2 μm . The peak position for the 7.6 μm component is readily reproduced in these spectra. However the origin of the dominant 7.8 μm component in TU Tau is an enigma. It is not well reproduced in laboratory spectra and a trend, as for the 6.2 μm profile, linking PAH size to peak position isn't found for the 7.7 μm complex. Dehydrogenation has almost no influence on peak position and this time incorporation of nitrogen also doesn't produce the desired shift. Most likely other PAH related species play an important role here.

Concluding, the most likely carrier of the 7.6 μm component in TU Tau is a family of either pure-C or N substituted PAHS. The dominant 7.8 μm component in TU Tau is most likely carried by other PAH related species.

The peak position for the 8.6 μm profile from TU Tau lies at $\sim 8.61 \mu\text{m}$. Laboratory studies show that the profile and peak position are readily reproduced by neutral PAHS. Responsible are combination modes of aromatic C-C and C-H modes vibrations.

Aromatic C-H stretching and aromatic C-H out-of-plane bending modes produce the 11.2 μm profile. Especially the solo aromatic C-H modes of neutral PAHS have been shown to fit the observed stellar positions well.

Overall a diverse family of PAHS is present in the CSE of TU Tau. The family consists of both 'pure' C and N substituted PAHS. The clear absence of the 3.3 and 12.7 μm features suggests that the PAHS are mostly ionized. Also some neutral PAHS and PAH related species belong to the family.

Based on the comparison of TU Tau's band profiles one would conclude that TU Tau has the

most resemblance with PNE, however, the observed band strength ratios for TU Tau are more similar to those observed for the ISM.

The next chapter deals with the impact on the PAH evolution scheme that the detection of PAHS in the CSE of TU Tau has. Also the ambiguity in the identification of TU Tau with a single object and the possible influence of TU Tau's hot companion on the PAHS are addressed.

Chapter 4

Impacts

In chapter 3 it became clear that the U_{IR} bands from TU Tau show the most resemblances with those from PNE. This result enables us to draw some conclusions on the PAH evolution scheme. But what should be kept in mind is that these conclusions are drawn upon the results found for a single carbon-rich AGB star and perhaps even more important, the physical environment around this star might differ from more ‘common’ carbon-rich AGB stars due to the presence of a hot companion.

4.1 PAH evolution

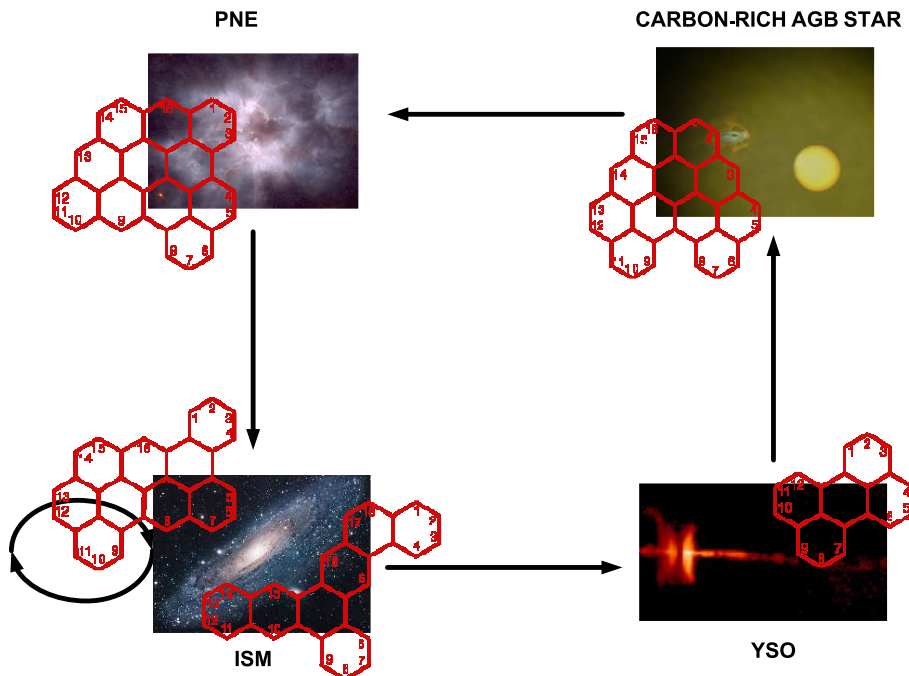


Figure 4.1— Schematic evolution scheme for PAHs. In each phase the PAH family can be altered due to the differences in physical environment.

In Fig. 4.1 the proposed evolution path for PAHs is schematically drawn. Dust and PAHs are introduced into the ISM mainly by dust-driven winds from carbon-rich AGB stars (top right). The smaller PAHs are more sensitive to the harsh environment of interstellar space than the dust and are therefore more likely to have undergone changes when reaching finally the ISM. It has already been shown that in the final evolutionary step, the transition from PNE PAHs into ISM PAHs, the PAH family changes (Hony et al. 2000 and Peeters et al. 2002). The question that remained was if PAHs undergo any changes in the first evolutionary step from CSE, of carbon-rich AGB star, PAHs into PNE PAHs. The nature of the changes PAHs undergo is still very uncertain, is the old family destroyed

and a new one created, or do the PAHS form clusters, with different characteristics, in each phase. One of the key questions is, whether the differences in the PAH family compositions is governed by a single parameter (e.g. clustering), or that it is the complex cooperation of several physical parameters. Since no data is yet available on PAH clusters and clustering, the need for laboratory studies is essential and should soon be put on the agenda of the relevant scientific research groups.

The spectral variations in peak position in the 5 - 9 μm region of TU Tau are thought to reflect a chemical evolution of the carrier; eg. incorporation of N in the ring. Given that AGB stars (TU Tau) and PNE have similar spectral characteristics, but different from interstellar objects, suggests that the changes predominantly happen in the ISM (top left).

PAH processing and reprocessing in the ISM occurs through several high energy and low energy processes. These processes include FUV processing, shock processing and ice processing (Strazulla et al. 1995 and Bernstein et al. 1999). The high energy processing are responsible for the more open structured nature of ISM PAHS. The focus is now on PAH destruction.

In all cases considered it will be the weaker bond of the atoms/groups attached to the C-skeleton that will dissociate, with the weakest bounded, first. The bond energies of these peripheral atoms on PAHS typically lie between 4-6 eV (Omont 1986). When photons are involved two things can happen; one, the PAH molecule is heated to such a high temperature that the peripheral atoms evaporate and two, a direct excitation of the σ -bond leads to the dissociation of peripheral atoms. It has been shown that evaporation is negligible for PAHS with $\bar{N}_C \gtrsim 25$ and also that direct dissociation is very unlikely for large molecular systems that have a high density of electronic states (Omont 1986).

Grains are also capable of destroying PAHS. Grains in the ISM can acquire a relatively high velocity with respect to the gas through turbulence (Voelk et al. 1980 and Draine & Anderson 1985), rocket thrust by the photoelectric effect (Purcell 1979), etc. Moreover, charged grains can acquire very large velocities due to magnetic shocks (Draine 1980). The stronger coupling to the gas, because of their small mass, makes it difficult for PAHS to maintain their large velocities. Therefore destruction of PAHS in the ISM will be through grain-PAH collisions and not through PAH-PAH collisions. When a grain collides with a PAH its effect on the grain is negligible, but the severe deformation of the PAH can result in the breaking of C-C bonds and the ejection of C-atoms into the gas. Chemical reaction involving PAHS can also destroy PAHS. This is called chemical sputtering.

However PAHS are not only destroyed in the ISM, they can also grow and may even form from grains that have been shattered in shocks. Recent laboratory studies have shown that PAHS are also formed in cosmic ices upon energetic processing (Gudipati & Allamandola 2003), these results suggest that ice-processing can be very important in the ISM.

Summarizing, the family of PAHS present in the ISM consists of modified PNE PAHS, which are being destroyed, modified and which grow. Also part of this family are newly formed PAHS from the remnants of shattered grains.

In the never ending dust cycle the ISM PAHS will eventually become part again of star forming regions. When a newly formed star ignites fusion the harsh environment that it creates will destroy most of the PAHS again (bottom right). When, at the end of stellar evolution, in the CSE of newly formed carbon-rich AGB stars PAHS are formed again the evolution scheme has come to full circle.

4.2 Influence of companion star on the PAH composition in TU Tau

The effect of FUV photons on PAHS has become clear from the previous section. TU Tau has, in contrast to more ‘common’ carbon-rich AGB stars, a hot companion star. This companion star gives rise to FUV photons, which are normally not present near carbon-rich AGB stars. The influence of these photons on the PAH family composition in the CSE of TU Tau has to be investigated to exclude the possibility that the composition is mainly determined by the presence of the companion. In other words, that the PAH family composition near TU Tau is similar to that near more ‘common’ carbon-rich AGB stars.

The influence of the FUV photons on PAHS can be twofold. First there is the possible influence on the ionization state of the PAHS. Secondly the influence on the amount of PAHS present. To determine the order of these influences, some estimates for the circumstances at the shell where PAHS are formed have to be made.

For the FUV field an estimate can be made when knowing that the companion is an A2 IV star. Zombeck (1990) give an absolute V-band magnitude M_V of 0.53 and the effective temperature for an A2 IV star is ~ 9700 K. To calculate the absolute bolometric magnitude a bolometric correction (BC) has to be applied, according to eq. (4.1). However Flower (1996) give a BC ~ 0.0 .

$$M_{\text{bol}} = M_V + \text{BC} \quad (4.1)$$

Using eq. (4.2) gives for the absolute bolometric luminosity $L = 10^{\frac{4.83-0.53}{2.5}} = 52 L_{\odot}$

$$M_{V(\odot)} - M_V = 2.5 \log \left(\frac{L}{L_{\odot}} \right) = M_{V(\odot)} - M_{\text{bol}} \quad (4.2)$$

For a separation of 152 AU (see section 1.6), and using $1 L_{\odot} = 3.826 \cdot 10^{33} \text{ erg} \cdot \text{s}^{-1}$ and $1 \text{ AU} = 1.50 \cdot 10^{13} \text{ cm}$, the bolometric flux F_{bol} is given according to eq. (4.3).

$$F_{\text{bol}} \approx \frac{52 \times 3.826 \cdot 10^{33}}{4\pi(152 \times 1.5 \cdot 10^{13})^2} = 3.0 \cdot 10^3 \text{ erg} \cdot \text{cm}^{-2} \cdot \text{s}^{-1} \quad (4.3)$$

The amount of energy radiated away in the FUV is determined by taking into account a correction factor f_{FUV} . This dilution factor is approximated with eq. (4.4).

$$f_{\text{FUV}} = \int_{3.1 \text{ eV}}^{13.6 \text{ eV}} B_{\nu}(\nu, T) d\nu / \sigma T^4 \quad (4.4)$$

When taking a blackbody temperature of $T = 9700$ K the dilution factor becomes $f_{\text{FUV}} = 0.46$. The energy emitted in the FUV is then, in Habing units, $G_0 = 0.46 \times 3.0 \cdot 10^3 / 1.6 \cdot 10^{-3} = 0.9 \cdot 10^6$.

In comparison, this strength of the incident FUV field is similar to that of PNE such as NGC 7027 and much larger than that for RNE such as NGC 2023 and NGC 7023 (Hony et al. 2000).

The electron density n_e is found considering the ionization balance, eq. (4.5) for a specific specie, e.g. Fe. Here n_n is the number of neutrals, k_{ion} is the ionization rate coefficient, n_{ions} is the number of ionized particles and α is the recombination rate coefficient.

$$n_n \cdot k_{\text{ion}} = n_{\text{ions}} \cdot n_e \cdot \alpha \quad (4.5)$$

When considering only single ionizations the charge balance reads eq. (4.6).

$$n_{\text{ions}} = n_e \quad (4.6)$$

Similarly, for the particle density eq. (4.7) can be written.

$$n = n_{\text{ions}} + n_{\text{n}} \quad (4.7)$$

k_{ion} depends on the radiation field present and can be written as (4.8), where k_0 is the unattenuated rate and γ is an attenuation constant.

$$k_{\text{ion}} \simeq G_0 \cdot k_0 \cdot e^{-\gamma A_V} \quad (4.8)$$

The degree of ionization x is defined through eq. (4.9).

$$x \equiv \frac{n_{\text{ions}}}{n_{\text{ions}} + n_{\text{n}}} \quad (4.9)$$

With the degree of ionization, the ionization balance can be written as eq. (4.10).

$$\frac{1-x}{x^2} = \frac{n \cdot \alpha}{k_{\text{ion}}} \quad (4.10)$$

What is now left is to find appropriate values for the density, recombination rate and ionization rate coefficients.

Lets use iron (FeI) to probe the electron density. Spaans et al. (1994) give for FeI irradiated by a blackbody with temperature $T_{\text{eff}} = 10^4$ K, $k_0 = 2.24 \cdot 10^{-11} \text{ s}^{-1}$ and $\gamma = 2.14$. For A_V the interstellar extinction is taken as an upper limit, $A_V \simeq 3.1 \cdot E(B-V) = 1.36$. Putting this together with eq. (4.8) gives $k_{\text{ion}} \simeq 1.1 \cdot 10^{-6} \text{ cm}^2$. Nahar et al. (1997) give for Fe^+ around 800 K, the temperature of the CSE (Allain et al. 1997), $\alpha \simeq 4.34 \cdot 10^{-12} \text{ cm}^3 \cdot \text{s}^{-1}$. For the total iron density $n_{\text{FeI}} \sim 3 \cdot 10^1 \text{ cm}^{-3}$ is adopted. This is for a hydrogen density of $n_{\text{H}} \sim 1 \cdot 10^8 \text{ cm}^{-3}$, typical for the near-photospheric regions in the CSE of such carbon-rich AGB stars (Aoki et al. 1998), and an iron abundance of $[\text{FeI}] \sim 3 \cdot 10^{-5}$. Putting this into eq. (4.10) gives $x \approx 1.0$, indicating all the iron is ionized. The electron density is then $n_e \approx 3 \cdot 10^3 \text{ cm}^{-3}$.

The ionization state of a PAH is controlled by the parameter $\frac{G_0}{n_e}$, which in this case gives $\frac{G_0}{n_e} \sim 30 \text{ cm}^3$. For comparison, for typical diffuse clouds $\frac{G_0}{n_e} \sim 500 \text{ cm}^3$, for RNE, associated with HII regions, $\frac{G_0}{n_e} \sim 10^3 \text{ cm}^3$ and for PDRS $\frac{G_0}{n_e} \sim 10^4 \text{ cm}^3$ (Bakes et al. 2001)

Coupling this back to the observed $\frac{F_{11.2}}{F_{6.2}}$ ratio for TU Tau, which possibly reflects the ionization over recombination ratio, it is obvious that similar band strength ratios are seen for objects which have the same $\frac{G_0}{n_e}$ (see Fig. 3.3).

For a PAH that can only be single ionized, the neutral fraction $f(0)$ is given by eq. (4.11). Here γ is the ionization rate coefficient over the recombination rate coefficient.

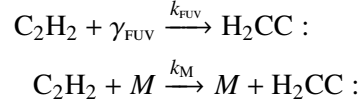
$$f(0) = (1 + \gamma)^{-1} \quad (4.11)$$

When taking the electron recombination rate for phenanthrene, γ is given by eq. (4.12).

$$\gamma = 1.4 \cdot 10^{-5} \cdot N_{\text{C}}^{\frac{1}{2}} \cdot \frac{G_0}{n_e} \cdot T^{\frac{1}{2}} \quad (4.12)$$

Extrapolating for a PAH of 50 C-atoms and $T = 800$ K, gives a small neutral fraction of $f(0) \approx 1.2 \cdot 10^{-4}$. This shows, in accordance with the conclusions from section 3.3, that indeed most of the PAHS are ionized.

The C_2H_2 radical formation is a good first order indicator for the influence of the FUV photons on the PAH formation rate. The formal reactions, considered here, for forming the acetylene radical are given below,



where the radical can be formed through photon interaction or collisional interactions with the molecule M . The reaction rate k_{FUV} can be calculated using eq. (4.13), where A_V is the extinction and γ is a parameter to take into account the increasing extinction at FUV wavelengths.

$$k_{FUV} = \alpha_{FUV} \cdot e^{-\gamma \cdot A_V} \text{ s}^{-1} \quad (4.13)$$

Le Teuff et al. (2000) tabulate, for the interstellar radiation field (ISRF) as photon source, $\alpha_{FUV} = 4.6 \cdot 10^{-10} \text{ s}^{-1}$ and $\gamma = 3.1$. Taking again the interstellar extinction as the upper limit, $A_V \approx 1.36$, gives $k_{FUV} \approx 6.8 \cdot 10^{-12} \text{ s}^{-1}$.

The reaction rate k_M can be calculated using eq. (4.14), where α_M is the rate constant, T the temperature, E the energy term and R the gas constant.

$$k_M = \alpha_M \cdot T^n e^{-\frac{E}{RT}} \text{ cm}^3 \cdot \text{s}^{-1} \quad (4.14)$$

Frenglach & Feigelson (1989) tabulate $\alpha_M = 3.2 \cdot 10^{16} \text{ mol} \cdot \text{cm}^3 \cdot \text{s}^{-1}$, $n = 0$ and $E = 159 \text{ kJ} \cdot \text{mol}^{-1}$. Given $R \equiv 8.31 \cdot 10^{-3} \text{ kJ} \cdot \text{K}^{-1} \cdot \text{mol}^{-1}$, $1 \text{ mol} \equiv 6.022 \cdot 10^{23}$ and taking $T = 800 \text{ K}$, gives $k_M \approx 2.18 \cdot 10^{-18} \text{ cm}^3 \cdot \text{s}^{-1}$

The parameter that summarizes the influence of the FUV field, is χ , given in eq. (4.15),

$$\chi \equiv \frac{[C_2H_2] \cdot f \cdot k_{FUV}}{[C_2H_2][M] \cdot k_M} = \frac{k_{FUV}}{k_M} \cdot \frac{f}{[M]} = 3.1 \times 10^6 \cdot \frac{f}{[M]} \quad (4.15)$$

where f is a correction factor for the ISRF.

Taking $\gamma_{ISRF} = 1 \cdot 10^8 \text{ photons} \cdot \text{cm}^{-2} \cdot \text{s}^{-1}$, a Blackbody at $T = 9700 \text{ K}$, $d = 152 \text{ AU}$ and for a typical stellar radius for a A0 V star $R = 2.5 R_\odot$ will give according to eq. (4.16) $f = 2 \cdot 10^6$.

$$f = \frac{\gamma_{FUV}}{\gamma_{ISRF}} = \gamma_{ISRF}^{-1} \cdot \left(\frac{R}{d}\right)^2 \cdot \int_{3.1 \text{ eV}}^{13.6 \text{ eV}} \frac{B_\nu(\nu, T)}{h\nu} d\nu \quad (4.16)$$

The collisional partner for acetylene is H or H_2 , using again a density of $1 \sim 10^8 \text{ cm}^{-3}$ results in $\chi \sim 6 \cdot 10^4$. Implying that the presence of the FUV photons near TU Tau seem to have a significant effect on the PAH formation rate.

However, the estimates made are very crude. First the density, Cherchneff et al. (1992) show that the density near the dust forming regions in the outflow of giants is around $1 \cdot 10^{11} \text{ cm}^{-3}$. This brings χ down to 60. Second the temperature, the collisional reaction is not efficient because an energy barrier equivalent to 19000 K at 800 K has to be bridged. This gives a Boltzmann factor of $5 \cdot 10^{-11}$. Around 1000 K the Boltzmann factor increases and χ starts to become greater than one, which suggest that when the outflow of gas starts and the gas moves away from the warm stellar surface, the collisional reaction becomes less important.

This shows that it is important that detailed models for the stellar outflow of TU Tau should be made, including FUV processing.

Chapter 5

Summary and conclusions

The gas and dust present in space has a profound influence on the ISM. An important component of interstellar dust, genuine star dust, can be traced back to AGB stars through meteorites. Soot, carbonaceous dust, is formed through the carbon condensation route. PAHs are the building blocks in this route. PAHs on them selfs are, when not incorporated into soot, also injected into the ISM. The presence of these large molecules in space has a big influence on many aspects of the ISM. The presence of PAHs in space is generally accepted, presently however, the specific molecular identifications of the carriers remains elusive. The ultimate goal is the identifications of the individual molecules of the PAH family. For this an understanding of the evolution of PAHs; when, where and how they form, is essential.

The CSE of carbon-rich AGB stars house a wide variety of molecular species. Their fingerprints show up in the spectra of these stars in the form of many absorption and emission lines. With the SWS instrument on board ISO many spectra of carbon-rich AGB stars have been obtained and made it possible to identify many of the species.

Spectral features around 3.3, 6.2, 7.6, 7.9, 8.6, 11.2 and 12.7 μm are usually identified belonging to PAHs. PAH molecules need FUV photons to get excited, therefor the features in the so called UIR bands are commonly not found in spectra of carbon-rich AGB stars. However the sample of 50 warm carbon-rich AGB stars, contains a binary star, TU Tau. The companion of TU Tau is a hot A star that provides FUV photons able to excite the PAHs.

Appropriate stars to TU Tau have been selected from the sample to compare. Corrections for continua and optical depth have been applied. The use of global continua was inadequate and local continua were required. The local continua show that corrections in the optical depth are also necessary. The residual emission in the UIR bands is obtained by subtracting the corrected spectra from the spectrum of TU Tau.

The profiles of the residual emission in the UIR bands of TU Tau have been compared to UIR band profiles from the ISM, post AGB stars and PNE. The profiles of TU Tau are shown to have the most resemblance with those from PNE. Uncertainties in the deduced residual UIR band profiles exist, however a lot of confidence is put in the reality of these profiles.

Determined UIR band flux ratios, laid against UIR band strength correlations known for several types of objects, gave no definite match between TU Tau and a single class of objects. Whereas, to first order, the profile shape is a measure of the molecular structure (chemistry), the UIR band strength ratios are a measure of the ionization state (environment). This suggests that the physical conditions in the CSE of TU Tau differ significantly from PNE conditions, but that the similar molecules are playing a role.

The match of the UIR band profiles of TU Tau with those from PNE indicates that PAHs are formed in the CSE of carbon-rich AGB stars and make it largely unmodified into the PN phase. Which indicates that the differences between PNE and ISM PAHs is mostly due to processing in the ISM phase.

PAH processing in the ISM can occur through several high energy and low energy processes. These processes include FUV processing, shock processing and ice processing.

The influence of the nearby companion star on the PAH ionization state and PAH formation rate was also established. The analysis indicated that the contribution of the companion star to these parameters can be significant, depending on position in the outflow.

5.1 Discussion and future work

The general conclusions have mainly been based on the results from chapter 2, the determination of the UIR band profiles from TU Tau. It is the determination using both the continuum and optical depth corrections where the focus of this discussion lies.

The uncertainties in the profiles have been put in terms of the residual profiles obtained after subtracting a best, a second best and a worst ‘appropriate’ comparison star. The residual profiles from comparing with the three stars show, indeed that residual emission is present, however the nice profiles obtained with the best comparison, star W Ori, are only found for the other two after subtracting an ‘extra’ continuum component.

The optical depth corrections, together with the power-law continuum seemed to work very nice. Especially with W Ori. The corrections were only of first order, but wanting to correct for higher orders would be very difficult and the interpretation would become more difficult. As section 3.3 made clear, due to large variation near 6 - 10 μm between the different spectra, the fit to the optical depth counteracted, in some extend, the fit to the continuum. A better approach would be to model spectra for general carbon-rich AGB stars, get constraints on the different parameters, and then create a model for TU Tau without PAHs. Comparison of TU Tau with the model would give the most reliable UIR band profiles. The modeling of the complex spectra, with the many parameters, should give better insight in the reality of the residual UIR band emission. Moreover many of the difficulties arising from different stellar parameters as $T_{\text{effective}}$, $\log g$, C/O, . . . are then corrected for. Perhaps it would even become possible to constrain the 3.3 and 12.7 μm UIR band presence and profiles.

Detailed modeling of the stellar outflow, including the FUV photons coming from the companion star, should reveal if the UIR band profiles from TU Tau are characteristic for ‘common’ carbon-rich AGB stars.

Finding more good comparison stars such as W Ori will, obviously, improve the statistical significance of the deduced results. The sample presented in this work was obtained with AOR sws01, which is of relatively low resolution. Higher resolution spectra would teach us more about the PAH profiles themselves. At moderate resolution spectra using VISIR on the VLT can help search, from the ground, for the 11.2 μm profile.

Acknowledgments

At the end of all this some words of thanks are in order. First of all to my supervisors Xander and Sacha. Although Sacha has his office in Noordwijk, he often found the time to come to 'Anton Pannekoek' in Amsterdam to give me advise on my progress. Xander spent most of his time abroad, but his brief but subtle comments and remarks, which I received by e-mail, were always very useful and sometimes even necessary.

Other staff-members I would like to thank are Russ Shipman for his help with *OSIA* and Do Kester for his help on the *IRAS* data of TU Tau, which has been shortly investigated for long period changes in the spectrum of TU Tau. Special thanks to Els Peeters for providing me with her data on the *UIR* band profiles for the *PNE*, post *AGB* stars and the *ISM*. Further, I would like to thank Wilfred Frieswijk and Erwin Platen for there help with *IDL*. Also I would like to thank Chris Ormel and Erwin Platen for their remarks and help on a scientific level.

References

- Alksnis, A., Balklavs, A., Dzervitis, U., Eglitis, I., Paupers, O., & Pundure, I. 2001, *Baltic Astronomy*, 10, 1
- Allain, T., Sedlmayr, E., & Leach, S. 1997, *A&A*, 323, 163
- Allamandola, L. J., Tielens, G. G. M., & Barker, J. R. 1989, *ApJ*, 71, 733
- Aoki, W., Tsuji, T., & Ohnaka, K. 1998, *A&A*, 333, L19
- Bakes, E. L. O., Tielens, A. G. G. M., & Bauschlicher, C. W. 2001, *ApJ*, 556, 501
- Bauschlicher, C. W. 2002, *ApJ*, 564, 782
- Beichman, C. A., Neugebauer, G., Habing, H. J., Clegg, P. E., & Chester, T. J. 1988, *NASA Reference Publication*, 1190, 1
- Bernstein, M. P., Sandford, S. A., Allamandola, L. J., Gillette, J. S., Clemett, S. J., & Zare, R. N. 1999, *Sci*, 283, 1135
- Buss, R. H., Tielens, A. G. G. M., & Snow, T. P. 1991, *ApJ*, 372, 281
- Cherchneff, I., Barker, J. R., & Tielens, A. G. G. M. 1992, *ApJ*, 401, 269
- Cherchneff, I., Le Teuff, Y. H., Williams, P. M., & Tielens, A. G. G. M. 2000, *A&A*, 357, 572
- Claussen, M. J., Kleinmann, S. G., Joyce, R. R., & Jura, M. 1987, *ApJ*, 65, 385
- Cohen, M., Allamandola, L., Tielens, A. G. G. M., Bregman, J., Simpson, J. P., Witteborn, F. C., Wooden, D., & Rank, D. 1986, *ApJ*, 302, 737
- Cohen, M., Tielens, A. G. G. M., & Allamandola, L. J. 1985, *ApJ Lett.*, 299, L93
- de Graauw, T., Haser, L. N., Beintema, D. A., Roelfsema, P. R., van Agthoven, H., Barl, L., Bauer, O. H., Bekenkamp, H. E. G., Boonstra, A.-J., Boxhoorn, D. R., Cote, J., de Groene, P., van Dijkhuizen, C., Drapatz, S., Evers, J., Feuchtgruber, H., Frericks, M., Genzel, R., Haerendel, G., Heras, A. M., van der Hucht, K. A., van der Hulst, T., Huygen, R., Jacobs, H., Jakob, G., Kamperman, T., Katterloher, R. O., Kester, D. J. M., Kunze, D., Kussendragger, D., Lahuis, F., Lamers, H. J. G. L. M., Leech, K., van der Lei, S., van der Linden, R., Luinge, W., Lutz, D., Melzner, F., Morris, P. W., van Nguyen, D., Ploeger, G., Price, S., Salama, A., Schaeidt, S. G., Sijm, N., Smoorenburg, C., Spakman, J., Spoon, H., Steinmayer, M., Stoecker, J., Valentijn, E. A., Vandenbussche, B., Visser, H., Waelkens, C., Waters, L. B. F. M., Wensink, J., Wesselius, P. R., Wiezorrek, E., Wieprecht, E., Wijnbergen, J. J., Wildeman, K. J., & Young, E. 1996, *A&A*, 315, L49
- Draine, B. T. 1980, *ApJ*, 241, 1021
- Draine, B. T. & Anderson, N. 1985, *ApJ*, 292, 494
- Flower, P. J. 1996, *ApJ*, 469, 355

- Frenklach, M. & Feigelson, E. D. 1989, *ApJ*, 341, 372
- Geballe, T. R., Lacy, J. H., Persson, S. E., McGregor, P. J., & Soifer, B. T. 1985, *ApJ*, 292, 500
- Gillett, F. C., Forrest, W. J., & Merrill, K. M. 1973, *ApJ Lett.*, 184, L93+
- Gudipati, M. S. & Allamandola, L. J. 2003, Division for Planetary Sciences Meeting, 35,
- Hony, S. & Bouwman, J. 2004, *A&A*, 413, 981
- Hony, S., Tielens, A. G. G. M., Waters, L. B. F. M., & de Koter, A. 2003, *A&A*, 402, 211
- Hony, S., van Kerckhoven, C., Peeters, E., Tielens, A. G. G. M., Hudgins, D. M., & Allamandola, L. J. 2000, in *ESA SP-456: ISO Beyond the Peaks: The 2nd ISO Workshop on Analytical Spectroscopy*, 63–+
- Hudgins, D. M. & Allamandola, L. J. 1999, *ApJ Lett.*, 513, L69
- Kraemer, K. E., Sloan, G. C., Price, S. D., & Walker, H. J. 2002, *ApJ*, 140, 389
- Kukarkin, B. V., Kholopov, P. N., Pskovsky, Y. P., Efremov, Y. N., Kukarkina, N. P., Kurochkin, N. E., & Medvedeva, G. I. 1971, in *General Catalogue of Variable Stars*, 3rd ed. (1971), 0–+
- Le Teuff, Y. H., Millar, T. J., & Markwick, A. J. 2000, *A&AS*, 146, 157
- Leech, K., Kester, D., Shipman, R., Beintema, D., Feuchtgruber, H., Heras, A., Huygen, R., Lahuis, F., Lutz, D., Morris, P., Roelfsema, P., Salama, A., Schaeidt, S., Valentijn, E., Vandebussche, B., Wieprecht, E., & de Graauw, T., eds. 2003, *The ISO Handbook, Volume V - SWS - The Short Wavelength Spectrometer*
- Leger, A. & Puget, J. L. 1984, *A&A*, 137, L5
- Messenger, S. R. 1997, Ph.D. Thesis
- Nahar, S. N., Bautista, M. A., & Pradhan, A. K. 1997, *ApJ*, 479, 497
- Neugebauer, G. & Leighton, R. B. 1969, *Two-micron sky survey. A preliminary catalogue* (NASA SP, Washington: NASA, 1969)
- Nicolet, B. 1978, *A&AS*, 34, 1
- Olson, B. I. & Richer, H. B. 1975, *ApJ*, 200, 88
- Omont, A. 1986, *A&A*, 164, 159
- Osterbrock, D. E. 1974, *Astrophysics of gaseous nebulae* (Research supported by the Research Corp., Wisconsin Alumni Research Foundation, John Simon Guggenheim Memorial Foundation, Institute for Advanced Studies, and National Science Foundation. San Francisco, W. H. Freeman and Co., 1974. 263 p.)
- Peeters, E., Hony, S., Van Kerckhoven, C., Tielens, A. G. G. M., Allamandola, L. J., Hudgins, D. M., & Bauschlicher, C. W. 2002, *A&A*, 390, 1089
- Peeters, E., van Dienenhoven, B., van Kerckhoven, C., Hony, S., Tielens, A. G. G. M., Allamandola, L. J., Hudgins, D. M., & Bauschlicher, C. W. 2003, in *Astrophysics of Dust*

- Perryman, M. A. C., Lindegren, L., Kovalevsky, J., Hoeg, E., Bastian, U., Bernacca, P. L., Cr ez e, M., Donati, F., Grenon, M., van Leeuwen, F., van der Marel, H., Mignard, F., Murray, C. A., Le Poole, R. S., Schrijver, H., Turon, C., Arenou, F., Froeschl e, M., & Petersen, C. S. 1997, *A&A*, 323, L49
- Puget, J. L. & Leger, A. 1989, *ARA&A*, 27, 161
- Purcell, E. M. 1979, *ApJ*, 231, 404
- Richer, H. B. 1971, *ApJ*, 167, 521
- . 1972, *ApJ Lett.*, 172, L63+
- Salpeter, E. E. 1971, *ARA&A*, 9, 127
- Sellgren, K. 1984, *ApJ*, 277, 623
- Shane, C. D. 1925, *PASP*, 37, 35
- Spaans, M., Tielens, A. G. G. M., van Dishoeck, E. F., & Bakes, E. L. O. 1994, *ApJ*, 437, 270
- Speck, A. K. & Barlow, M. J. 1997, *Ap&SS*, 251, 115
- Strazulla, G., Arena, M., Baratta, G. A., Castorina, C. A., Celi, G., Leto, G., Palumbo, M. E., & Spinella, F. 1995, *Advances in Space Research*, 16, 61
- Voelk, H. J., Morfill, G. E., Roeser, S., & Jones, F. C. 1980, *A&A*, 85, 316
- Wilson, R. E. 1953, *Carnegie Institute Washington D.C. Publication*, 0
- Zombeck, M. V. 1990, *Handbook of Astronomy and Astrophysics, Second Edition* (Cambridge, UK: Cambridge University Press, 1990)

List of Figures

1.1	A sketch of the evolution of a low-mass star in the Hertzsprung-Russel diagram. Indicated are the evolutionary stages.	
1.2	Schematic overview of the layout of ESA's Infrared Space Observatory (ISO). Source Leech et al. (2003)	5
1.3	Schematic overview of the SWS instrument carried by ISO. Source de Graauw et al. (1996).	6
1.4	ISO - SWS spectra of RY Dra showing most of the typical features, including molecular and dust features, in carbon-rich stars.	
1.5	The IR emission features in the mid-IR spectra of the planetary nebula NGC 7027. Indicated are some of the UIR features.	
1.6	The structure of benzene. a: the σ -bonding framework of benzene. b: the p orbitals which form the delocalized π system.	
1.7	PAH example, circum-coronene ($C_{42}H_{16}$).	11
1.8	The structure of acetylene. A: σ bonds in acetylene and the electron orbitals. B: π bonds in acetylene. C: structure of the molecule.	
1.9	The structure of fullerene, better known as the "Bucky Ball".	15
1.10	ISO SWS spectrum of TU Tau, indicated are the molecular line positions, dust features (below) and the UIR wave-lengths.	
2.1	Three spectra shown from 2.8 μm to 3.4 μm . Each spectrum has been normalized to the maximum flux level of the continuum.	
2.2	Classification color map showing the locations of the stars from the subset. The spectrum ID has been linear color-coded.	
2.3	Distance downsampled spectrum of W Ori, dark line, and the spectrum of TU Tau, gray line. In the box the residual spectrum is shown.	
2.4	Top: The mean normalized spectrum from the subsample of nine carbon-rich AGB stars. The dark solid curve is the mean spectrum.	
2.5	Overview of the spectra in the subsample. Indicated above the spectra are the locations of the possible PAH features.	
2.6	Left panels: the spectra from the subsample with fitted blackbody curves. Right panels: residual spectra.	32
2.7	Power-law fits, with power-law index $\gamma = 1$, to the local continuum (dashed lines) for the selected three stars (see 2.3).	
2.8	Left: Scaled spectra of the three selected stars from 4.0 - 7.0 μm . Right: Scaled spectra of three selected stars from the subsample.	
2.9	<i>method 2</i> fitting routine with W Ori as selected comparison star. See text for details.	37
2.10	<i>method 2</i> fitting routine with S Sct as selected comparison star. See text for details.	38
2.11	<i>method 2</i> fitting routine with VX And as selected comparison star. See text for details.	40
2.12	Matching the SiC emission of TU Tau.	41
2.13	Top: residual spectrum from comparing TU Tau with W Ori. Bottom: residual from comparing TU Tau with the mean spectrum.	
2.14	Residual spectra for comparing TU Tau with W Ori (top), S Sct (middle) and VX And (bottom), using <i>method 1</i> .	
2.15	Residual spectra for comparing TU Tau with W Ori (top), S Sct (middle) and VX And (bottom), using <i>method 2</i> .	
2.16	Main result: 6.22, 7.6 + 7.95, 8.6 and 11.2 μm profiles. The maxima have been normalized to one.	50
2.17	Main result with an 'extra' continuum component subtracted: 6.22, 7.7 + 8.6 and 11.2 μm profiles. The maxima have been normalized to one.	
3.1	Top: the profiles from Peeters et al. (2002) and Peeters et al. (2003). The colors represent for the C-C modes: red (C-C), blue (C-C), green (C-C), yellow (C-C), orange (C-C), purple (C-C).	
3.2	The matching UIR band profiles (class B and B _{11,2}) have been overlaid on the UIR band profiles from TU Tau.	55
3.3	Band strength ratios. Squares indicate HII regions, triangles indicate intermediate mass star forming regions, crosses indicate other regions.	
4.1	Schematic evolution scheme for PAHs. In each phase the PAH family can be altered due to the differences in physical conditions.	
A.1	ISO - SWS spectra for HD19557 and TX PSC.	79
A.2	ISO - SWS spectra for TX PSC, V AQLY, CVN and TU TAU.	80
A.3	ISO - SWS spectra for V S SCT, V460 CYG, 460 CYG and T IND.	81
A.4	ISO - SWS spectra for T IND, W ORI, RY DRA and SS 485.	82
A.5	ISO - SWS spectra for VX AND, R FOR, RU VIR and CS 3070.	83
A.6	ISO - SWS spectra for V CRB, V CRB, V CRB and V CRB.	84
A.7	ISO - SWS spectra for V CRB, V CRB SS VIR and AFGL 933.	85
A.8	ISO - SWS spectra for CS 2429 and T DRA, T DRA and T DRA.	86
A.9	ISO - SWS spectra for T DRA, T DRA, T DRA and T DRA.	87

A.10	iso - sws spectra for T DRA, U CAM, S SEP and S SEP.	88
A.11	iso - sws spectra for V CYG, V CYG, V CYG and V CYG.	89
A.12	iso - sws spectra for V CYG, V CYG, R SCL and R SCL.	90
A.13	iso - sws spectra for R SCL, R SCL, R SCL and R SCL.	91
B.1	2.5 + 2.6 μm Equivalent Width plotted against the 3.0 μm Equivalent Width, based on the occurrence of C_2H_2 and	
B.2	2.5 + 2.6 μm Equivalent Width plotted against 3.9 μm Equivalent Width, based on the occurrence of C_2H_2	95
B.3	2.5 + 2.6 μm Equivalent Width plotted against 13.7 μm Equivalent Width, based on the occurrence of C_2H_2 and	
B.4	3.0 μm Equivalent Width plotted against 3.9 μm Equivalent Width, based on the occurrence of C_2H_2	95
B.5	3.0 μm Equivalent Width plotted against 13.7 μm Equivalent Width, based on the occurrence of HCN.	95
B.6	3.9 μm Equivalent Width plotted against 13.7 μm Equivalent Width, based on the occurrence of C_2H_2	96
B.7	2.5 + 2.6 μm Equivalent Width plotted against 7.9 μm Equivalent Width, based on the occurrence of HCN.	96
B.8	2.5 + 2.6 μm Equivalent Width plotted against 7.9 μm Equivalent Width, based on the occurrence of HCN.	97
B.9	3.0 μm Equivalent Width plotted against 7.9 μm Equivalent Width, based on the occurrence of HCN.	97
B.10	2.5 + 2.6 μm Equivalent Width plotted against 5.0 μm Equivalent Width, based on the occurrence of CO.	98
C.1	Classification color map where the spectrum ID has been linear color coded.	99
C.2	Classification color map where the sorted 2.5 + 2.6 μm Equivalent Widths have been linear color coded.	100
C.3	Classification color map where the sorted auto-fitted blackbody temperatures have been linear color coded.	100
C.4	Classification color map where the sorted 3.0. μm Equivalent Widths have been linear color coded.	101
C.5	Classification color map where the sorted 3.9. μm Equivalent Widths have been linear color coded.	101
C.6	Classification color map where the sorted 5.0. μm Equivalent Widths have been linear color coded.	102
C.7	Classification color map where the sorted 7.9. μm Equivalent Widths have been linear color coded.	102
C.8	Classification color map where the sorted 11.3 μm Equivalent Widths have been linear color coded.	103
C.9	Classification color map where the sorted 13.7. μm Equivalent Widths have been linear color coded.	103
D.1	Resulting residual UIR band emission when using <i>method 2</i> with a fixed power-law index of $\gamma = 1$ and W Ori as seed	
D.2	Resulting residual UIR band emission when using <i>method 2</i> with a fixed power-law index of $\gamma = 1$ and S Sct as seed	
D.3	Resulting residual UIR band emission when using <i>method 2</i> with a fixed power-law index of $\gamma = 1$ and VX And as seed	

List of Tables

1.1	sws band specifications. Source Leech et al. (2003).	7
1.2	Identified bands in carbon-rich AGB stars, including molecular and dust features. .	9
1.3	The two main PAH classes with some examples.	12
1.4	Some properties for fully centrally condensed PAHS.	12
1.5	The IR emission features with wavelengths and mode identifications.	13
1.6	sws01 speed specifications. Duration is the duration of the scan, Reset Interval is the time between detector resets.	
1.7	Properties of TU Tau, with references to the data.	18
1.8	The sample.	20
2.1	Overview of the 50 stars from the sample and their deduced properties. Shown are the auto-fitted blackbody temperatures.	
2.2	Features under investigation shown together with their carrier(s) and the adopted integration ranges.	24
2.3	Overview of the features carried by common species and for which plots have been made.	25
2.4	The subsample: selected carbon-rich AGB stars with fitted blackbody temperatures and distance factor.	26
2.5	Scaling parameters (<i>method 1</i>).	34
2.6	Scaling parameters using <i>method 2</i> , with linear correlation coefficients R^2	36
2.7	Continuum and scaling parameters between 10.0 - 13.0 μm	39
2.8	Residual UIR band profile characterizations for TU Tau. The star names indicate the spectrum used to match TU Tau.	
3.1	Classification scheme for the 6.22, 7.7 complex and 8.6 μm profiles, λ_0 indicates the peak position. The 7.7 μm complex.	
3.2	Classification scheme for the 3.3 μm and 11.2 μm profiles. Adopted from Peeters et al. (2003).	55
3.3	Flux ratios for the UIR bands of TU Tau.	56
3.4	Integration ranges used for the determination for the flux ratios in the UIR bands of TU Tau.	56
D.1	Refined scaling parameters for <i>method 1</i> using fit routine from <i>method 2</i>	105

Appendix A

ISO - SWS spectra

This appendix presents the 50 iso - sws spectra used in this work. Plotted is the flux, in Jy, against wavelength, in μm . The spectra have a resolution $R = 300$ ($4 \times$ oversampled).

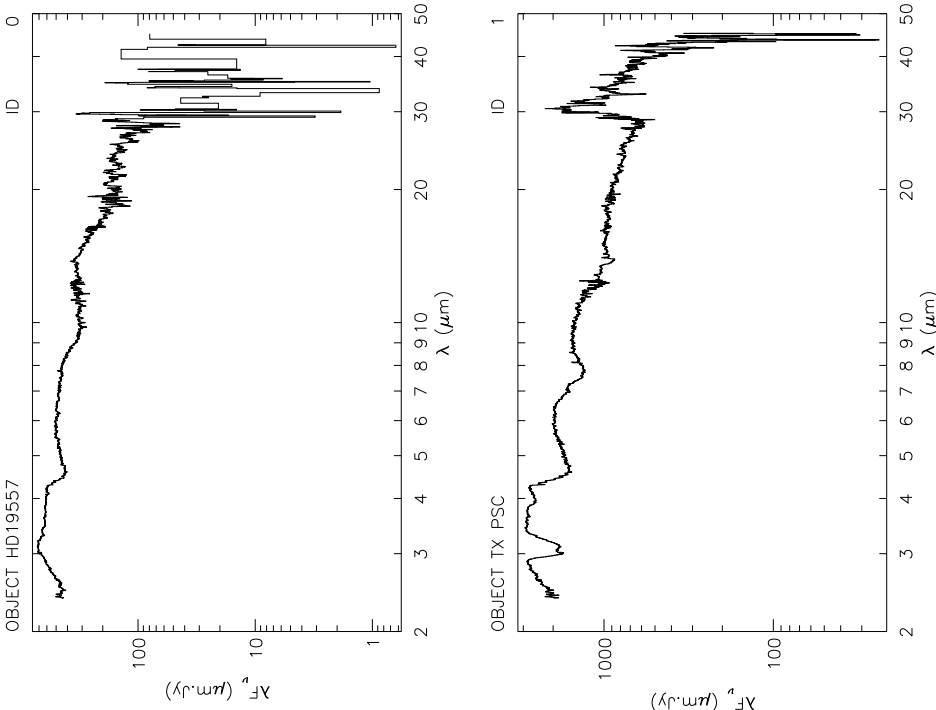


Figure A.1— iso - sws spectra for HD19557 and TX PSC.

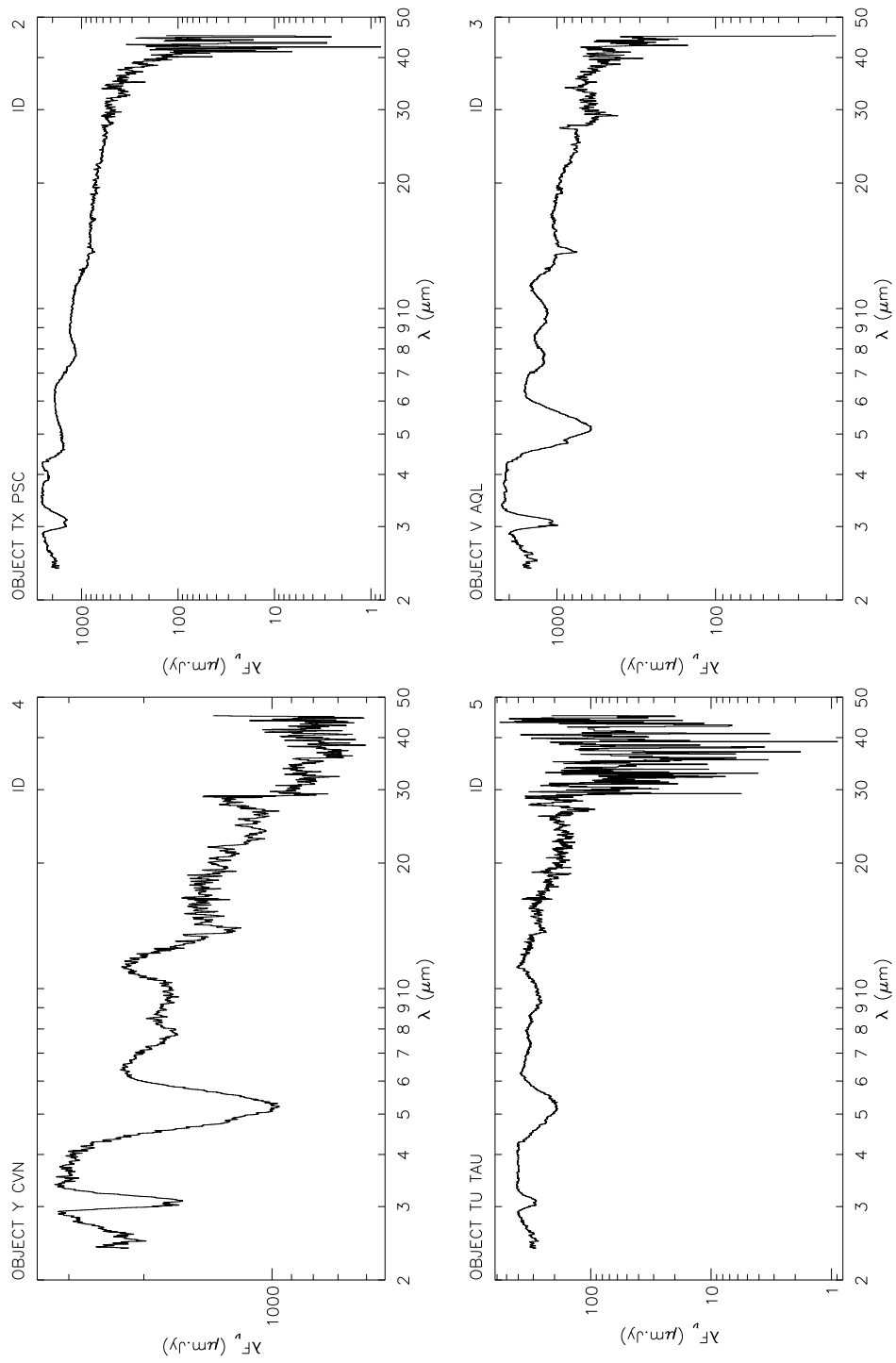


Figure A.2— iso - sws spectra for TX PSC, V AQL, CVN and TU TAU.

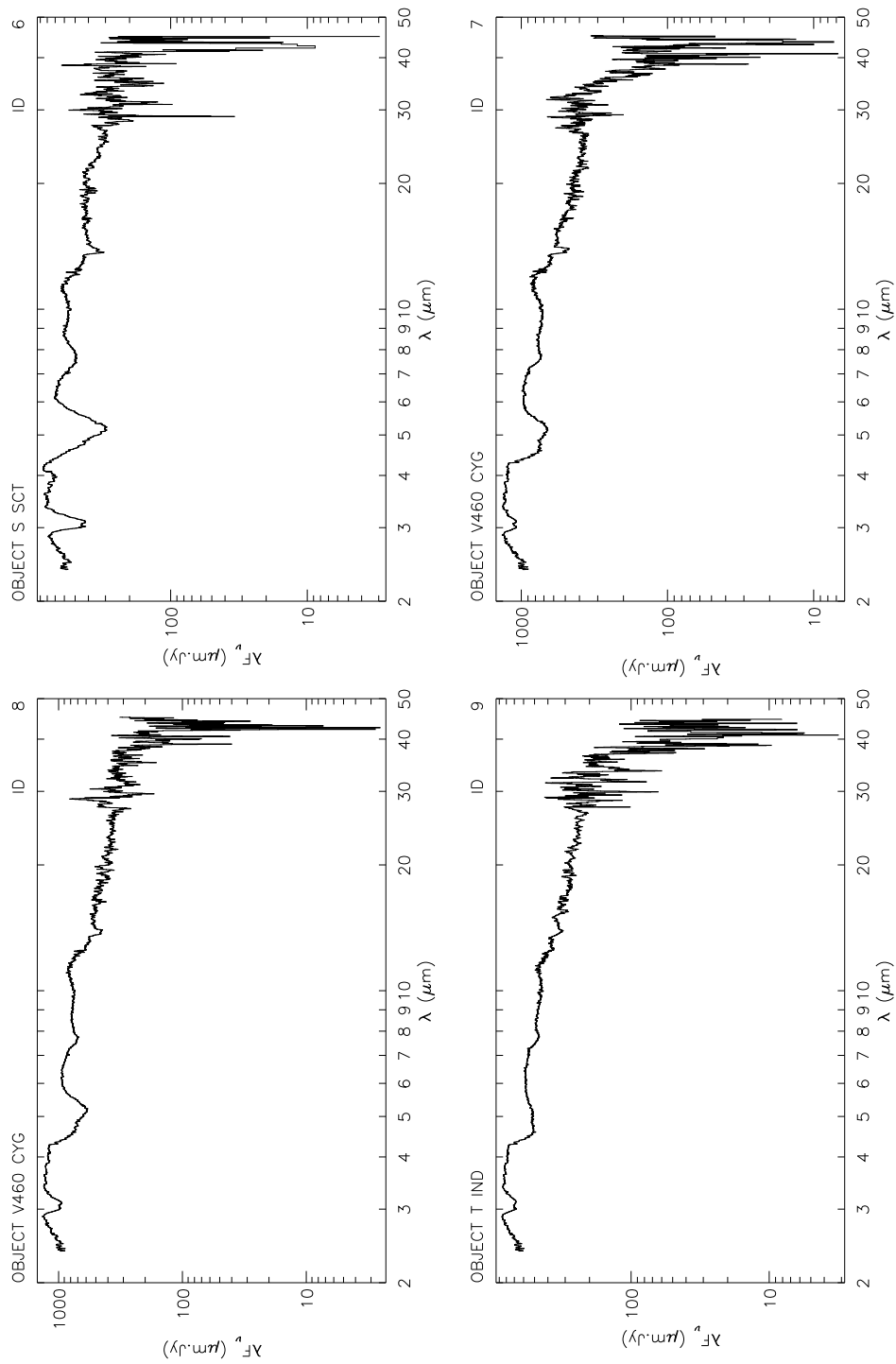


Figure A.3— iso - sws spectra for V S SCT, V460 CYG, 460 CYG and T IND.

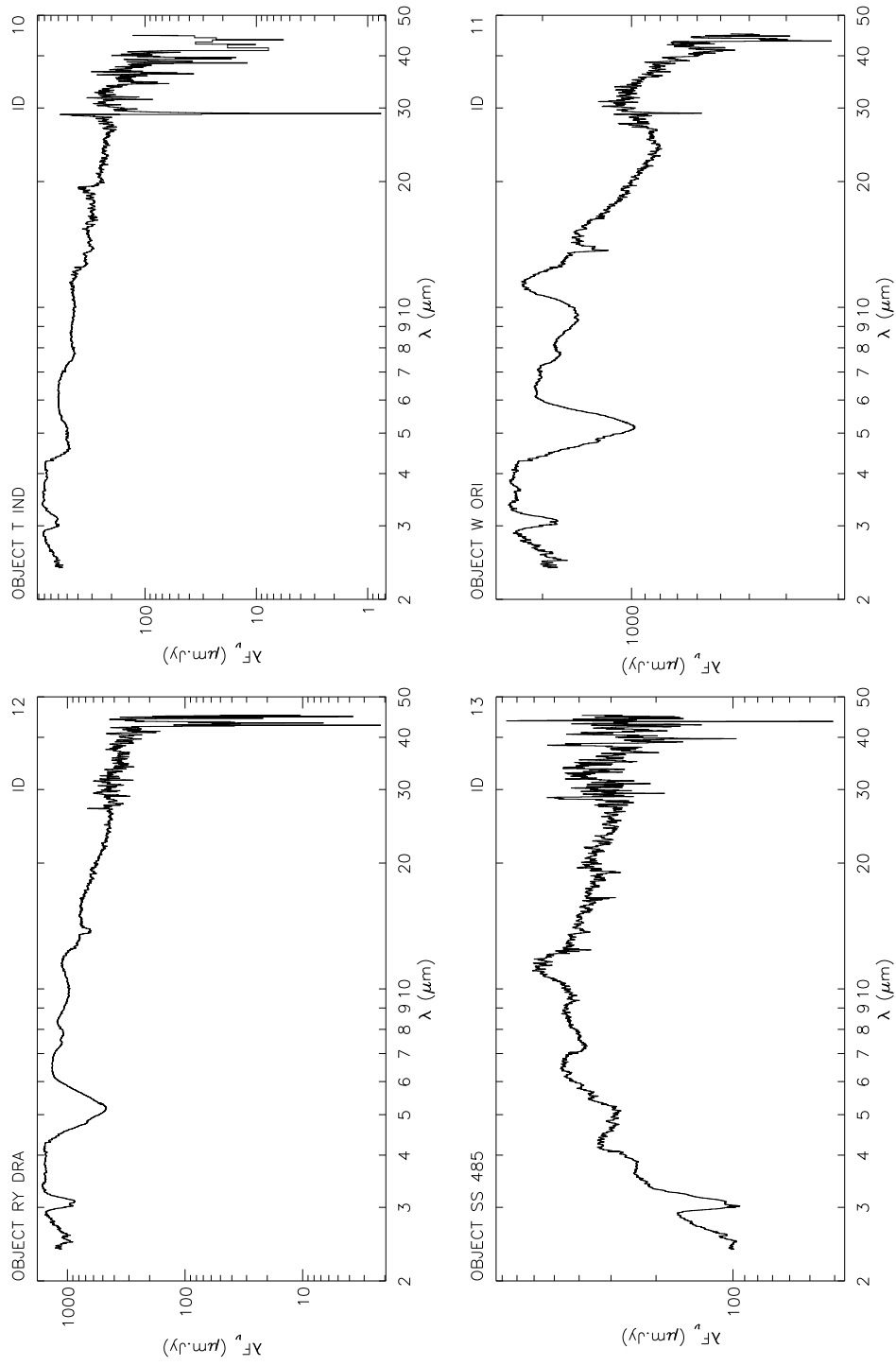


Figure A.4— iso - sws spectra for T IND, W ORI, RY DRA and SS 485.

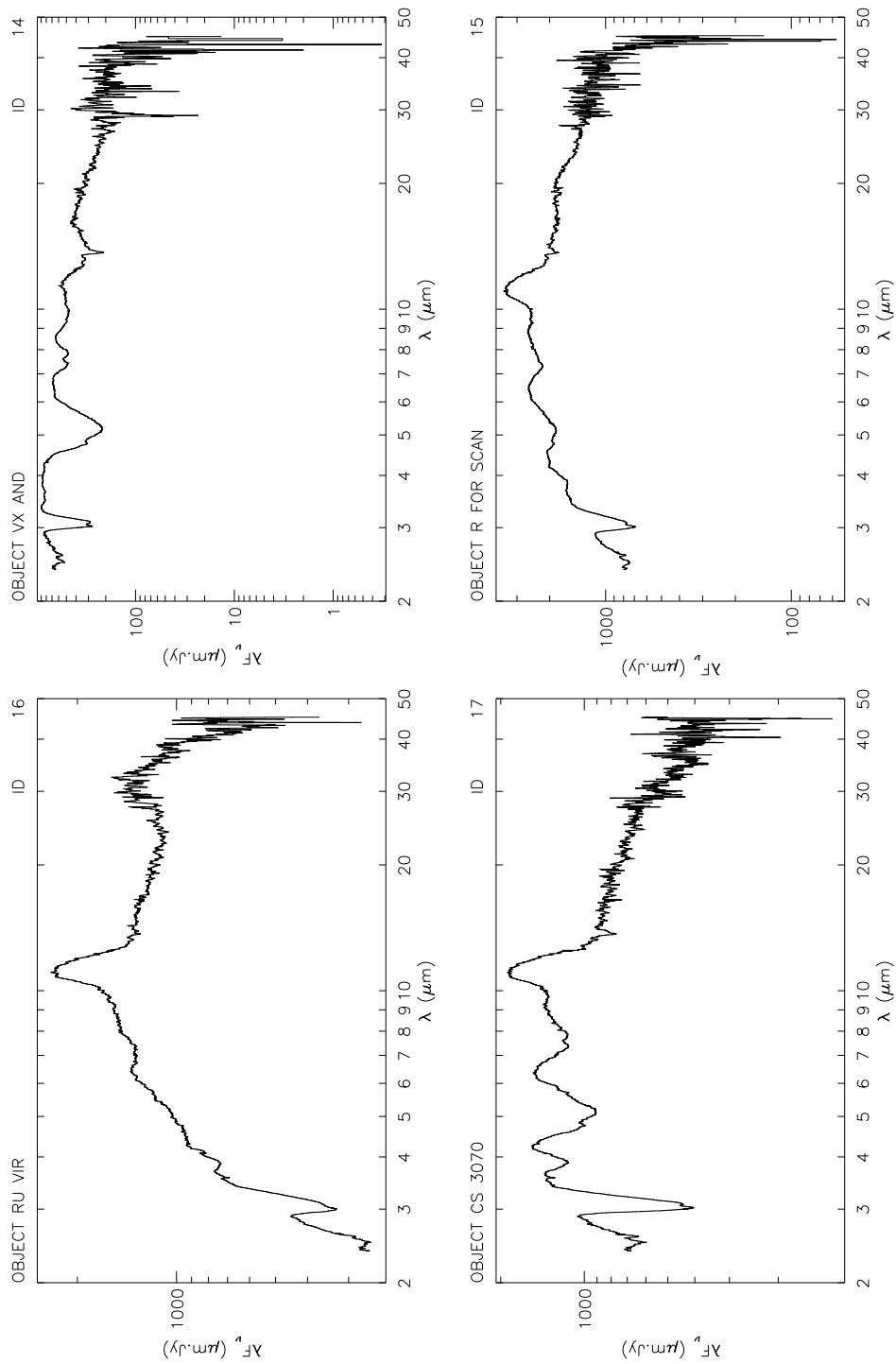


Figure A.5— iso - sws spectra for VX AND, R FOR, RU VIR and CS 3070.

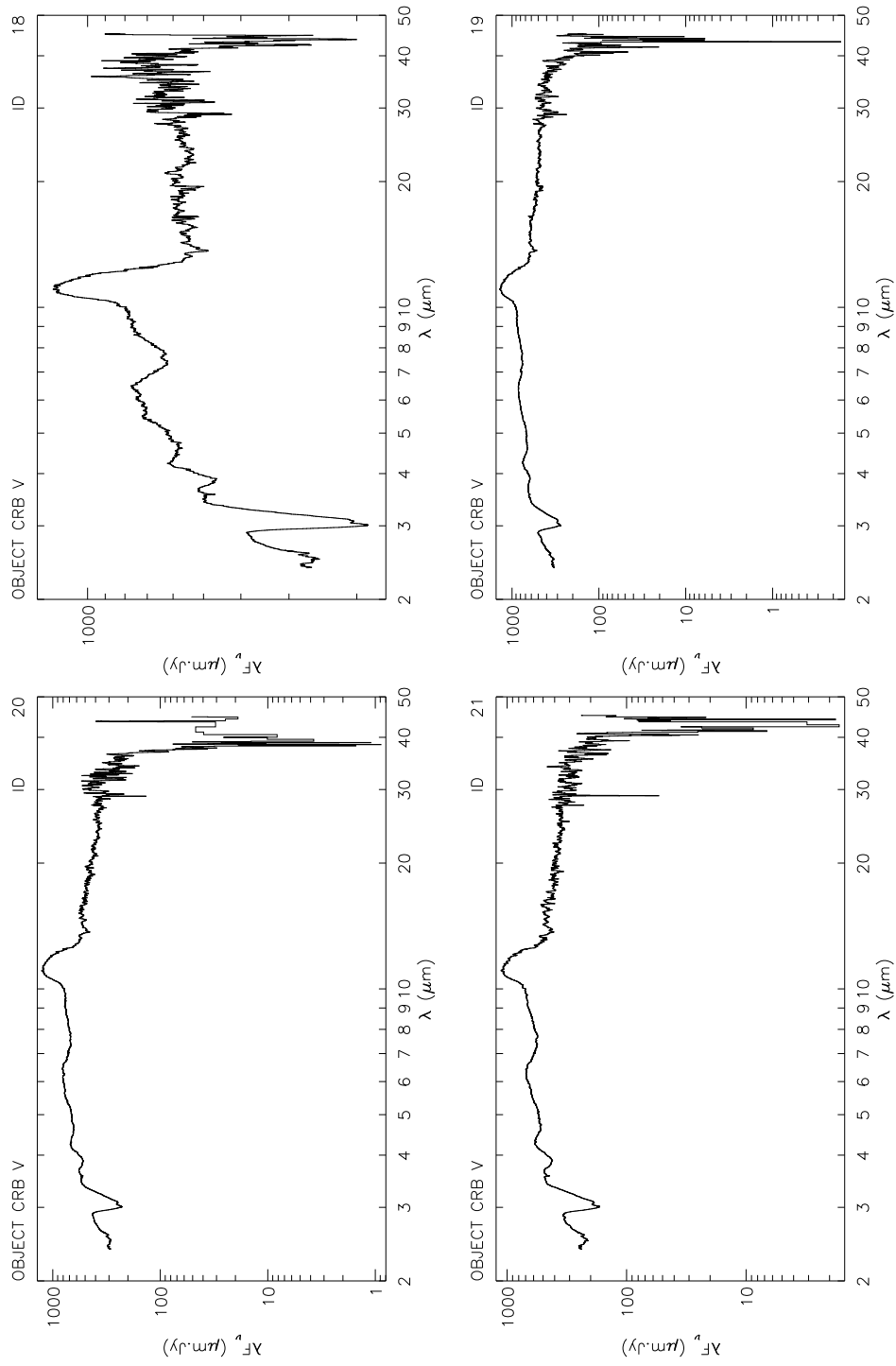


Figure A.6— ISO - sws spectra for V CRB, V CRB, V CRB and V CRB.

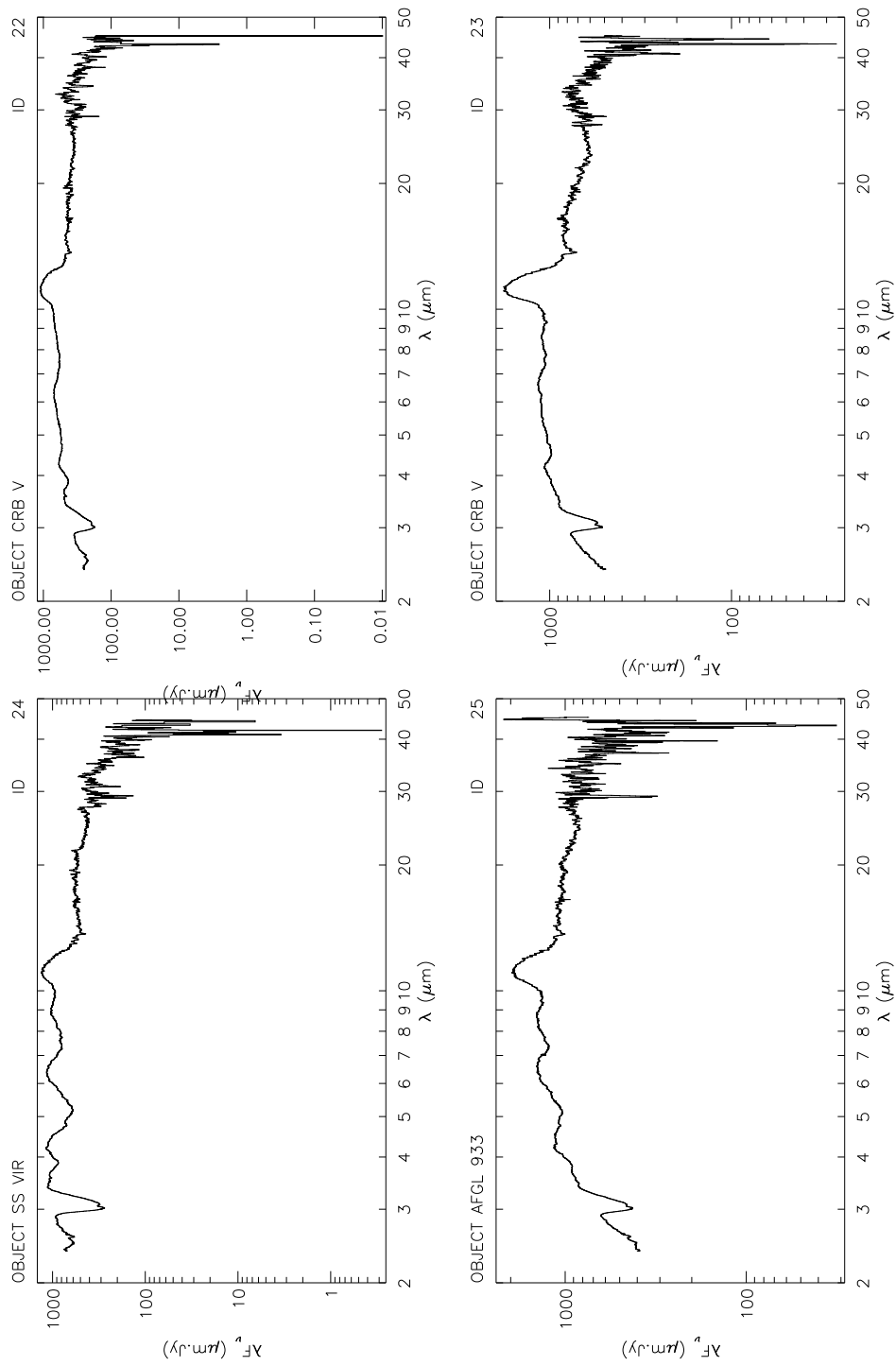


Figure A.7— ISO - sws spectra for V CRB, V CRB SS VIR and AFGL 933.

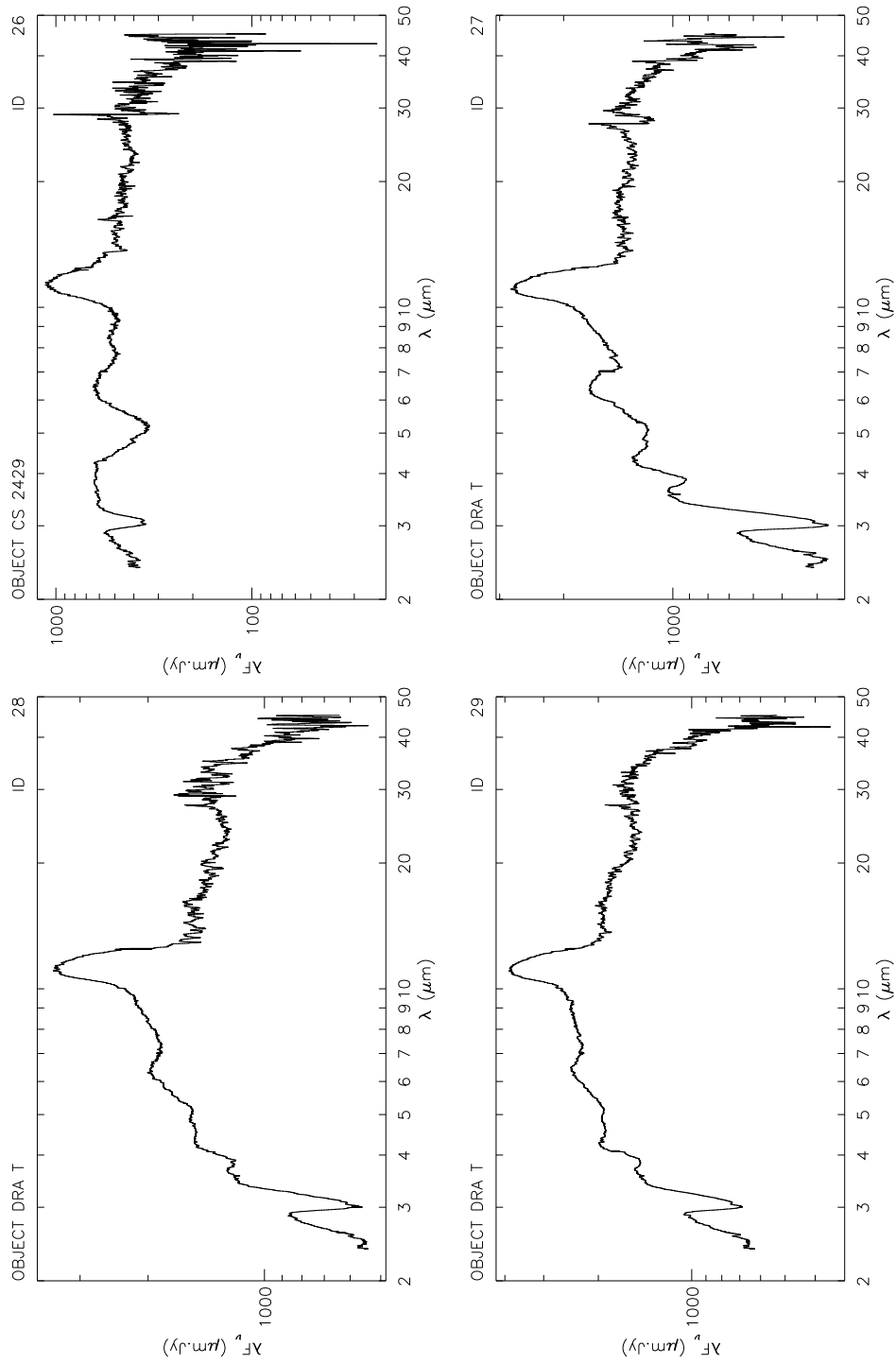


Figure A.8— iso - sws spectra for CS 2429 and T DRA, T DRA and T DRA.

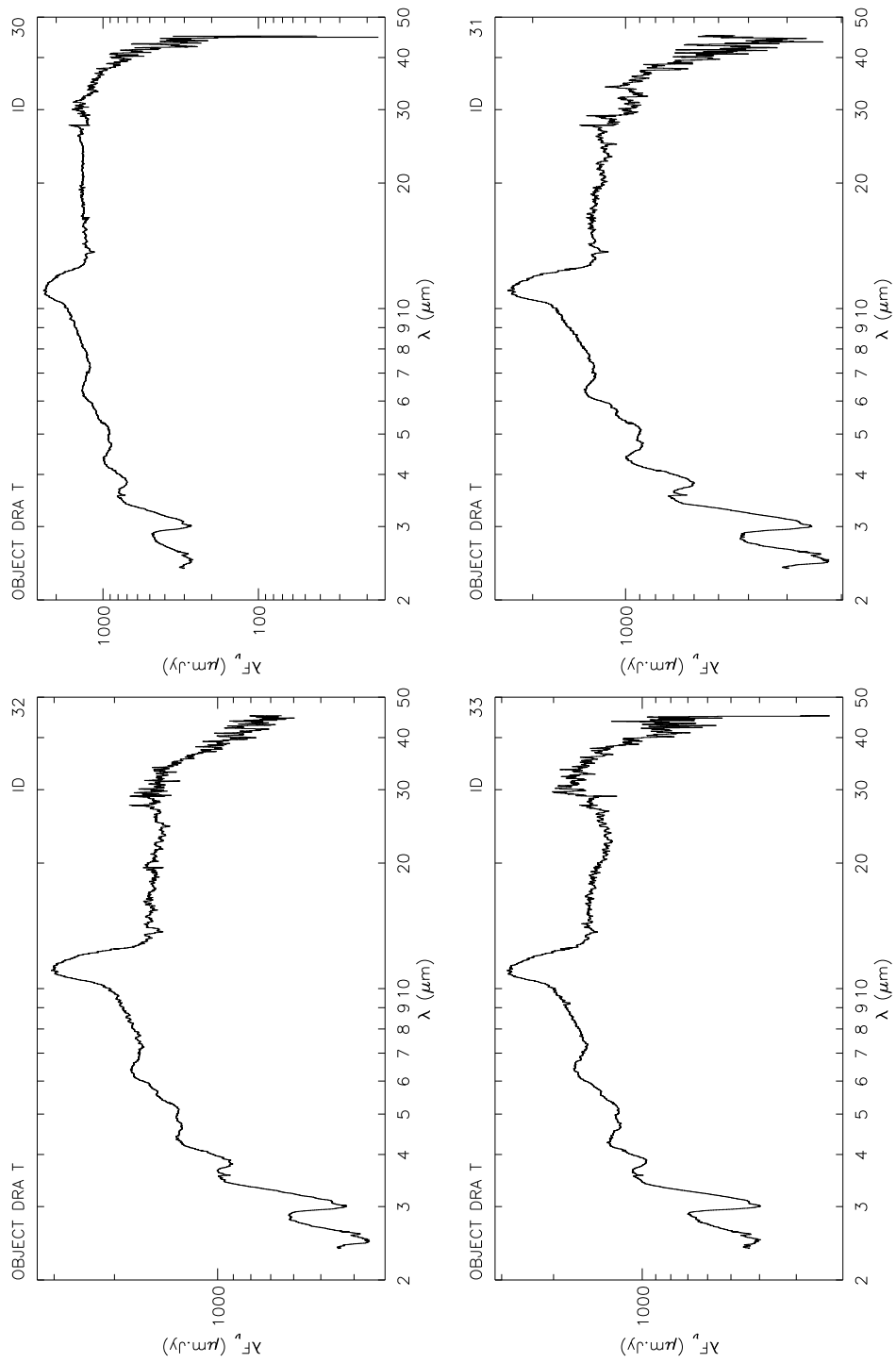


Figure A.9— ISO - sws spectra for T DRA, T DRA, T DRA and T DRA.

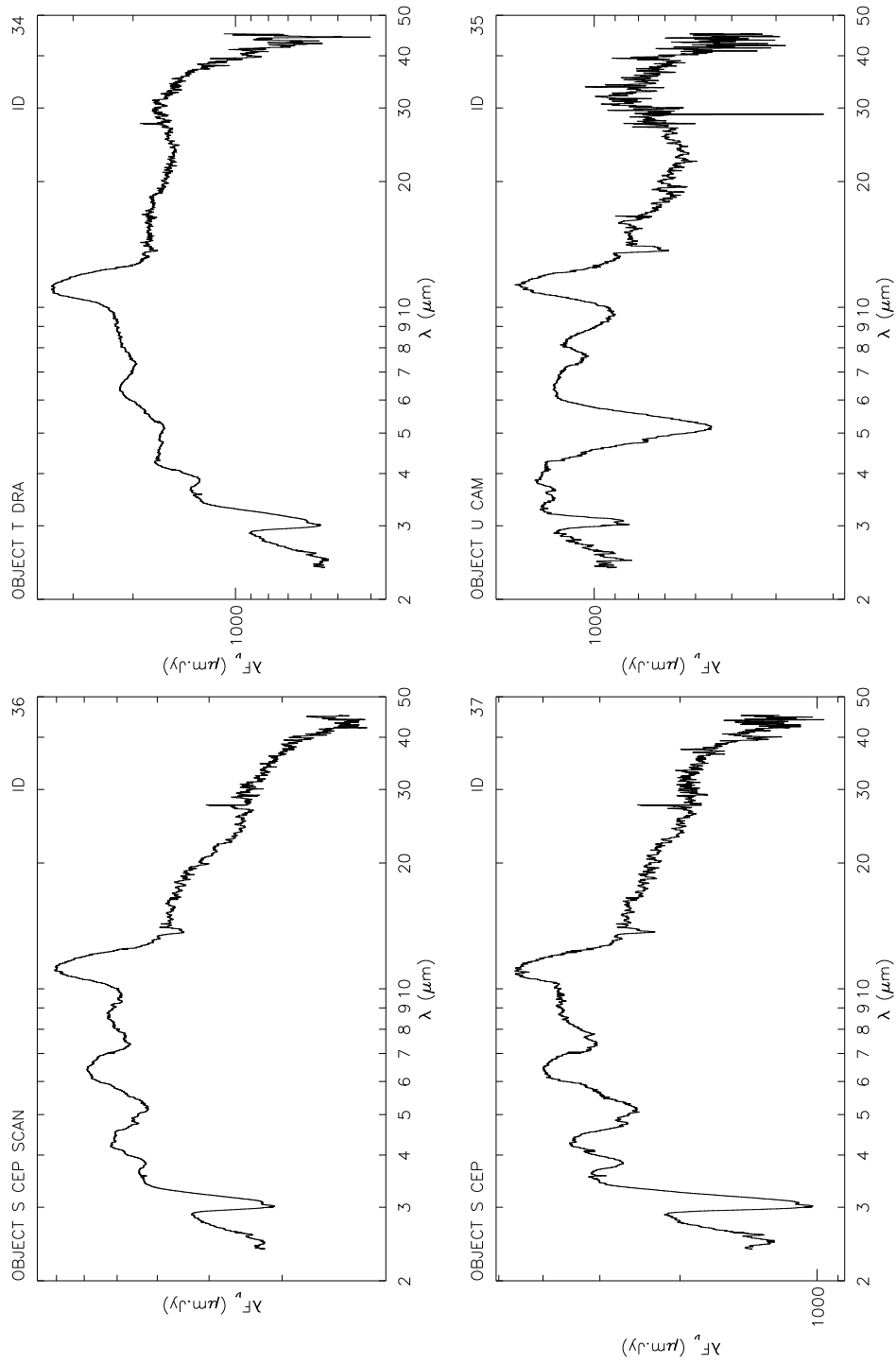


Figure A.10— ISO - sws spectra for T DRA, U CAM, S SEP and S SEP.

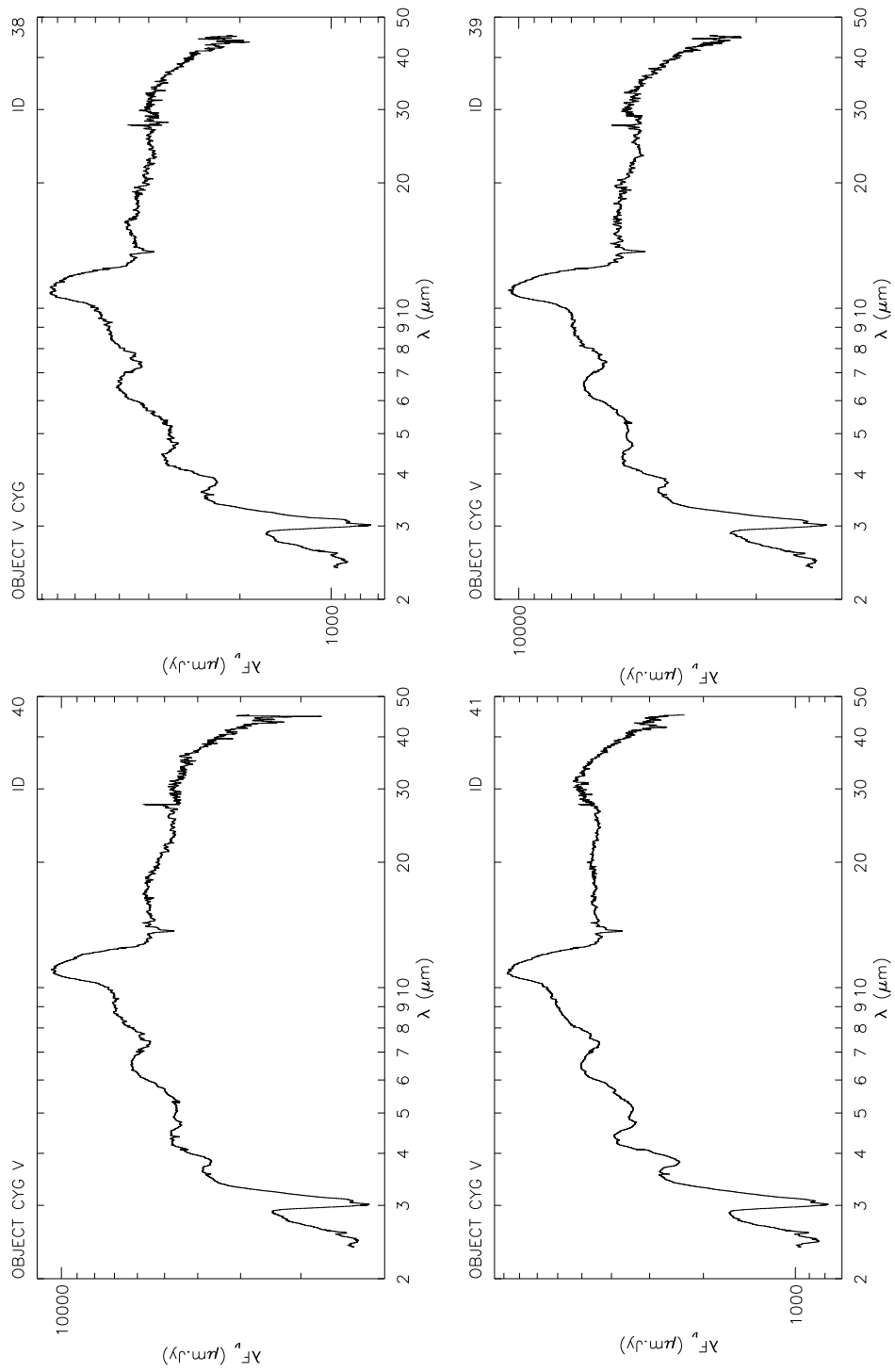


Figure A.11— ISO - sws spectra for V CYG, V CYG, V CYG and V CYG.

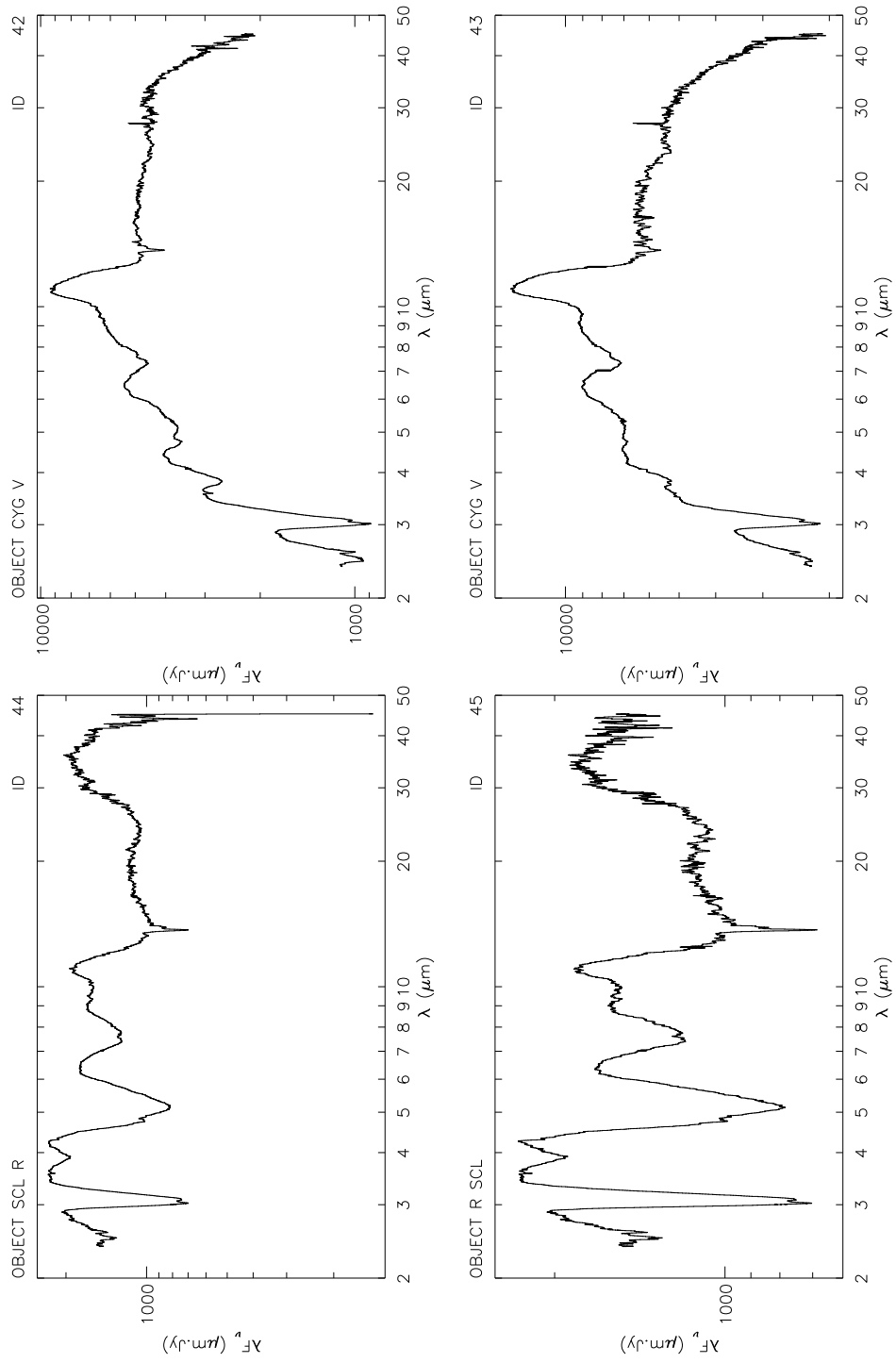


Figure A.12— iso - sws spectra for V CYG, V CYG, R SCL and R SCL.

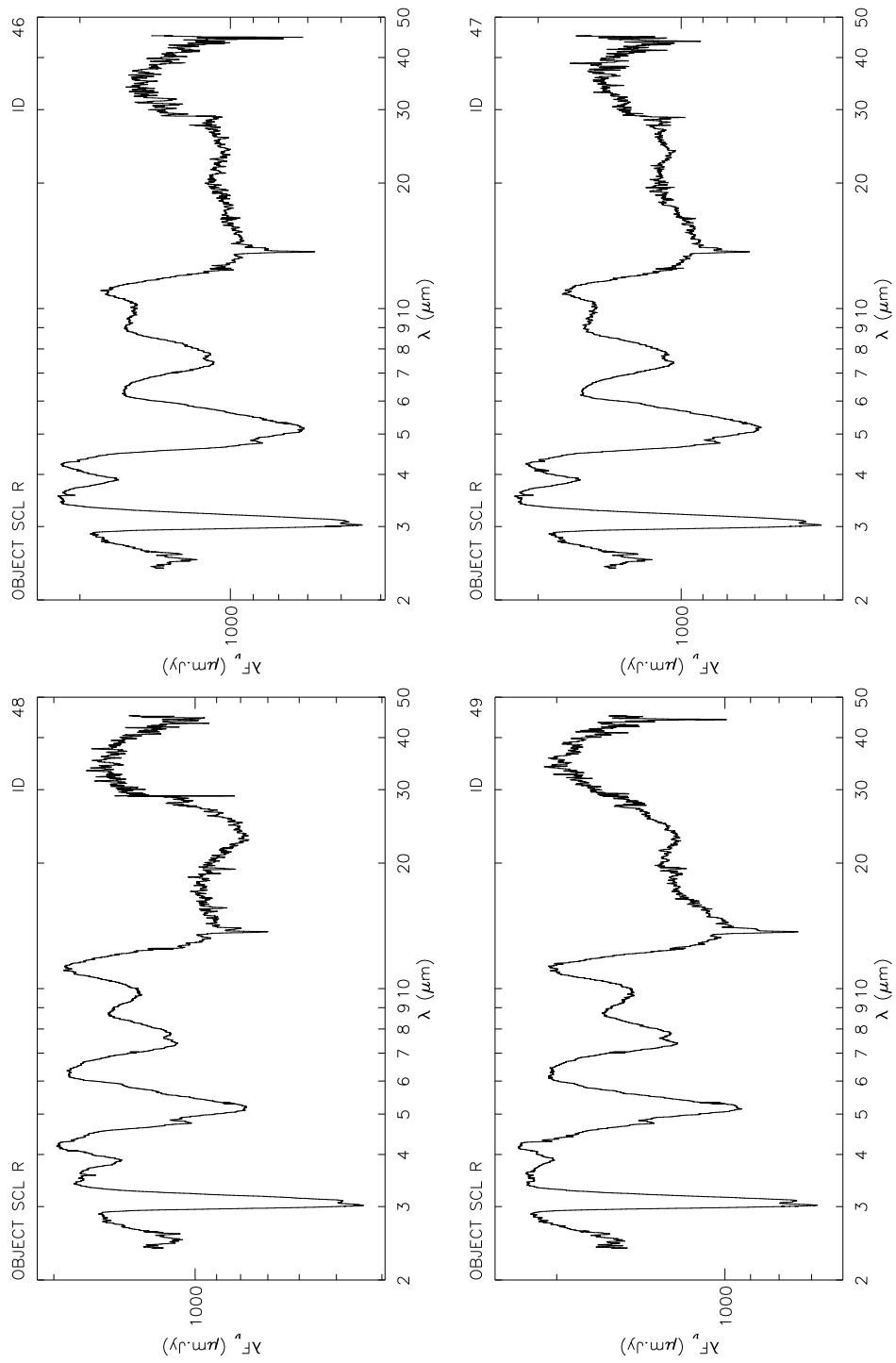


Figure A.13— iso - sws spectra for R SCL, R SCL, R SCL and R SCL.

Appendix B

Equivalent Widths

This appendix presents, for the selected spectra given in Table 2.1, the EW for the features given in Table 2.2, plotted in pairs against each other. Also the fractional EW s have been drawn against the $13.7 \mu\text{m}$ EW . TU Tau is colored purple in each of the plots.

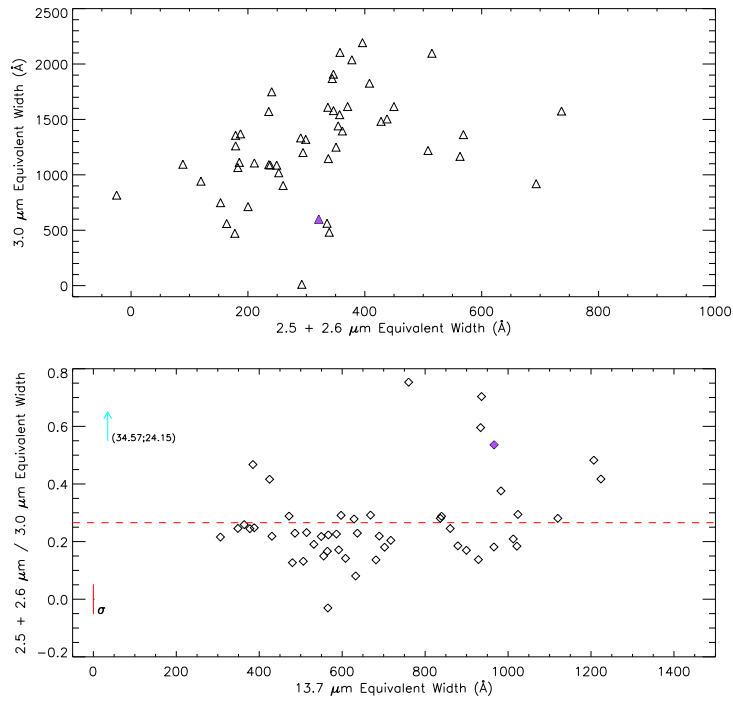


Figure B.1— $2.5 + 2.6 \mu\text{m}$ Equivalent Width plotted against the $3.0 \mu\text{m}$ Equivalent Width, based on the occurrence of C_2H_2 and HCN .

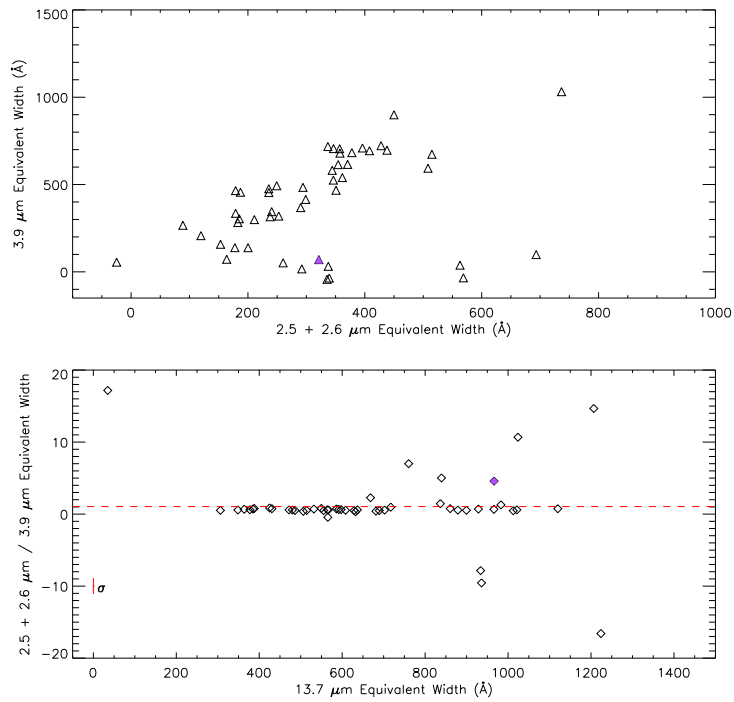


Figure B.2— 2.5 + 2.6 μm Equivalent Width plotted against 3.9 μm Equivalent Width, based on the occurrence of C_2H_2 .

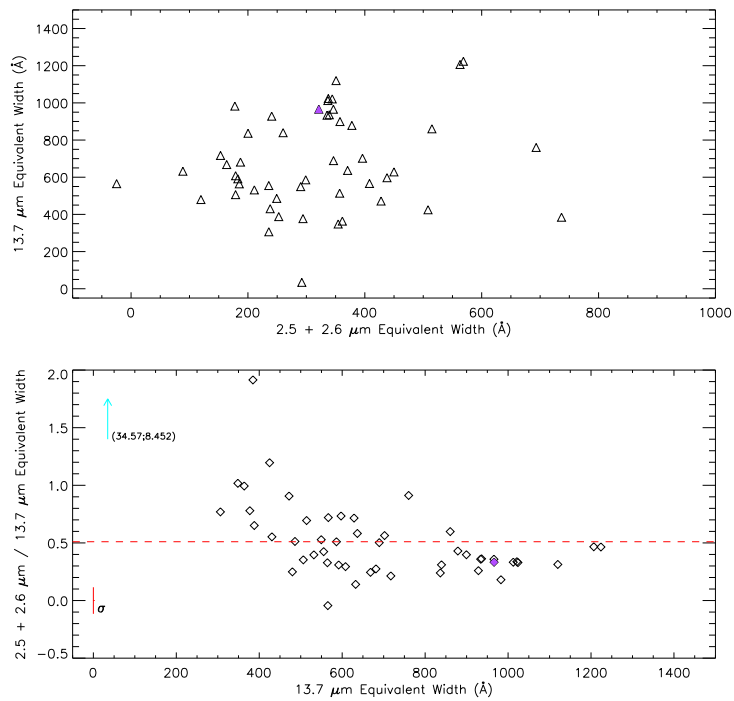


Figure B.3— 2.5 + 2.6 μm Equivalent Width plotted against 13.7 μm Equivalent Width, based on the occurrence of C_2H_2 and HCN.

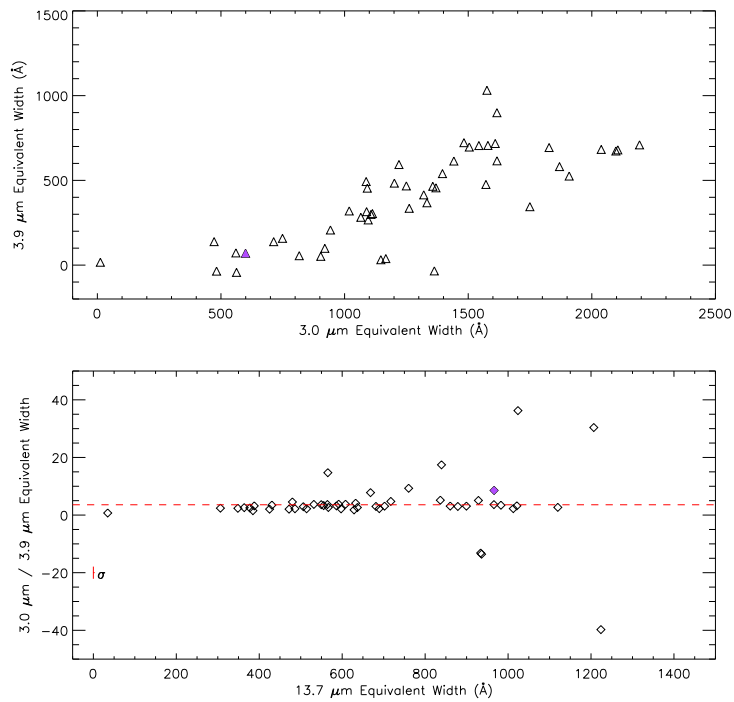


Figure B.4— 3.0 μm Equivalent Width plotted against 3.9 μm Equivalent Width, based on the occurrence of C_2H_2 .

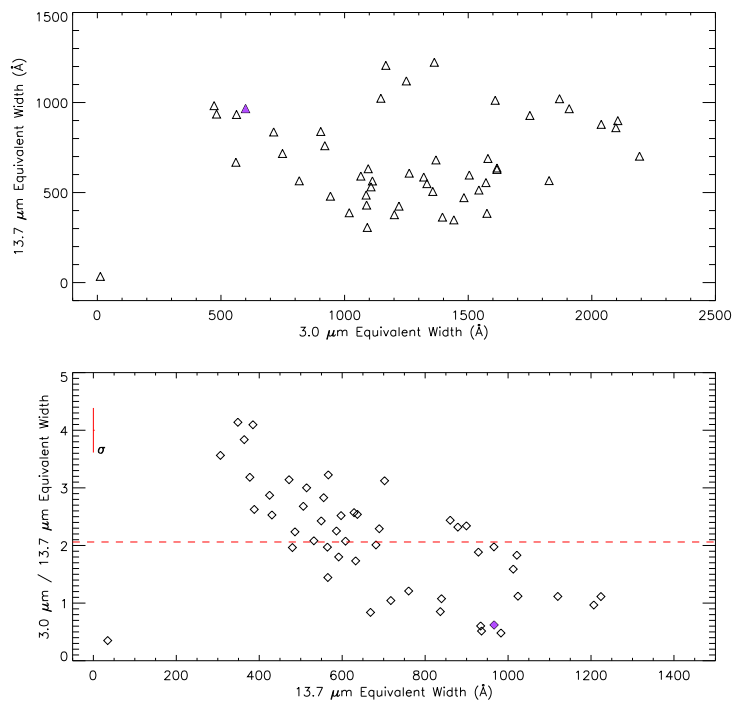


Figure B.5— 3.0 μm Equivalent Width plotted against 13.7 μm Equivalent Width, based on the occurrence of HCN.

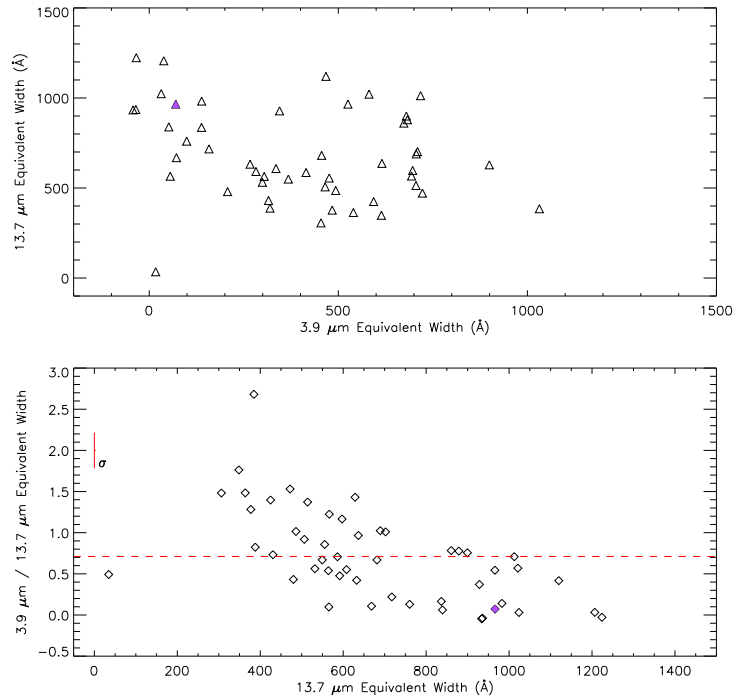


Figure B.6— 3.9 μm Equivalent Width plotted against 13.7 μm Equivalent Width, based on the occurrence of C_2H_2 .

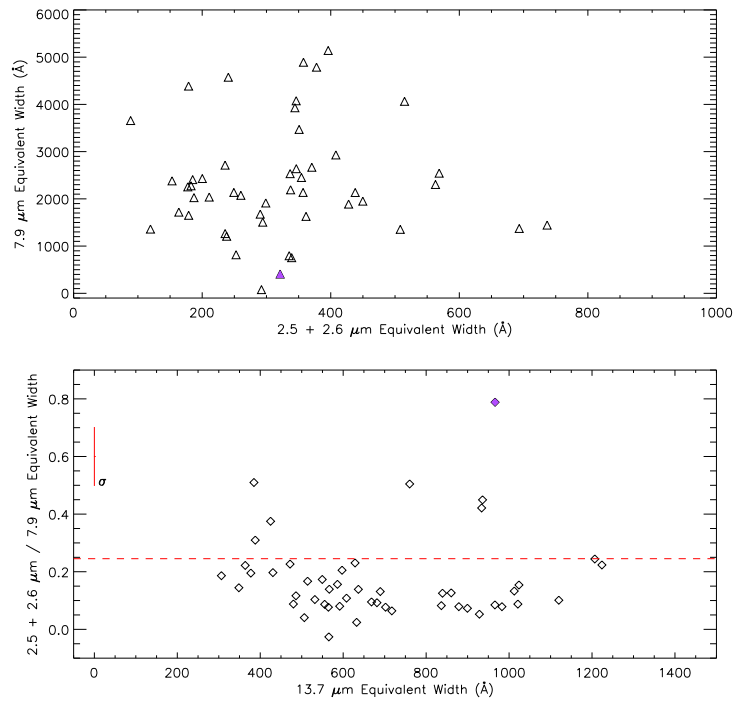


Figure B.7— 2.5 + 2.6 μm Equivalent Width plotted against 7.9 μm Equivalent Width, based on the occurrence of HCN .

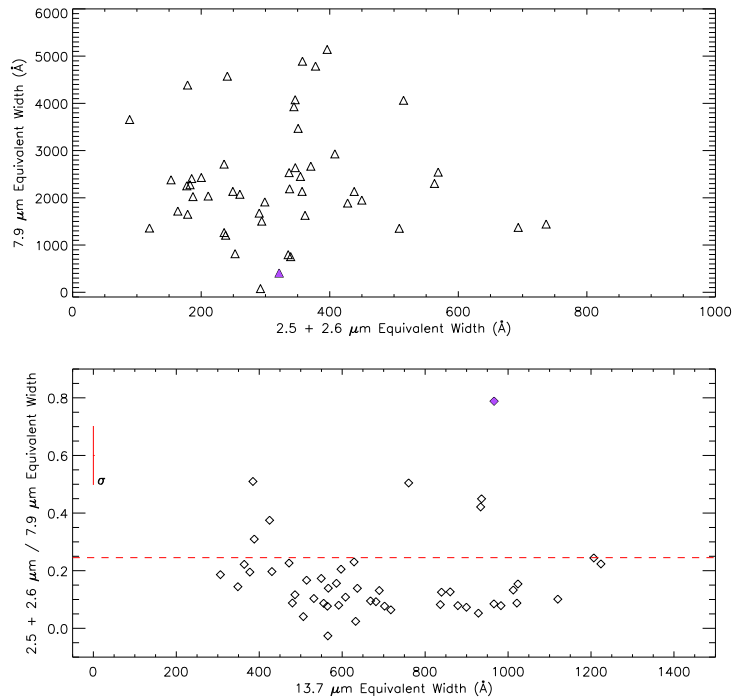


Figure B.8— 2.5 + 2.6 μm Equivalent Width plotted against 7.9 μm Equivalent Width, based on the occurrence of HCN.

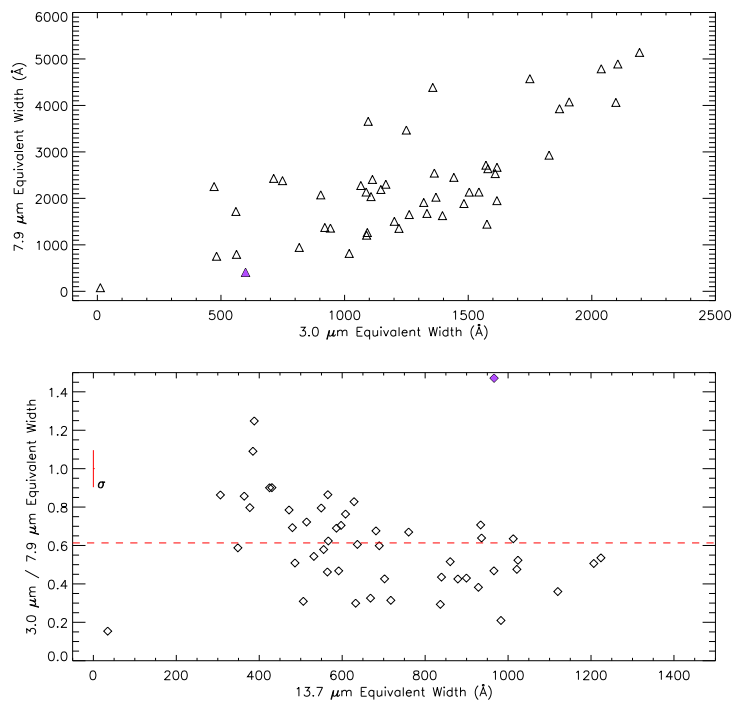


Figure B.9— 3.0 μm Equivalent Width plotted against 7.9 μm Equivalent Width, based on the occurrence of HCN.

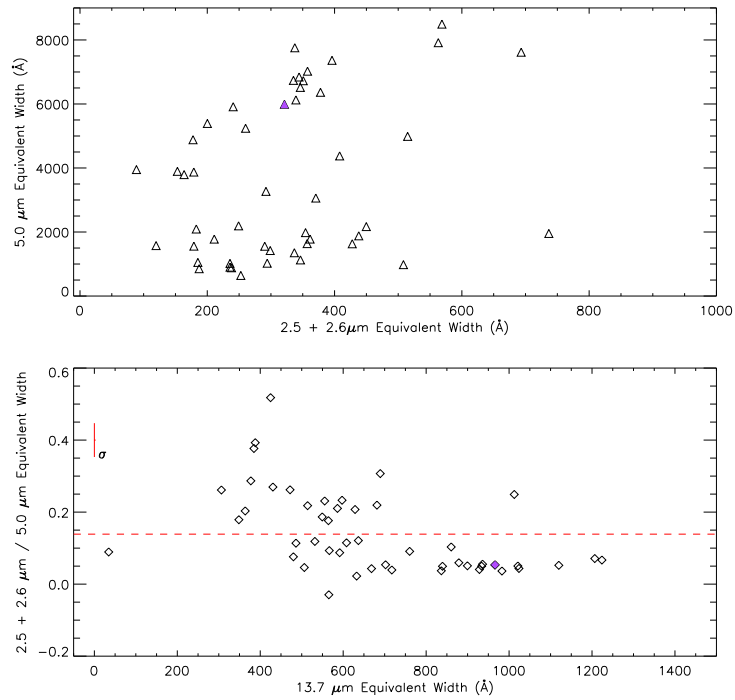


Figure B.10— 2.5 + 2.6 μm Equivalent Width plotted against 5.0 μm Equivalent Width, based on the occurrence of CO.

Appendix C

Classification Color Maps

This appendix presents the color classification maps. In each image each column is a classification criterion and the rows indicate the classification order (hierarchy). A classification is made on sorting the spectra on blackbody temperature and on the EWS for the features given in Table 2.1. Each figure has a different column that has been linear color coded. The columns are in ascending order.

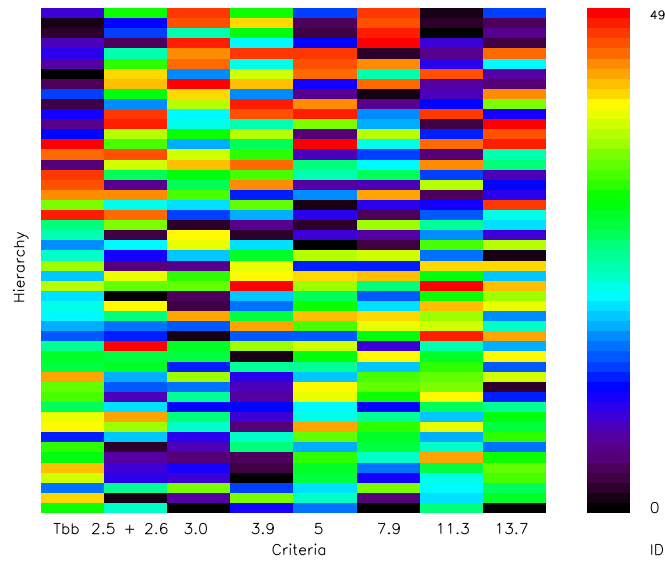


Figure C.1— Classification color map where the spectrum ID has been linear color coded.

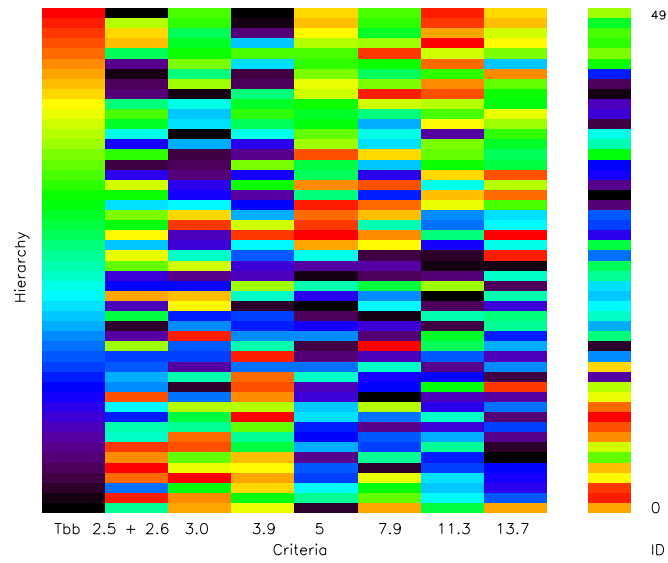


Figure C.2— Classification color map where the sorted 2.5 + 2.6 μm Equivalent Widths have been linear color coded.

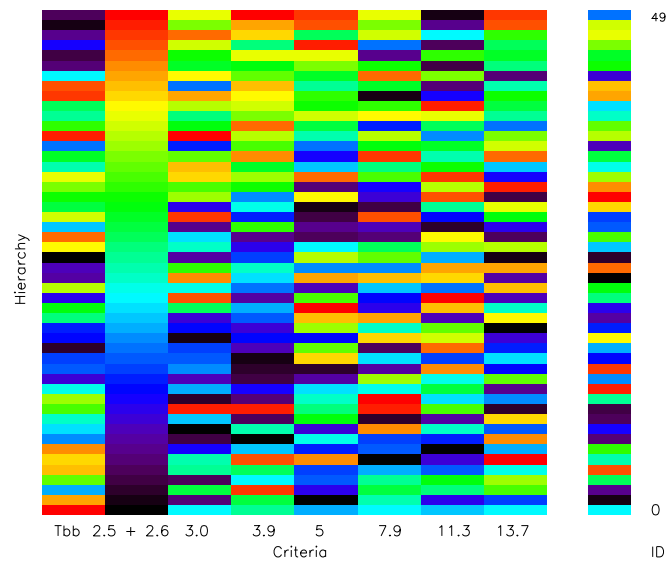


Figure C.3— Classification color map where the sorted auto-fitted blackbody temperatures have been linear color coded.

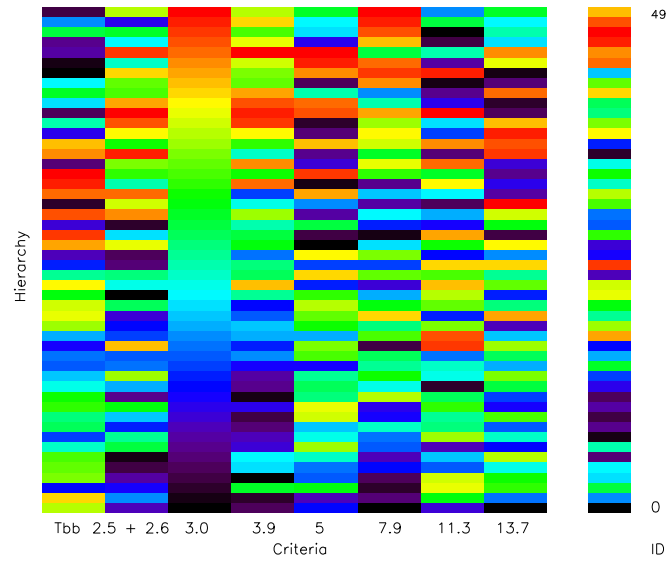


Figure C.4— Classification color map where the sorted 3.0. μm Equivalent Widths have been linear color coded.

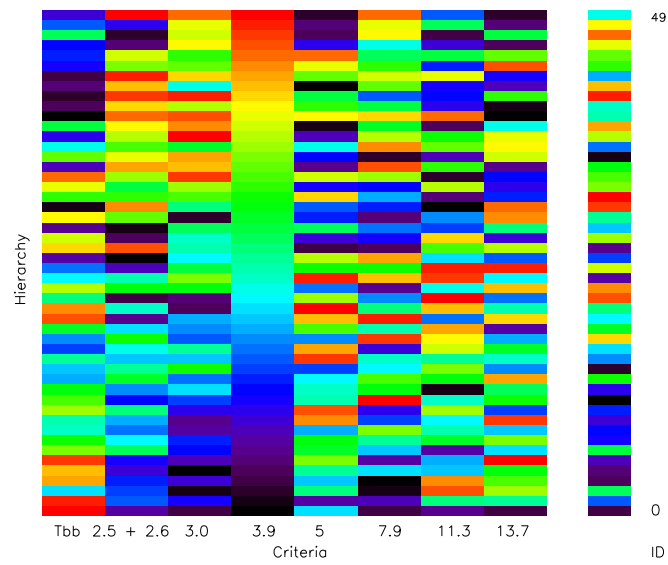


Figure C.5— Classification color map where the sorted 3.9. μm Equivalent Widths have been linear color coded.

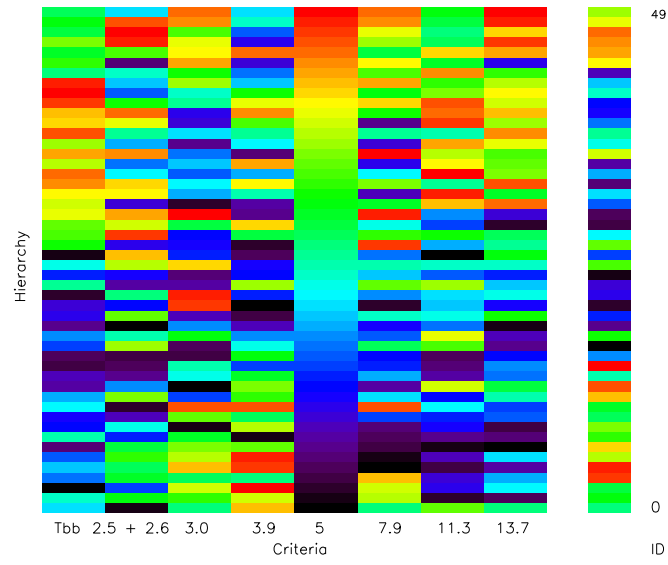


Figure C.6— Classification color map where the sorted 5.0. μm Equivalent Widths have been linear color coded.

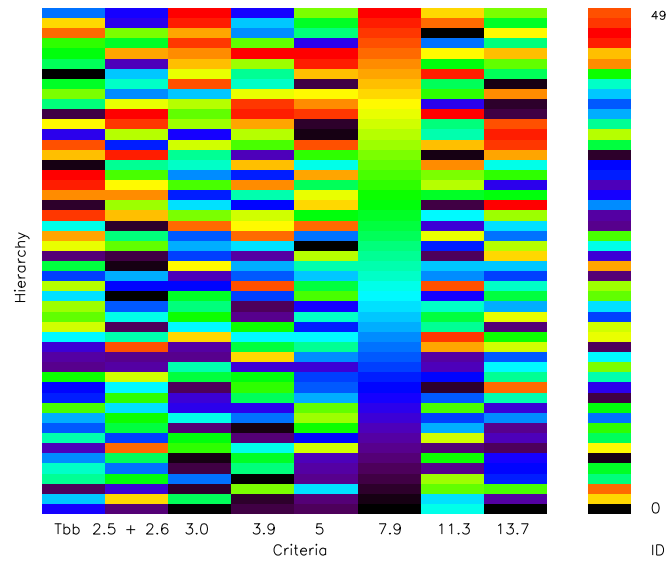


Figure C.7— Classification color map where the sorted 7.9. μm Equivalent Widths have been linear color coded.

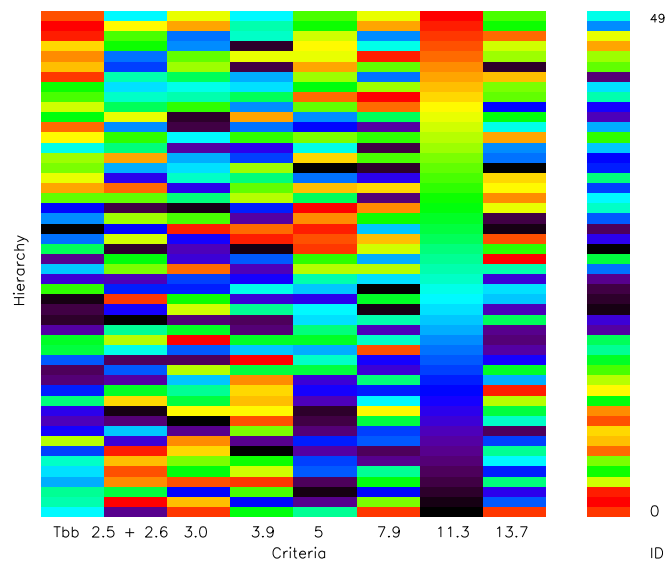


Figure C.8— Classification color map where the sorted 11.3 μm Equivalent Widths have been linear color coded.

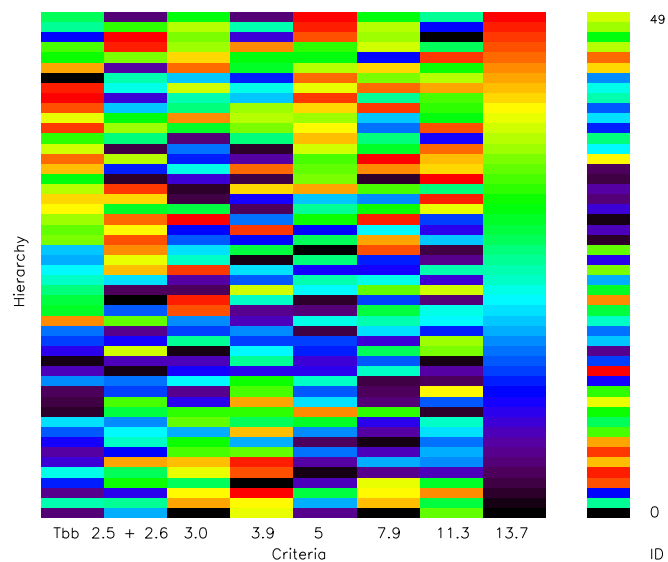


Figure C.9— Classification color map where the sorted 13.7 μm Equivalent Widths have been linear color coded.

Appendix D

Method 1 refined

This appendix presents the result for the scaling parameters when using the *method 2* routine with fixed power-law index γ (*method 1*).

	TU Tau	R^2	W Ori	R^2	S Sct	R^2	VX And	R^2
<i>d</i>	-	-	0.164	0.997	0.534	0.991	0.840	0.973
<i>c</i>	391.6	-	396.4	-	406.6	-	434.6	-
<i>t</i>	-	-	0.816	0.998	0.838	0.986	0.546	0.991

Table D.1— Refined scaling parameters for *method 1* using fit routine from *method 2*.

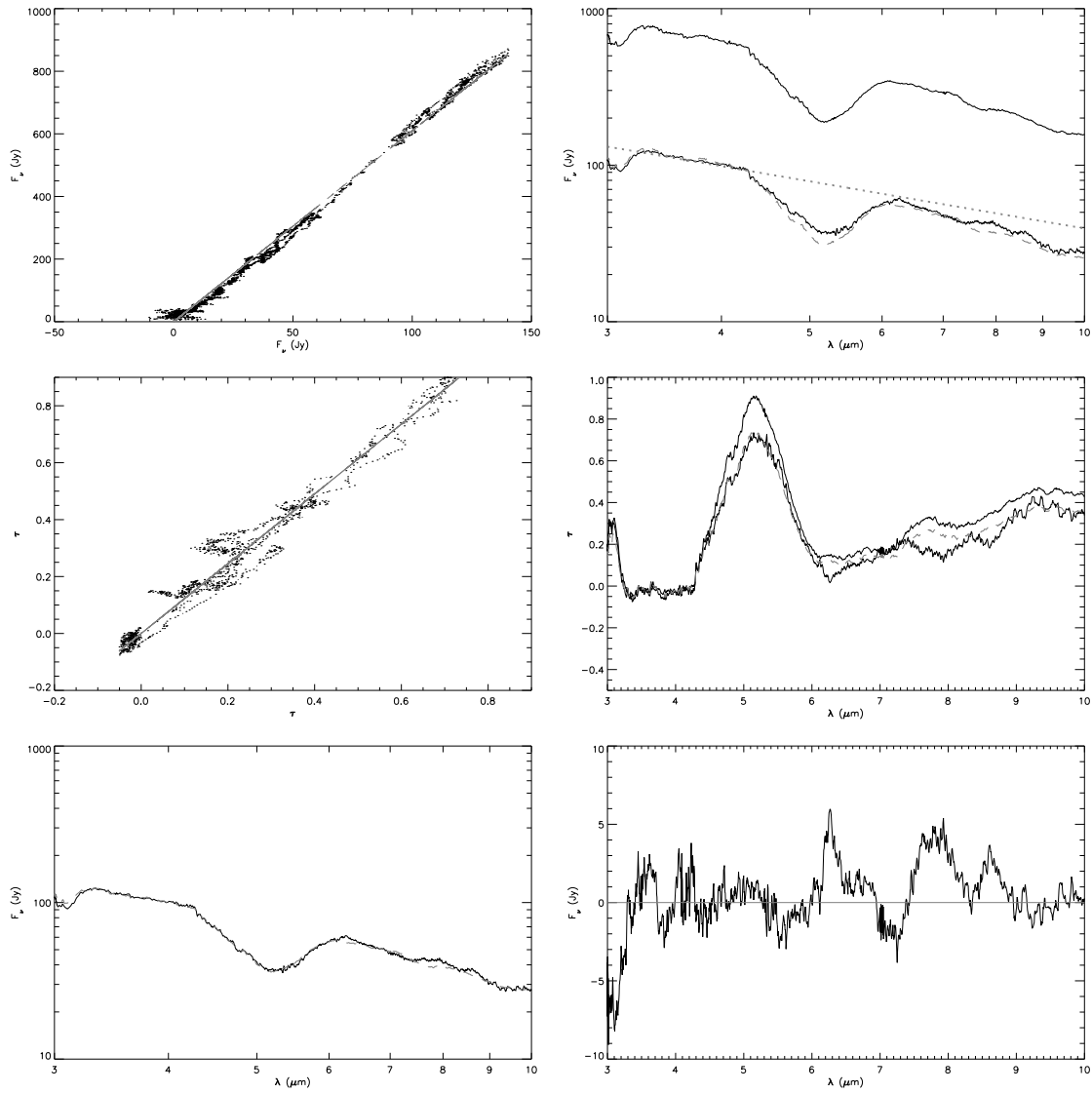


Figure D.1— Resulting residual UIR band emission when using *method 2* with a fixed power-law index of $\gamma = 1$ and W Ori as selected comparison star .

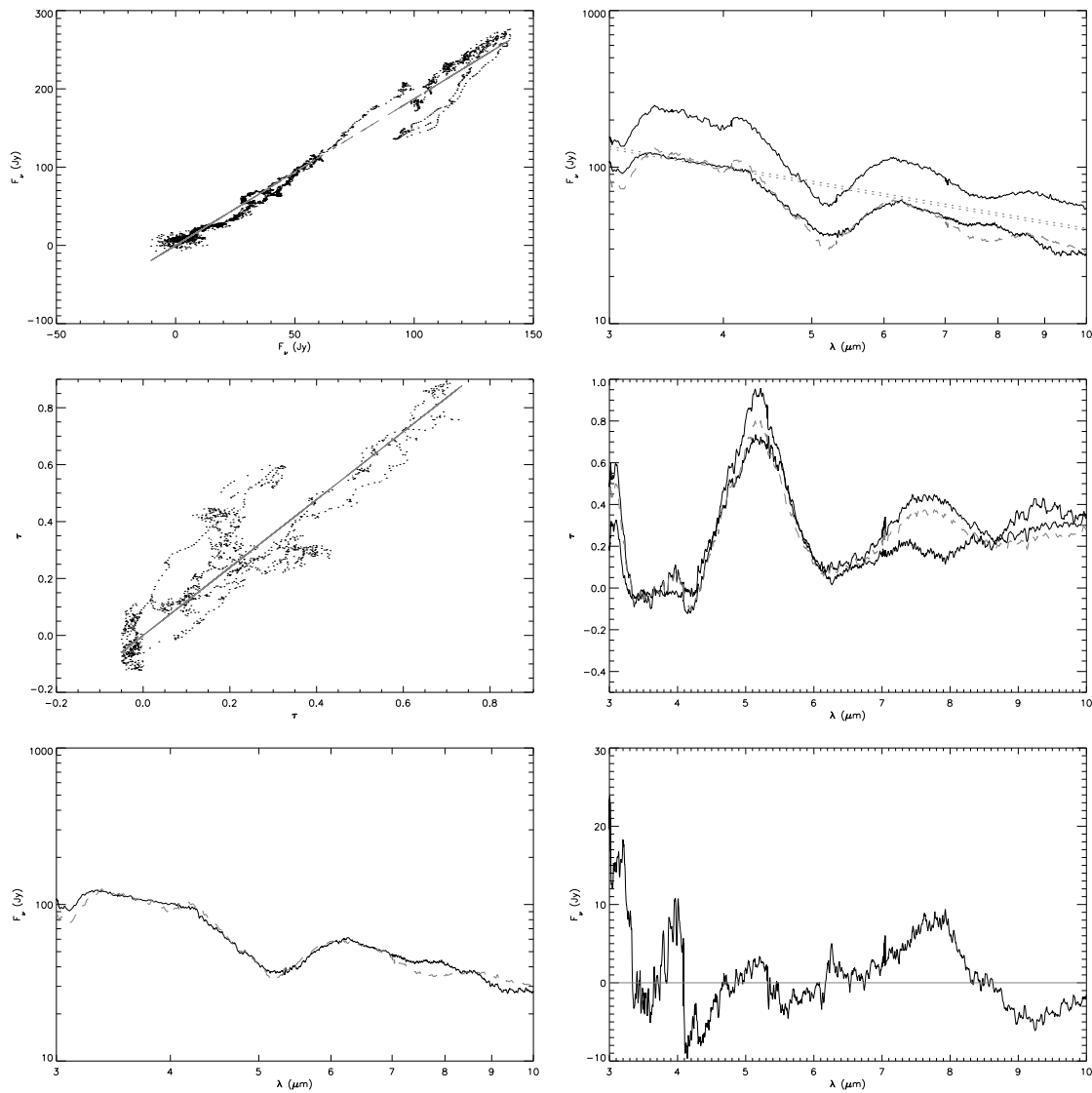


Figure D.2— Resulting residual UIR band emission when using *method 2* with a fixed power-law index of $\gamma = 1$ and S Sct as selected comparison star .

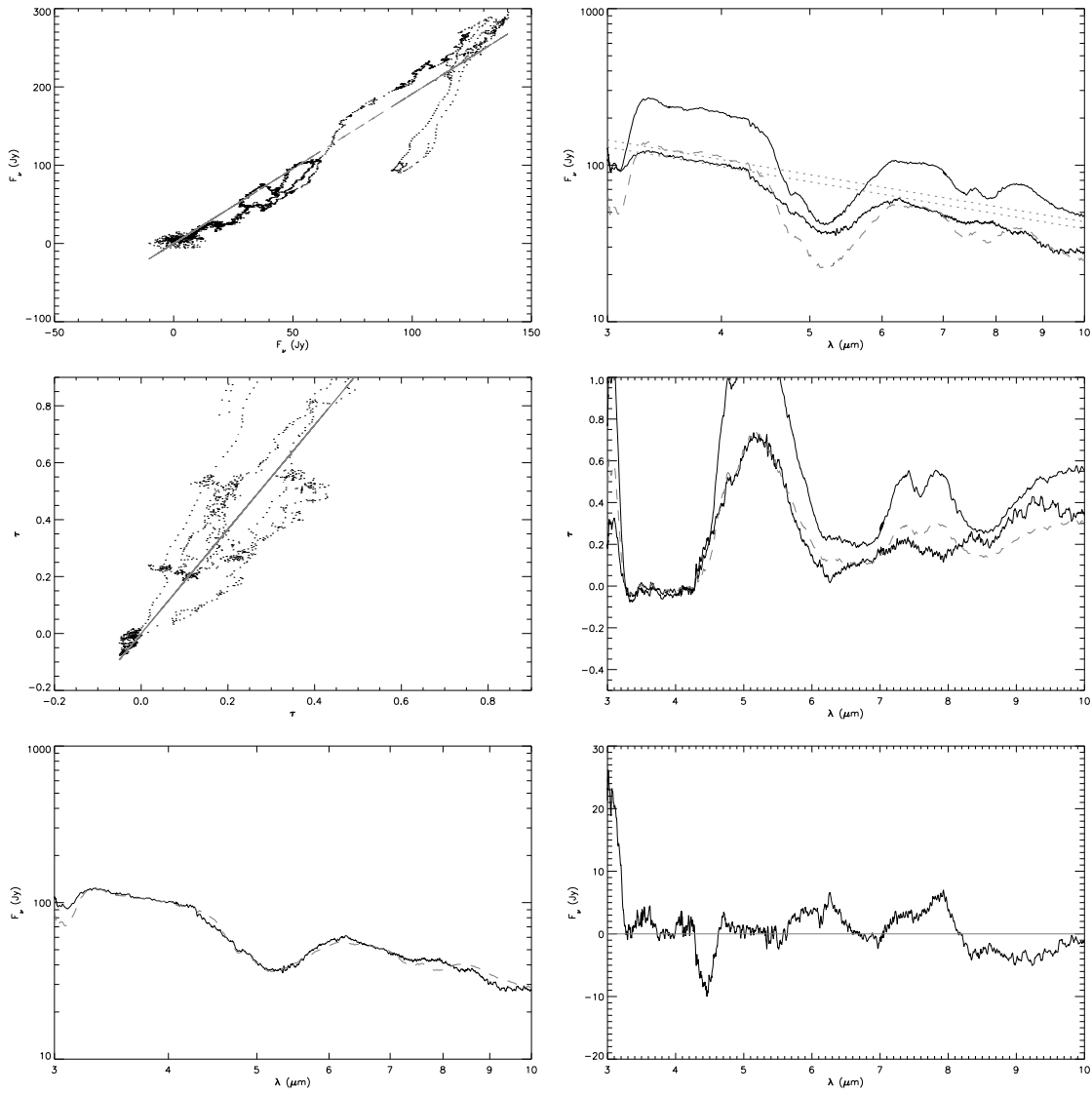


Figure D.3— Resulting residual UIR band emission when using *method 2* with a fixed power-law index of $\gamma = 1$ and VX And as selected comparison star .